

1 **Eupnea, Tachypnea, and Autoresuscitation in a Closed-Loop Respiratory Control**
2 **Model**

3 Casey O. Diekman,¹ Peter J. Thomas,² and Christopher G. Wilson³

4 ¹*Corresponding author*

5 *Department of Mathematical Sciences*

6 *New Jersey Institute of Technology*

7 *323 MLK Jr Blvd*

8 *Newark, NJ 07102*

9 *diekman@njit.edu*

10 *(973) 596-3497*

11 ²*Department of Mathematics, Applied Mathematics, and Statistics;*

12 *Department of Biology; Department of Cognitive Science;*

13 *Department of Electrical Engineering and Computer Science,*

14 *Case Western Reserve University*

15 ³*Lawrence D. Longo Center for Perinatal Biology, Division of Physiology,*

16 *School of Medicine, Loma Linda University*

17 (Dated: June 22, 2017)

18 **Abstract**

19 How sensory information influences the dynamics of rhythm generation varies across sys-
20 tems, and general principles for understanding this aspect of motor control are lacking.
21 Determining the origin of respiratory rhythm generation is challenging because the mecha-
22 nisms in a central circuit considered in isolation may be different than those in the intact
23 organism. We analyze a closed-loop respiratory control model incorporating a central pat-
24 tern generator (CPG), the Butera-Rinzel-Smith (BRS) model, together with lung mechanics,
25 oxygen handling, and chemosensory components. We show that: (1) Embedding the BRS
26 model neuron in a control loop creates a bistable system; (2) Although closed-loop and
27 open-loop (isolated) CPG systems both support eupnea-like bursting activity, they do so
28 *via* distinct mechanisms; (3) Chemosensory feedback in the closed loop improves robustness
29 to variable metabolic demand; (4) The BRS model conductances provide an autoresuscita-
30 tion mechanism for recovery from transient interruption of chemosensory feedback; (5) The
31 *in vitro* brainstem CPG slice responds to hypoxia with transient bursting that is qualita-
32 tively similar to *in silico* autoresuscitation. Bistability of bursting and tonic spiking in the
33 closed-loop system corresponds to coexistence of eupnea-like breathing, with normal minute
34 ventilation and blood oxygen level, and a tachypnea-like state, with pathologically reduced
35 minute ventilation and critically low blood oxygen. Disruption of the normal breathing
36 rhythm, either through imposition of hypoxia or interruption of chemosensory feedback,
37 can push the system from the eupneic state into the tachypneic state. We use geometric
38 singular perturbation theory to analyze the system dynamics at the boundary separating
39 eupnea-like and tachypnea-like outcomes.

40

41 **Keywords:** respiratory rhythm, central pattern generator, closed-loop control model, hy-
42 poxia, autoresuscitation

43

44 **New & Noteworthy**

45 A common challenge facing rhythmic biological processes is the adaptive regulation of central
46 pattern generator (CPG) activity in response to sensory feedback. We apply dynamical
47 systems tools to understand several properties of a closed-loop respiratory control model,
48 including the coexistence of normal and pathological breathing, robustness to changes in
49 metabolic demand, spontaneous autoresuscitation in response to hypoxia, and the distinct

50 mechanisms that underlie rhythmogenesis in the intact control circuit versus the isolated,
51 open-loop CPG.

52 INTRODUCTION

53 Sensory feedback is essential to guide the timing of rhythmic motor processes. How
54 sensory information influences the dynamics of a central pattern generating circuit varies
55 from system to system, and general principles for understanding this aspect of rhythmic
56 motor control are lacking. To complicate matters, the mechanism underlying rhythm gener-
57 ation in a central circuit when considered in isolation may be different from the mechanism
58 underlying rhythmicity in the intact organism.

59 Despite decades of investigation there remains little consensus about the mechanisms
60 underlying sustained oscillations during respiratory rhythmogenesis in the brainstem. On
61 one hand, it has been proposed that oscillations in the preBötzinger complex (pBC) arise
62 mainly from synchronized activity of endogenously bursting cells that interact in a highly
63 coupled network, and drive a population of amplifying follower cells (Smith et al., 2000). On
64 the other hand, it has also been suggested that oscillations arise from network-dependent
65 interactions of conditionally bursting cells (Feldman et al., 2013). More elaborate models
66 have proposed that interactions between multiple brainstem areas are essential for generating
67 and shaping breathing rhythms (Smith et al., 2007; Rybak et al., 2007; Lindsey et al.,
68 2012). Without presuming to adjudicate between these alternatives, here we investigate an
69 alternative hypothesis, namely that *respiratory rhythms arise from the interplay of central*
70 *rhythm generation circuits, biomechanics, and feedback from peripheral signaling pathways.*

71 Our understanding of respiratory rhythmogenesis derives in large part from the pioneer-
72 ing work of Smith, Feldman, Ramirez and others who demonstrated that the pBC can
73 autonomously sustain respiratory-like oscillations in isolated brainstem slice preparations
74 (Smith et al., 1991; Ramirez et al., 1997). However, it has long been observed that the
75 mechanisms underlying oscillations in a central pattern generator (CPG) may differ fun-
76 damentally in the intact organism versus a deafferented, isolated central circuit (Bässler,
77 1986; Koshiya and Smith, 1999). Here we investigate rhythmogenesis in a simple model of
78 closed-loop respiratory control, incorporating biomechanics, oxygen handling, metabolism,
79 and chemosensation. We show that eupnea-like oscillations arise from a distinct mechanism

80 in the intact (closed-loop) *versus* isolated (open-loop) systems. Specifically:

- 81 • During eupneic oscillations in the closed-loop model, the time-varying excitatory drive
82 to the CPG (the control parameter g_{tonic}) remains entirely in a domain that corre-
83 sponds to quiescent behavior in the open-loop model with constant g_{tonic} .
- 84 • The frequency of respiratory oscillations in the isolated central pattern generator sys-
85 tem is controlled by the time constant for a persistent sodium current (τ_h); whereas
86 the frequency of eupneic oscillations in the intact system is relatively insensitive to
87 changes in τ_h .
- 88 • In contrast, the frequency of breathing in the closed-loop model *can* be controlled
89 by manipulating the frequency content of the time-varying excitatory drive feedback
90 signal.

91 The paper is organized as follows: we develop the model and analyze its behavior using
92 averaging and open-loop/closed-loop control analysis; we demonstrate bistable states cor-
93 responding to coexistence of eupnea and tachypnea; and we show that imposed bouts of
94 hypoxia, or sustained interruption of the chemosensory pathway monitoring arterial blood
95 oxygen levels, can precipitate a dramatic transition from eupnea to tachypnea. However, for
96 moderate bouts of hypoxia, or brief interruptions of chemosensory feedback, the endogenous
97 properties of the ionic conductances in a standard CPG model (Butera Jr. et al., 1999a)
98 can lead to spontaneous autoresuscitation.

99 A preliminary version of the model was presented at the 34th Annual International Con-
100 ference of the IEEE EMBS (Diekman et al., 2012).

101 METHODS

102 Model equations

Central Pattern Generator (CPG): We adopt the Butera-Rinzel-Smith (BRS) model (“model 1” in (Butera Jr. et al., 1999a)) of bursting pacemaker neurons in the preBötzinger complex as our central pattern generator. We represent the CPG with a single BRS unit described by the membrane potential V and dynamical gating variables n (delayed rectifying

potassium (I_K) activation) and h (persistent sodium (I_{NaP}) inactivation). Two “instantaneous” gating variables p_∞ (I_{NaP} activation) and m_∞ (fast sodium (I_{Na}) activation) are set equal to their voltage-dependent asymptotic values; the I_{Na} inactivation gate is set equal to $(1 - n)$. In addition, the model includes leak (I_L) and tonic excitatory (I_{tonic}) currents. The governing equations for the CPG are:

$$C \frac{dV}{dt} = -I_K - I_{\text{NaP}} - I_{\text{Na}} - I_L - I_{\text{tonic}} \quad (1)$$

$$\frac{dn}{dt} = \frac{n_\infty(V) - n}{\tau_n(V)} \quad (2)$$

$$\frac{dh}{dt} = \frac{h_\infty(V) - h}{\tau_h(V)} \quad (3)$$

$$I_K = g_K n^4 (V - E_K) \quad (4)$$

$$I_{\text{NaP}} = g_{\text{NaP}} p_\infty(V) h (V - E_{\text{Na}}) \quad (5)$$

$$I_{\text{Na}} = g_{\text{Na}} m_\infty^3(V) (1 - n) (V - E_{\text{Na}}) \quad (6)$$

$$I_L = g_L (V - E_L) \quad (7)$$

$$I_{\text{tonic}} = g_{\text{tonic}} (V - E_{\text{tonic}}) \quad (8)$$

$$x_\infty(V) = \frac{1}{1 + \exp[(V - \theta_x)/\sigma_x]} \quad (9)$$

$$\tau_x = \frac{\bar{\tau}_x}{\cosh[(V - \theta_x)/2\sigma_x]} \quad (10)$$

103 where $C = 21$ pF, $g_K = 11.2$ nS, $g_{\text{NaP}} = 2.8$ nS, $g_{\text{Na}} = 28$ nS, $g_L = 2.8$ nS, $E_K = -85$ mV,
 104 $E_{\text{Na}} = 50$ mV, $E_L = -65$ mV, $E_{\text{tonic}} = 0$ mV, $\theta_n = -29$ mV, $\sigma_n = -4$ mV, $\theta_p = -40$ mV,
 105 $\sigma_p = -6$ mV, $\theta_h = -48$ mV, $\sigma_h = 6$ mV, $\theta_m = -34$ mV, $\sigma_m = -5$ mV, $\bar{\tau}_n = 10$ ms, and
 106 $\bar{\tau}_h = 10,000$ ms.

107

Motor pool activity: The membrane potential (V) of the CPG is an input to the respiratory musculature through synaptic activation of a motor unit (α):

$$\frac{d\alpha}{dt} = r_a[T](1 - \alpha) - r_d\alpha \quad (11)$$

$$[T] = \frac{T_{\text{max}}}{(1 + \exp(-(V - V_T)/K_p))} \quad (12)$$

108 where $r_a = r_d = 0.001$ mM⁻¹ ms⁻¹ sets the rise and decay rate of the synaptic conductance,
 109 and $[T]$ is the neurotransmitter concentration with $T_{\text{max}} = 1$ mM, $V_T = 2$ mV, and $K_p = 5$
 110 mV (Ermentrout and Terman, 2010).

111

Lung volume: The motor unit drives changes in lung volume (vol_L):

$$\frac{d}{dt}(\text{vol}_L) = E_1\alpha - E_2(\text{vol}_L - \text{vol}_0) \quad (13)$$

112 where $\text{vol}_0 = 2 \text{ L}$ is the unloaded lung volume, and $E_1 = 0.4 \text{ L}$ and $E_2 = 0.0025 \text{ ms}^{-1}$ were
 113 chosen to give physiologically reasonable lung expansions (West, 2008). The respiratory
 114 musculature acts as a low-pass filter: low-frequency bursting of the CPG drives discrete
 115 fluctuations in lung volume, but tonic spiking does not. This behavior is analogous to
 116 tetanic muscle contraction in response to high frequency nerve stimulation (Kandel et al.,
 117 1991).

118

Lung oxygen: External air at standard atmospheric pressure (760 mmHg) with 21% oxygen content will have a partial pressure of oxygen $P_{\text{ext}}\text{O}_2 = 149.7 \text{ mmHg}$. When the lungs expand ($\frac{d}{dt}[\text{vol}_L] > 0$), external air is inhaled and we assume this fresh air mixes instantaneously with the air already in the lungs. The partial pressure of oxygen in the lung alveoli ($P_A\text{O}_2$) will increase at a rate determined by the lung volume and the pressure difference between external and internal air. When the lungs are not expanding ($\frac{d}{dt}[\text{vol}_L] \leq 0$), there is no mixing of air. During both lung expansion and contraction, oxygen is being transferred to the blood at a rate determined by the time constant $\tau_{LB} = 500 \text{ ms}$ and the difference between $P_A\text{O}_2$ and the partial pressure of oxygen in the arterial blood ($P_a\text{O}_2$). Thus, the change in $P_a\text{O}_2$ is given by:

$$\frac{d}{dt}(P_a\text{O}_2) = \frac{P_{\text{ext}}\text{O}_2 - P_A\text{O}_2}{\text{vol}_L} \left[\frac{d}{dt}(\text{vol}_L) \right]_+ - \frac{P_A\text{O}_2 - P_a\text{O}_2}{\tau_{LB}} \quad (14)$$

119 where $[x]_+$ denotes $\max(x, 0)$.

120

Blood oxygen: Our model for blood oxygenation is given by:

$$\frac{d}{dt}(P_a\text{O}_2) = \frac{J_{LB} - J_{BT}}{\zeta \left(\beta_{\text{O}_2} + \eta \frac{\partial S_{\text{aO}_2}}{\partial P_a\text{O}_2} \right)}, \quad (15)$$

where the fluxes of oxygen from the lungs to the blood (J_{LB}) and from the blood to the tissues (J_{BT}) have units of moles of O_2 per millisecond, and the denominator converts changes in the number of moles of O_2 in the blood to changes in $P_a\text{O}_2$. J_{LB} depends on the difference in oxygen partial pressure between the lungs and the blood:

$$J_{LB} = \left(\frac{P_A\text{O}_2 - P_a\text{O}_2}{\tau_{LB}} \right) \left(\frac{\text{vol}_L}{RT} \right) \quad (16)$$

121 and is calculated using the ideal gas law $PV = nRT$, where n is the number of moles of O_2 ,
 122 $R = 62.364 \text{ L mmHg K}^{-1} \text{ mol}^{-1}$ is the universal gas constant, and $T = 310 \text{ K}$ is temperature.

J_{BT} accounts for both dissolved and bound oxygen in the blood:

$$J_{BT} = M\zeta(\beta_{O_2} P_aO_2 + \eta \text{SaO}_2). \quad (17)$$

The concentration of dissolved oxygen in the blood is directly proportional to P_aO_2 (known as *Henry's law*), where the constant of proportionality is the blood solubility coefficient $\beta_{O_2} = 0.03 \text{ ml O}_2 \times \text{L blood}^{-1} \text{ mmHg}^{-1}$ for blood at 37 degrees C. At physiological partial pressures (P_aO_2 from approximately 80 to 110 mmHg), the amount of dissolved O_2 is far too small to meet the body's metabolic demand for oxygen. The vast majority of oxygen stored in the blood is bound to hemoglobin (Hb). Hemoglobin has four cooperative oxygen binding sites, leading to the nonlinear (sigmoidal) hemoglobin saturation curve SaO_2 :

$$\text{SaO}_2 = \frac{P_aO_2^c}{P_aO_2^c + K^c} \quad (18)$$

$$\frac{\partial \text{SaO}_2}{\partial P_aO_2} = cP_aO_2^{c-1} \left(\frac{1}{P_aO_2^c + K^c} - \frac{P_aO_2^c}{(P_aO_2^c + K^c)^2} \right), \quad (19)$$

123 where $K = 26 \text{ mmHg}$ and $c = 2.5$ are phenomenological parameters taken from (Keener
 124 and Sneyd, 2009).

The parameter M in (17) represents the rate of metabolic demand for oxygen from the tissues, and unless stated otherwise is set at $8 \times 10^{-6} \text{ ms}^{-1}$. The conversion factors ζ and η in (15) and (17) depend on the concentration of hemoglobin, $[\text{Hb}] = 150 \text{ gm L}^{-1}$, and the volume of blood, $\text{vol}_B = 5 \text{ L}$, respectively. We assume a molar oxygen volume of 22.4 L and that each fully saturated Hb molecule carries 1.36 ml of O_2 per gram:

$$\zeta = \text{vol}_B \times \left(\frac{\text{mole } O_2}{22,400 \text{ mL } O_2} \right) \quad (20)$$

$$\eta = [\text{Hb}] \times \left(\frac{1.36 \text{ mL } O_2}{\text{gm Hb}} \right). \quad (21)$$

Chemosensation: Peripheral chemoreceptors in the carotid bodies detect reductions in P_aO_2 and transmit impulses to the central nervous system through the carotid sinus nerve. In humans, these chemoreceptors are responsible for the increase in ventilation that occurs in response to arterial hypoxemia (Hlastala and Berger, 2001). Carotid body afferent fibers can adjust their firing rate rapidly (even within a respiratory cycle) due to small changes in blood gases (West, 2008). There is a nonlinear relationship between the activity of carotid

chemosensory nerve fibers and P_aO_2 , with very little nerve activity until P_aO_2 is reduced below 100 mmHg and then steep firing rate increases as P_aO_2 is reduced further (Hlastala and Berger, 2001; West, 2008). We modeled this hypoxia chemosensory pathway with a sigmoidal relationship between P_aO_2 and the conductance representing external drive to the CPG (g_{tonic}). Increasing oxygen deficiency increases the respiratory drive:

$$g_{\text{tonic}} = \phi \left(1 - \tanh \left(\frac{P_aO_2 - \theta_g}{\sigma_g} \right) \right) \quad (22)$$

125 where $\phi = 0.3$ nS, $\theta_g = 85$ mmHg, and $\sigma_g = 30$ mmHg. This conductance serves to “close
126 the loop” in our respiratory control model, since $I_{\text{tonic}} = g_{\text{tonic}}(V - E_{\text{tonic}})$ is a term in the
127 CPG voltage equation (1).

128 The closed-loop model (Fig. 1) has the same overall structure as the model in (Diekman
129 et al., 2012). The blood oxygenation component of the model has been substantially revised
130 to better reflect the basic physiology of oxygen transport and ensure conservation of mass.

131 Computational platform

132 Numerical simulations were performed in MATLAB R2016a (MathWorks, Natick, MA)
133 using the *ode15s* solver with absolute tolerance $\leq 10^{-9}$ and relative tolerance $\leq 10^{-6}$.
134 Bifurcation diagrams were constructed using XPPAUT (Ermentrout, 2002). MATLAB code
135 used to generate all figures (except Fig. 12) is available in ModelDB at [http://senselab.
136 med.yale.edu/ModelDB/showModel.cshtml?model=229640](http://senselab.med.yale.edu/ModelDB/showModel.cshtml?model=229640), along with XPP code used to
137 construct the bifurcation diagrams in Figs. 4 and 10.

138 Animal experiments

139 We used *in vitro* experiments to determine if hypoxia exposure of pBC neurons mim-
140 icked some of the features observed in our model. We cut rhythmically active slices from
141 Sprague-Dawley rat pups (postnatal days 0 to 5) anesthetized with 4% isoflurane in a ven-
142 tilated hood. Once the animal reached a surgical plane of anesthesia (no withdrawal to
143 tail or toe pinch) the skull and spinal column was exposed via a midline incision and a
144 scalpel was used to decerebrate the pup and the thorax/spinal column was transected at
145 T1/T2. The spinal column and brainstem were then immersed in ice cold artificial cere-
146 brospinal fluid (ACSF) containing the following (in mM): 124 NaCl, 25 NaHCO₃, 3 KCl,

147 1.5 $\text{CaCl}_2 \cdot 2\text{H}_2\text{O}$, 1.0 $\text{MgSO}_4 \cdot 7\text{H}_2\text{O}$, 0.5 $\text{NaH}_2\text{PO}_4 \cdot \text{H}_2\text{O}$, 30 D-glucose, bubbled with carbo-
148 gen (95/5% O_2/CO_2). We rapidly performed dorsal and ventral laminectomies to expose
149 the neuraxis while preserving the cranial nerve rootlets. Rhythmically active brainstem
150 slices were cut from the brainstem using a vibratome (Leica VT1000). We then transferred
151 the slices to a low volume chamber mounted on an upright microscope with IR-DIC optics
152 and superfused the slice continuously with 95% O_2 and 5% CO_2 for at least 30 min before
153 beginning our experiments. Extracellular potassium concentration was raised to 9 mM to
154 generate a breathing rhythm comparable to an awake human (10 to 20 breaths/bursts per
155 minute). We used whole-cell patch-clamp recordings to assess the behavior of preBötzinger
156 complex neurons and the role that hypoxia/anoxia played in stimulating autoresuscitative
157 transitions in these neurons. The *in vitro* slice preparation and electrophysiological record-
158 ings were performed as described previously (Smith et al., 1991; Koizumi et al., 2008).
159 Briefly, inspiratory cells were acquired by making a tight seal ($\geq 5\text{ G}\Omega$), breaking through
160 to whole cell, and then switching to current clamp for hypoxia/NaCN. To test the role that
161 hypoxia plays in altering rhythmic drive, we switched the gas used to bubble the perfusate
162 to a hypoxic gas mixture (94% N_2 , 1% O_2 , 5% CO_2) or added sodium cyanide (NaCN, 300
163 μM) to the perfusate. Application of either hypoxia or NaCN challenge was for one to three
164 minutes. All animal procedures were approved by the Institutional Animal Care and Use
165 Committee (Case Western Reserve University).

166 RESULTS

167 Distinct mechanisms underlie bursting in isolated CPG and closed-loop 168 systems

169 The closed-loop model described in the Methods section produces a stable eupnea-like
170 breathing rhythm of approximately 10 breaths per minute (Fig. 2A). The central pattern
171 generator components of the model comprise a three-dimensional subsystem (voltage, fast
172 potassium activation gate n , and persistent sodium inactivation gate h) corresponding to
173 the Butera-Rinzel-Smith I_{NaP} pacemaker model. The isolated pacemaker can also produce
174 a eupnea-like fictive breathing rhythm for a range of (fixed) excitatory conductances, with
175 roughly 10 bursts per minute when $g_{\text{tonic}} = 0.3\text{ nS}$ (Fig. 2B). But despite similar timing

176 of bursting in the intact and isolated systems, we find that distinct mechanisms underly
177 rhythmogenesis in these two scenarios. To establish this result, we

- 178 • Compare the range of g_{tonic} supporting bursting in the isolated (open-loop) model,
179 *versus* the values of g_{tonic} attained during eupneic bursting in the intact model. We
180 find that during eupneic bursting for the intact system, the values of g_{tonic} remain
181 within the “quiescent” range for the isolated BRS model.
- 182 • Study the dynamics of bursting superimposed on the bifurcation structure of the
183 (v, n, h) -subsystem. Both the intact and isolated systems exhibit a fixed point near
184 a saddle-node bifurcation, however in the isolated system the fixed point is unstable
185 (allowing spontaneous bursting) and in the intact system it is stable (requiring phasic
186 chemosensory drive to support bursting).
- 187 • Compare the effect of accelerating or retarding the dynamics of the h -gate, in the iso-
188 lated *versus* the intact model. We find that rescaling $\bar{\tau}_h$ causes proportionate changes
189 in burst period in the isolated model, but has little effect in the intact model. More-
190 over, the intact model supports eupneic bursting even when $\bar{\tau}_h$ is infinitely large (h is
191 held fixed as a constant).
- 192 • Study the sensitivity of burst timing to sensory input by rescaling the time course
193 of g_{tonic} . We find that rescaling the time course of g_{tonic} proportionately changes the
194 burst period.

195 *Closed-loop bursting with “quiescent” g_{tonic}*

196 Our model of closed-loop respiratory control includes neural, mechanical, and chemosen-
197 sory components and is capable of producing a stable oscillatory solution that represents
198 normal eupneic breathing. The operation of the closed-loop model is illustrated in Fig. 1.
199 Bursts of action potential firing (V) of preBötzinger complex (pBC) neurons in the brainstem
200 CPG activate a pool of motor neurons (α) that contract the diaphragm, causing the lungs
201 to expand in volume (vol_L) and intake air. Inhaled oxygen increases the partial pressure
202 of oxygen in the lung ($P_A\text{O}_2$) and enters the bloodstream through gas exchange between
203 alveoli and capillaries.

204 Peripheral chemoreceptors in the carotid body detect changes in the partial pressure of
205 oxygen in the blood (P_aO_2) and convey this information to the central nervous system by reg-
206 ulating the amount of excitatory input drive g_{tonic} to the brainstem CPG. This chemosensory
207 feedback closes the respiratory control loop and maintains P_aO_2 levels around 100 mmHg.

208 If the connection between P_aO_2 and the CPG is interrupted, then g_{tonic} takes a fixed
209 value and the isolated CPG corresponds to the canonical Butera, Rinzel, and Smith (BRS)
210 model of pBC neurons in a well-studied regime (Butera Jr. et al., 1999a,b; Best et al.,
211 2005; Dunmyre et al., 2011). We refer to this as the “open-loop” system. For a range
212 of g_{tonic} values, bursting arises through fast activation and slow inactivation of a persistent
213 sodium current I_{NaP} . The timescale of bursting is controlled by the inactivation variable h ,
214 which must de-inactivate sufficiently after a burst before the next burst can begin. With
215 a maximal time constant $\bar{\tau}_h$ of 10 s, both the closed-loop model and the open-loop model
216 (with $g_{\text{tonic}} = 0.3$ nS) exhibit burst periods of approximately 6 s (Fig. 2A and 2B).

217 In the open-loop system, the dynamics of h are essential for bursting: if h were held
218 constant then the model can exhibit quiescence or repetitive spiking, but is not capable
219 of bursting. For example, with h held constant at 0.6, the isolated BRS model exhibits
220 hyperpolarized quiescence for $g_{\text{tonic}} < 0.31$, tonic spiking for $0.31 < g_{\text{tonic}} < 1.64$, bistability
221 of tonic spiking and depolarized quiescence for $1.64 < g_{\text{tonic}} < 2.57$, and depolarized quies-
222 cence for $g_{\text{tonic}} > 2.57$. In contrast, the dynamics of h are not essential for bursting in the
223 closed-loop system, since fluctuation of g_{tonic} in response to changes in P_aO_2 also operates
224 on the time scale of eupneic breathing. A reduced version of the closed-loop model where h
225 is held constant at 0.6 produces bursting with a period of approximately 7 s (Fig. 2C). Thus,
226 closed-loop bursting does not require the dynamical mechanism responsible for bursting in
227 the isolated CPG.

228 Additional evidence that distinct mechanisms underlie bursting in the open and closed-
229 loop models comes from the surprising observation that the closed-loop limit cycle exists
230 entirely within the quiescent regime of the isolated CPG system. To compare the operation
231 of the circuit in these different configurations, we conducted a series of simulations of the
232 open-loop (static g_{tonic} , dynamic h) model over a range of g_{tonic} values (Fig. 3, blue markings),
233 and the reduced closed-loop (dynamic g_{tonic} , static h) model over a range of h values (Fig. 3,
234 red markings). The open-loop model exhibits quiescence if $g_{\text{tonic}} < 0.28$ nS, bursting if
235 $0.28 < g_{\text{tonic}} < 0.44$ nS, and beating if $g_{\text{tonic}} > 0.44$ nS. The reduced closed-loop model

236 exhibits quiescence if $h < 0.3$, slow beating if $0.3 < h < 0.45$, bursting if $0.45 < h < 0.75$,
 237 and fast beating if $h > 0.75$. One might naïvely predict that the limit cycle corresponding
 238 to eupneic bursting in the full closed-loop model (dynamic g_{tonic} , dynamic h) would exist
 239 in the region corresponding to bursting in both the static g_{tonic} and static h models (i.e.
 240 the region labeled Bu/Bu in Fig. 3). Instead, we find that the closed-loop trajectory (black
 241 trace in Fig. 3) exhibits h values in the bursting region of the reduced closed-loop model,
 242 but g_{tonic} values that lie entirely within the quiescent region of the open-loop model (the
 243 Q/Bu region in Fig. 3). Thus, we observe a novel form of excitability in the canonical BRS
 244 model: a time-varying g_{tonic} produces bursting despite the g_{tonic} values remaining within the
 245 quiescent region (i.e., the maximum g_{tonic} value observed during bursting in the closed-loop
 246 model is less than the minimum g_{tonic} needed to obtain bursting in the open-loop model).

247 *Bifurcation analysis*

248 In order to understand the distinct mechanisms of closed-loop bursting in more detail,
 249 Figure 4 walks through the dynamics in a series of projections onto the $V - h$ plane. The
 250 ability of the closed-loop system to exhibit bursting with a time-varying g_{tonic} that is always
 251 less than the value of static g_{tonic} required for bursting can be understood by considering
 252 the bifurcation structure of the BRS equations. Bursting consists of oscillations on two
 253 timescales: a slow alternation between silent and active phases, and rapid spiking oscillations
 254 during the active phase. Models of bursting can be decomposed into a fast subsystem
 255 responsible for generating spikes, and a slow subsystem that modulates spikes and the resting
 256 membrane potential (Ermentrout and Terman, 2010). In the BRS model, h evolves on a
 257 slower timescale than V and n . Thus equations (1)–(2) form the fast subsystem, which we
 258 denote as (\dot{V}, \dot{n}) , and equation (3) is the slow subsystem, which we denote \dot{h} . Different
 259 classes of bursting can be identified based on the types of bifurcations that occur in the fast
 260 subsystem to cause transitions between the silent and active phases when the slow variable
 261 is treated as a bifurcation parameter (Rinzel, 1987; Bertram et al., 1995).

262 The BRS model is an example of “fold/homoclinic” bursting, where spiking initiates at
 263 a fold bifurcation and terminates at a homoclinic bifurcation (Izhikevich, 2007). This type
 264 of bursting has also been called “square-wave” bursting since the shape of the membrane
 265 potential profile resembles a square wave (Fig. 2A). The steady states of the fast subsystem,

266 *i.e.* points satisfying $(\dot{V} = 0, \dot{n} = 0)$, form an S-shaped curve in the $V - h$ plane that we
 267 denote \mathcal{S} . The lower branch of \mathcal{S} is stable, and meets the middle branch of unstable fixed
 268 points at the lower knee ($h = 0.61, V = -51.4$), where a fold bifurcation occurs as shown
 269 in Fig. 4A. Another fold bifurcation, which is not shown in the figure, occurs at the upper
 270 knee ($h = -1.56, V = -29.7$), where the middle and upper branches of \mathcal{S} meet. The upper
 271 branch becomes stable through a subcritical Hopf bifurcation at ($h = 0.92, V = -22.8$).
 272 The branch of unstable periodic orbits that are born at this Hopf bifurcation coalesce with
 273 a branch of stable periodic orbits at the saddle-node of periodic orbits bifurcation located
 274 at $h = 1.17$ (not shown). The stable branch of periodic orbits ends at the homoclinic
 275 bifurcation on the middle branch of \mathcal{S} at $h = 0.57$. During the silent phase of bursting, the
 276 trajectory is along the lower branch of \mathcal{S} at a stable fixed point of the fast subsystem. The
 277 hyperpolarized membrane potential causes the persistent sodium channel to de-inactivate
 278 and h to increase. As h increases, the trajectory moves slowly to the right until the stable
 279 fixed point is destroyed at the fold bifurcation. At this point, the trajectory jumps up to the
 280 stable branch of periodic solutions and spiking begins. The depolarized membrane potential
 281 during spiking causes the persistent sodium channel to inactivate and h to decrease. As h
 282 decreases, the period of the limit cycle—and therefore the time between spikes—increases
 283 until spiking ends when the limit cycle merges with the invariant manifold of a saddle point
 284 at the homoclinic bifurcation. At this point, the trajectory jumps down to the stable branch
 285 of \mathcal{S} , ending the active phase of that burst and beginning the silent phase of the next burst.
 286 Throughout both phases of open-loop bursting, all fixed points of the full system (1)–(3) are
 287 unstable. This is indicated by all intersections of the h -nullcline (defined as $\dot{h} = 0$) occurring
 288 on unstable portions of \mathcal{S} (Fig. 4A bottom panel).

289 In contrast, during closed-loop bursting the h -nullcline always intersects the stable lower
 290 branch of \mathcal{S} (Figs. 4B–D bottom panels). These stable fixed points of the full CPG subsystem
 291 $(\dot{V}, \dot{n}, \dot{h})$ correspond to g_{tonic} taking values that would lead to stable quiescence in the isolated
 292 BRS model. However, in the closed-loop model, when the CPG is quiescent (as in Fig. 4B)
 293 then $P_a\text{O}_2$ starts to fall, which causes g_{tonic} to increase. Slowly increasing g_{tonic} gradually
 294 shifts \mathcal{S} to the left, allowing the trajectory to jump up at the lower knee fold bifurcation
 295 and start spiking, even though the CPG fixed point remains stable (Fig. 4C). The spiking
 296 of the CPG eventually causes $P_a\text{O}_2$ to increase, which in turn causes g_{tonic} to decrease and
 297 shifts \mathcal{S} to the right, leading to the homoclinic bifurcation that terminates spiking (Fig. 4D).

298 Thus, although the same bifurcations occur in the fast subsystem during both open- and
299 closed-loop bursting, the time-varying nature of g_{tonic} in the closed-loop system changes the
300 way in which the bifurcations are approached in comparison to the open-loop system.

301 *Sensitivity of burst timing to sensory input and internal dynamics*

302 We find that the timing of bursts in the closed-loop system is governed by chemosensory
303 feedback, rather than the intrinsic bursting mechanism of the isolated CPG (slow inactiva-
304 tion of I_{NaP} through the h -gate). To assess the influence of h dynamics in controlling burst
305 properties, we simulated the open-loop and closed-loop models with $\bar{\tau}_h$ ranging from 8 to
306 45 s (Fig. 5). The interburst interval (IBI), burst duration, and the number of spikes per
307 burst all varied linearly as a function of $\bar{\tau}_h$ in the open-loop model, whereas in the closed-
308 loop model these burst properties were much less sensitive to changes in $\bar{\tau}_h$. To assess the
309 influence of the timescale for chemosensory input τ_{PaO_2} in controlling burst properties, we
310 recorded the g_{tonic} values observed during closed-loop eupneic bursting with $\bar{\tau}_h = 10$ s, and
311 then played back compressed ($\gamma < 1$) or elongated ($\gamma > 1$) versions of this g_{tonic} waveform
312 as a forcing signal to the BRS model (with $\bar{\tau}_h = 10$ s). For $\gamma = 1$, the forced BRS exhibited
313 identical burst properties to the closed-loop model, as one would expect. For $\gamma = 0.8$, the
314 system entrained 1:1 to the forcing and exhibited smaller IBIs, burst durations, and number
315 of spikes per burst. For $\gamma < 0.8$, the system could not keep up with the forcing and lost
316 1:1 entrainment, instead only bursting once for every two peaks of the g_{tonic} waveform. For
317 $\gamma > 1$, IBI increased linearly with γ , whereas burst duration and number of spikes per burst
318 increased up to $\gamma = 2$ before leveling off or even decreasing. These simulations highlight
319 the differential roles of h dynamics and g_{tonic} fluctuations in the closed-loop system, with
320 g_{tonic} controlling the overall period of bursting (dominated by IBI) and h controlling spiking
321 during the burst. Thus, it is the timescale of chemosensory input that determines burst
322 timing in the closed-loop system, and not the timescale of the internal CPG dynamics.

323 **Bistability of eupnea and tachypnea in the closed-loop model**

324 In the closed-loop model, the stable bursting rhythm that represents eupneic breath-
325 ing coexists with a stable beating rhythm that represents pathologically rapid and shallow

326 “tachypneic” breathing. This bistability is evident in Fig. 6, which shows two simulations
 327 of the closed-loop model with identical parameter values but different initial conditions. In
 328 Fig. 6A, spikes during the active phase of CPG bursting drive lung expansions that bring
 329 in new air, causing an increase in P_aO_2 . During the silent phase of the burst, the lungs
 330 relax as air is exhaled and P_aO_2 decreases. The oscillation in P_aO_2 between 90 and 110
 331 mmHg produces an oscillation in g_{tonic} between 0.12 and 0.22 nS, which in turn leads to
 332 CPG bursting that maintains eupnea. In contrast, Fig. 6B shows that tonic spiking of the
 333 CPG fails to drive lung expansions large enough to support effective gas exchange, resulting
 334 in a P_aO_2 level well below the desired range. The low P_aO_2 produces a high g_{tonic} , which
 335 reinforces tonic spiking, trapping the system in a pathological state.

336 To better understand the nature of the bistability between normal and reduced P_aO_2 levels
 337 observed in the closed-loop model, we analyzed a reduced version of the open-loop model
 338 obtained by approximating the dynamics of the control variable P_aO_2 using the method
 339 of averaging (Sanders et al., 2007). If the dynamics of the control variable P_aO_2 evolve on
 340 a slow time scale, then our analysis is formally equivalent to an averaging analysis of the
 341 closed-loop model decomposed into fast and slow variables. We find that during eupneic
 342 bursting, the intrinsic slowness of the variables (measured as the maximum rate of change
 343 divided by the range of the variable) span multiple temporal scales, with P_aO_2 , vol_L , and
 344 P_AO_2 being an order of magnitude slower than h and α , which in turn are an order of
 345 magnitude slower than v and n (Appendix Table I). Since P_aO_2 is both a slow variable and
 346 the control variable, we reduce the closed-loop system to this single component and obtain
 347 a reduced model of the form:

$$\frac{dy}{dt} \approx \bar{g}(y), \quad (23)$$

348 where $y = P_aO_2$, and \bar{g} is defined by averaging the expression for the P_aO_2 flux, given a
 349 fixed P_aO_2 value (see (27)-(28) in the Appendix). This one-dimensional model facilitates
 350 understanding the dynamics of the control variable. In particular, P_aO_2 decreases when
 351 $\bar{g} < 0$, increases when $\bar{g} > 0$, and remains constant when $\bar{g} = 0$. P_aO_2 values for which
 352 $\bar{g} = 0$ are fixed points of our reduced (one-dimensional) slow subsystem. In Figure 7A we
 353 show \bar{g} for three different values of the metabolic demand M . With $M = 0.4 \times 10^{-5} \text{ ms}^{-1}$
 354 (green curve), the system has a stable fixed point at $P_aO_2 = 90$ corresponding to eupnea, a
 355 stable fixed point at $P_aO_2 = 40$ mmHg corresponding to tachypnea, and an unstable fixed
 356 point at $P_aO_2 = 80$ mmHg that acts as a boundary between the two stable states. With

357 $M = 0.8 \times 10^{-5} \text{ ms}^{-1}$ (cyan curve), the same three fixed points exist but the unstable fixed
 358 point and the stable eupneic fixed point are now closer to each other. With $M = 1.6 \times 10^{-5}$
 359 ms^{-1} (magenta curve), only one fixed point exists and it is the stable tachypneic fixed point.
 360 Figure 7B shows the location of the fixed points as a function of M . As M is increased,
 361 the unstable fixed point and the stable eupneic fixed point moved towards one another
 362 until they collide and annihilate each other in a saddle-node bifurcation. Thus, the reduced
 363 model obtained through averaging predicts that, as M is increased, the closed-loop system
 364 will eventually lose bistability and display tachypneic tonic spiking for all initial conditions.
 365 Indeed, simulations of the full model confirm that for high values of M , the closed-loop
 366 system no longer exhibits eupneic bursting (Fig. 8).

367 **Enhanced Robustness of Closed-loop System**

368 The incorporation of chemosensory feedback leads to the closed-loop system being more
 369 robust to changes in metabolic demand than the open-loop system. Figure 8 illustrates the
 370 enhanced robustness of the full closed-loop system in two ways. First, the $P_a\text{O}_2$ versus M
 371 curve has a shallower slope near the desired operating point of $P_a\text{O}_2 = 100 \text{ mmHg}$, where
 372 $\left| \frac{\partial P_a\text{O}_2}{\partial M} \right|$ is 70% less in the closed loop than in the open loop. Thus, the closed-loop model
 373 is locally robust to increases in metabolic demand (*cf.* Robustness and flexibility section
 374 in Discussion). Second, the range of M values for which $P_a\text{O}_2$ stays within the acceptable
 375 range of 80 to 110 mmHg (indicated by the green, shaded band) is larger in the closed loop
 376 ($1 \times 10^{-7} < M < 1.23 \times 10^{-5} \text{ ms}^{-1}$) than it is in the open loop ($0.49 \times 10^{-5} < M < 0.91 \times 10^{-5}$
 377 ms^{-1}). This is a more global, or functional, measure of the robustness.

378 As M is increased from 0.2×10^{-5} to $1.5 \times 10^{-5} \text{ ms}^{-1}$, the mean $P_a\text{O}_2$ levels decrease
 379 from 102 to 90 mmHg in the closed-loop model (black curve) and from 135 to 62 mmHg
 380 in the open-loop model (blue curve). The ability of the closed-loop system to maintain
 381 $P_a\text{O}_2$ levels within a narrower range reflects increased robustness of the closed-loop system
 382 to variations in metabolic demand. However if the metabolic demand becomes too great
 383 ($M > 1.2 \times 10^{-5} \text{ ms}^{-1}$), mean $P_a\text{O}_2$ levels in the closed-loop model drop precipitously as
 384 the system transitions from eupnea to tachypnea. Our averaging analysis predicts that this
 385 transition would occur at $M = 0.82 \times 10^{-5} \text{ ms}^{-1}$, since that is the value of M at which saddle-
 386 node bifurcation occurs in the reduced system (*cf.* Fig. 7B). The fact that this transition

387 occurs at a higher value of M than predicted by analysis of the reduced system illustrates
388 another type of robustness present in the closed-loop system.

389 **Autoresuscitation following transient perturbations**

390 The closed-loop system exhibits surprising resilience to transient perturbations. Due to
391 the bistable nature of the closed-loop system, perturbations can take the system out of the
392 basin of attraction for eupnea and into the basin of attraction for tachypnea. We find that
393 the closed-loop system is able to recover to eupnea following perturbations, even when the
394 perturbation creates transient P_aO_2 levels below 75 mmHg. This “autoresuscitation” phe-
395 nomenon arises from properties intrinsic to the BRS conductances (Diekman et al., 2012).
396 We demonstrate and analyze autoresuscitation using two different types of perturbations.
397 First, we consider perturbations where P_aO_2 instantaneously drops to an abnormally low
398 level. This type of perturbation, which we refer to as an imposed hypoxic event, is rather
399 non-physiological but is mathematically convenient. The second type of perturbation we
400 consider is more physiologically plausible, and models intermittent disruption of chemosen-
401 sory feedback. In this scenario, we temporarily disconnect g_{tonic} from P_aO_2 and hold g_{tonic}
402 at a constant value. All the system variables continue to evolve under this value of g_{tonic} for
403 τ seconds, until we reconnect the loop and again make g_{tonic} a function of P_aO_2 .

404 ***Perturbation I: Imposed hypoxic event***

405 We defined eupneic and tachypneic “ranges” based on the long-term behavior that results
406 from different initial conditions. First, we simulated the open-loop model over a range of
407 g_{tonic} values corresponding to different P_aO_2 levels. The g_{tonic} values were chosen using the
408 chemosensation sigmoid (22) for a range of P_aO_2 values with 0.1 mmHg spacing. Each sim-
409 ulation was allowed to reach steady-state before “closing the loop” and observing whether
410 those initial conditions led to eupnea or tachypnea in the closed-loop system. Closed-loop
411 simulations with initial conditions corresponding to P_aO_2 below 75.6 mmHg resulted in
412 tachypnea, and those with initial conditions corresponding to P_aO_2 above 78.1 mmHg re-
413 sulted in eupnea (Fig. 9). These ranges of P_aO_2 values are henceforth referred to as the
414 tachypneic range and the eupneic range, respectively. The dividing line between these two

415 ranges was approximately $g_{\text{tonic}} = 0.38$, which corresponds to $P_{\text{a}}\text{O}_2 = 76.85$ mmHg (Fig. 9).
 416 However, the restored closed-loop system could recover from transient perturbations that
 417 brought $P_{\text{a}}\text{O}_2$ below this dividing line. For example, at $t = 180$ s we set $P_{\text{a}}\text{O}_2 = 40$ mmHg
 418 and then immediately released the system back to its normal dynamics. We see that the
 419 trajectory escapes the tachypneic range and returns to eupnea. Then, at $t = 360$ s, we set
 420 $P_{\text{a}}\text{O}_2 = 30$ mmHg and again immediately released the system back to its normal dynamics.
 421 The trajectory is not able to escape the tachypneic range after this more severe perturbation.
 422 The system does not recover to eupnea and instead descends into tachypnea.

423 When the system is able to recover from transient hypoxic perturbations, it is due to
 424 the barrage of spiking activity brought on by the reduction in $P_{\text{a}}\text{O}_2$ levels and ensuing
 425 sudden increase in g_{tonic} . The relationship between $P_{\text{a}}\text{O}_2$, g_{tonic} , V , and vol_{L} is illustrated in
 426 Fig. 10A. The active phase of a eupneic burst is 0.39 seconds in duration and consists of 21
 427 spikes, corresponding to a spiking frequency of 54.5 Hz during the active phase (Fig. 10B,
 428 top). In contrast, the burst immediately following the hypoxic perturbation is 0.96 seconds in
 429 duration and consists of 69 spikes, corresponding to a spiking frequency of 72.2 Hz (Fig. 10B,
 430 bottom). The enhanced spiking during this burst leads to a vigorous expansion of lung
 431 volume (Fig. 10A, bottom) that brings extra oxygen into the lungs, ultimately raising $P_{\text{a}}\text{O}_2$
 432 (Fig. 10A, top) to a level high enough that g_{tonic} decreases (Fig. 10A, second from top)
 433 before the system becomes trapped in the tachypneic state. The barrage of spiking that
 434 facilitates autoresuscitation following hypoxic perturbation can be understood in terms of
 435 the bifurcation structure of the fast subsystem of the BRS model (Fig. 10C). As shown
 436 in Fig. 4, the curve of fast subsystem fixed points moves as g_{tonic} fluctuates in the closed-
 437 loop model. During the silent phase of a burst, $P_{\text{a}}\text{O}_2$ decreases and g_{tonic} increases, which
 438 shifts the curve leftward until the trajectory jumps up and begins to exhibit limit cycle
 439 oscillations corresponding to repetitive spiking. During the active phase, h decreases until
 440 the periodic orbits collide with the middle branch of unstable fixed points and are destroyed
 441 in a homoclinic bifurcation. Importantly, the period of the orbits increases logarithmically
 442 as they approach the homoclinic (Gaspard, 1990), thus spiking occurs at a higher frequency
 443 when the trajectory is further from the bifurcation point. Figure 10C (top) shows the
 444 trajectory of a typical eupneic burst, and the location of the curve of steady states, at the
 445 time the trajectory jumps up (green dot). Figure 10C (bottom) shows the trajectory of the
 446 spiking barrage following hypoxic perturbation. Note that when the trajectory jumps up,

447 the curve of fixed points is located much further to the left in the (V, h) plane due to the
448 drastic reduction in P_aO_2 . Since the trajectory is further from the homoclinic bifurcation
449 when it begins spiking, the system exhibits spikes for a longer time and at a higher frequency
450 than it does during the active phase of a typical burst.

451 *Response to transient hypoxia in vitro*

452 Although a sudden drop in P_aO_2 may seem non-physiological, it can be simulated *in vitro*
453 by adding sodium cyanide (NaCN), a pharmacological analog of hypoxia, to the brainstem
454 slice perfusate. Alternatively, hypoxia can be imposed by reducing the amount of O_2 in the
455 gas used to bubble the perfusate. We find that both of these *in vitro* hypoxic challenges
456 induce a similar barrage of spiking in brainstem slices containing the pBC as occurs in the
457 closed-loop model in response to a hypoxic P_aO_2 clamp perturbation. Figure 11A shows a
458 barrage of spikes in an individual pBC cell (top) and increased hypoglossal nerve rootlet
459 discharge (bottom) after bath application of 300 μ M NaCN. Figure 11B shows summary
460 data from nine experiments with increased burst duration and frequency during NaCN or
461 hypoxia treatment, followed by a return to baseline bursting activity after the treatment.
462 The changes in burst duration and frequency are significant ($p < 0.05$) across baseline,
463 NaCN or Hypoxia, and Recovery. There is a delay between the initiation of the treatment
464 and the effect seen in the individual neurons or the network output (XII) due to the “dead
465 space” volume of the perfusion system.

466 The carotid chemoreceptors and their inputs to the nucleus tractus solitarius (NTS) and
467 the rest of the inspiratory rhythm generating circuit are absent in the reduced *in vitro*
468 slice preparation. The cellular mechanisms by which neurons and glia participating in the
469 respiratory neural network sense local changes in oxygen is unknown, however, D’Agostino et
470 al. (2009) have shown that hemeoxygenase is expressed in neurons in the rostral ventrolateral
471 medulla (RVLM) which includes the preBötzing Complex and other respiratory-related
472 neurons and this may serve as a marker for hypoxia-sensitive cells within the pBC. Other
473 cellular mechanisms that may serve as hypoxia sensors in pBC include second messengers as
474 modifiers of K_{ATP} channels (Mironov et al., 1998; Mironov and Richter, 2000), changes in
475 mitochondrial NADH (Mironov and Richter, 2001), and L-type calcium channels (Mironov
476 and Richter, 1998). Even changes in the excitability of upstream projecting neurons, for

477 example from the NTS to the pBC (Takakura et al., 2007), could impact the behavior of
478 our model with changes in oxygen tension.

479 ***Perturbation II: Interruption of chemosensory feedback***

480 To explore the autoresuscitation phenomenon further, we modeled intermittent failure of
481 the chemosensory pathway that transmits information about blood oxygen content to the
482 CPG (Fig. 12). Specifically, we simulated the closed-loop system in the eupneic state and
483 then transiently disconnected g_{tonic} from $P_{\text{a}}\text{O}_2$ by setting g_{tonic} to a constant value of 0.1 nS
484 for durations ranging from 1 to 60 s. This intervention puts the CPG in the quiescent regime
485 and $P_{\text{a}}\text{O}_2$ gradually declines, reaching values below 50 mmHg for durations greater than 35
486 s. We then reconnected the chemosensory feedback, which caused an abrupt increase in
487 g_{tonic} and a barrage of spiking that quickly raised $P_{\text{a}}\text{O}_2$. We observed that if the duration
488 of the chemosensory failure was short enough, the system would recover to eupnea (Fig.
489 12A,C), but if the duration of the failure was sufficiently long, the system would descend
490 into tachypnea (Fig. 12B,D). For chemosensory failure durations near the critical value
491 separating these two states, trajectories transiently exhibited an activity pattern consisting
492 of bursts with a smaller number of spikes and shorter interburst intervals before transitioning
493 to a steady-state of eupneic bursting (as in Fig. 6A) or tachypneic tonic spiking (as in
494 Fig. 6B). In the next section, we show that this intermediate bursting pattern corresponds
495 to an unstable limit cycle with a stable manifold acting as a boundary between respiratory
496 system recovery and failure.

497 **Boundary between eupnea and tachypnea**

498 When pushed to the boundary separating eupnea and tachypnea, the failure or survival
499 of the system depends on the interplay of biomechanics (*e.g.* lung expansion and contrac-
500 tion) and excitability in central circuits (including *h*-gate dynamics) and cannot properly be
501 understood in terms of the central dynamics in isolation. The model has seven dynamical
502 variables, therefore trajectories move in a 7-D space. The two attractors (tachypneic spiking
503 and eupneic bursting) are separated by a smooth 6-D separatrix which is the stable manifold
504 of a metastable set living on the boundary. Simulations suggest that this set is a saddle

505 limit cycle, with a 6-D stable manifold and a 2-D unstable manifold. The intersection of
 506 these two sets of points is a 1-D unstable limit cycle. We computed Floquet multipliers, μ ,
 507 for this limit cycle and found one unstable direction ($\mu > 1$), five stable directions ($\mu < 1$),
 508 and one neutral direction ($\mu = 1$) (see Appendix for details). The components of the eigen-
 509 vector associated with the unstable direction provide information about the impact of each
 510 system variable on the fate of trajectories on the boundary. We analyzed the eigenvectors
 511 at the four locations on the boundary limit cycle indicated by the black arrows in Fig. 13A:
 512 approximately halfway through the quiescent phase of the burst (arrow b), shortly before
 513 the first spike of the active phase (arrow c), in between spikes during the active phase (arrow
 514 d), and shortly after the last spike of the active phase (arrow e). The size of the eigenvector
 515 components indicate how susceptible the system is to being pushed off of the boundary limit
 516 cycle by perturbations in each of the system’s variables. We find that the system is most
 517 sensitive to perturbations in h , P_AO_2 , and P_aO_2 at all four locations (Fig. 13D–E). Since
 518 eigenvectors are only defined up to an arbitrary change in sign, we chose the convention
 519 that the P_aO_2 component is positive in order to orient the eigenvectors consistently around
 520 the limit cycle (we ensured this by multiplying the vectors by -1 when necessary). The sign
 521 of each eigenvector component then indicates whether small increases in that variable push
 522 the system towards eupnea or tachypnea, with positive components being “pro-eupneic” and
 523 negative components being “pro-tachypneic”. We find that the h and P_AO_2 components are
 524 pro-eupneic at all four locations on the limit cycle, whereas α has a small pro-tachypneic
 525 effect at all four locations. The effect of perturbations in lung volume (vol_L) is small and
 526 varies with location. The system is not sensitive to perturbations in V and n , except during
 527 the active phase when V is slightly pro-eupneic (Fig. 13D).

528 **Extent of Autoresuscitation**

529 To quantify the extent of the autoresuscitation regime, we simulated a range of durations
 530 for the interruption of chemosensory feedback. Figure 14 shows P_aO_2 levels 3 minutes after
 531 reestablishing chemosensory feedback, with dark and bright colors indicating low and high
 532 P_aO_2 respectively. In the absence of chemosensory feedback, we assume that the drive to
 533 the CPG no longer fluctuates and set g_{tonic} to constant values between 0 and 0.6 nS when
 534 disconnected from P_aO_2 . If this value was sufficiently close to 0.3 (the nominal g_{tonic} value

535 used for open-loop simulations as shown in Fig. 2A), the CPG exhibited a bursting pattern
536 that kept P_aO_2 levels sufficiently high, such that the system always maintained eupnea when
537 the chemosensory feedback was reconnected. Values of g_{tonic} below this range correspond to
538 cases qualitatively similar to the simulations shown in Fig. 12. Values of g_{tonic} above this
539 range correspond to g_{tonic} being set to a high value in the absence of chemosensory feedback.
540 Here the CPG responds with a barrage of spiking at the beginning, rather than after, the
541 perturbation. This initial barrage raises P_aO_2 and can help the system avoid tachypnea if
542 the perturbation is short enough in duration (Fig. 15). The boundary separating eupnea
543 and tachypnea in this case is again associated with the unstable limit cycle analyzed in Fig.
544 13.

545 DISCUSSION

546 Modeling rationale

547 To understand the generation and stabilization of vital rhythms, such as breathing, one
548 must consider both central and peripheral systems working in concert. Thus one confronts
549 oscillating, nonlinear, closed-loop control systems, which are notoriously difficult to analyze
550 in a general setting (Shimkin, 2009). We chose, therefore, to work with a model that
551 does not include all known aspects of respiratory control, but represents enough salient
552 aspects of the physiology to capture the principal conundrum of interest—the interaction of
553 a stable central pattern generator circuit with phasic sensory feedback provided by peripheral
554 chemosensation.

555 Because breathing is such a fundamental physiological function, one expects there to be
556 multiple interwoven and layered control mechanisms interacting to stabilize and modulate
557 breathing rhythms. For instance, chemosensation allows changes in both oxygen and carbon
558 dioxide concentrations in the bloodstream to dramatically affect the breathing rhythm. Both
559 hypercapnia and hypoxia sensitivity are important, and dysregulation of either—for instance
560 in the perinatal period, when the immature network is still developing—can contribute to
561 pathological apneas (Martin et al., 2012). In order to formulate our model, we select one
562 element from each step in a closed-loop control circuit: sensitivity to blood gasses (hypoxia,
563 in our case), central pattern generation, motor output driving gas exchange, metabolic

564 demand, and, as the final “control variable”, the arterial partial pressure of dissolved oxygen.
565 Despite its relative poverty when compared with the full complexity of respiratory control,
566 our simple model nevertheless exhibits these fundamental features of interest:

- 567 • bistability between a normal “eupneic” state and a pathological “tachypneic” state
- 568 • interaction of intrinsic rhythmicity of central circuitry (BRS model) and global rhythmicity of the closed-loop system
- 569 • spontaneous activity providing a mechanism of “autoresuscitation” following bouts of
- 570 imposed hypoxia or interruption of chemosensory feedback.
- 571

572 We do not claim to have developed a *minimal* model for robust breathing, in the sense that
573 we do not rule out the possibility of a lower-dimensional closed-loop control model exhibiting
574 the same fundamental behaviors. Rather, we think of our model as *minimalist*, in the sense
575 that it incorporates enough physiological realism to shed light on natural respiratory con-
576 trol, yet remains simple enough to be amenable to mathematical analysis. Thorough analysis
577 of any such system requires a constellation of approaches, including control-theoretic tech-
578 niques, dissection of fast and slow timescales, bifurcation analysis, and numerical simulation.
579 We apply these tools to better understand the mechanisms of generation and stabilization
580 of robust breathing rhythms.

581 *Alternative bistable states and interpretations*

582 We interpret the non-bursting, regular spiking or “beating” regime of the CPG in the
583 closed-loop model as tachypnea because it produces rapid and shallow fluctuations in lung
584 volume that are not sufficient to maintain normoxia (Diekman et al., 2012). These lung
585 fluctuations have extremely small amplitude, and in other closed-loop models the beating
586 regime has been interpreted as apneusis, or “holding the breath” after inspiration (Ben-Tal
587 and Smith, 2008). Altering the shape of the g_{tonic} chemosensation sigmoid, by setting the
588 parameters $\phi = 0.2$ nS and $\theta_g = 100$ mmHg in (22), results in a closed-loop model that has
589 bistability between two different bursting regimes of the CPG: one with 20 spikes per burst
590 and a period of 5.8 seconds, and the other with only 3 spikes per burst and a period of 1.4
591 seconds. These bursting patterns produce lung volume fluctuations of 0.9 and 0.07 liters

592 respectively, with the former maintaining P_aO_2 around 100 mmHg and the latter around 30
 593 mmHg. Thus, this version of the closed-loop model again exhibits bistability of eupnea and
 594 tachypnea, where here the tachypnea regime consists of multi-spike bursts occurring at a
 595 higher frequency than eupnea. Although this is perhaps a more natural concept of tachypnea
 596 than the beating regime, we chose to use the beating regime as our model of tachypnea (i.e.
 597 we set $\phi = 0.3$ nS) for this study in order to make the difference between the coexisting
 598 physiological and pathological states more pronounced. Raising instead of lowering the
 599 maximal value of the chemosensation sigmoid, i.e. setting $\phi = 5$ nS (and $\theta_g = 50$ mmHg),
 600 results in a closed-loop model with bistable eupneic bursting and a depolarized (-30 mV)
 601 quiescent state of the CPG. We interpret this quiescent state, for which lung volume is
 602 constant at 3.1 liters, as apneusis. Finally, we also considered a bell-shaped curve instead
 603 of a sigmoid for the relationship between g_{tonic} and P_aO_2 , and observed bistability between
 604 eupneic bursting and a hyperpolarized (-60 mV) quiescent state of the CPG. We interpret
 605 this quiescent state, for which lung volume is constant at 2.0 liters, as apnea. While we
 606 have not observed coexistence of more than two stable states in any of these versions of the
 607 closed-loop model, we cannot rule out the possibility of higher-order multistability.

608 *Control theory and averaging analysis*

609 Control theory is a promising framework for studying respiratory control, however it
 610 requires the part of control theory that involves nonlinear, nonstationary control (i.e. control
 611 of limit cycle trajectories), and possibly also stochastic control—which means the control
 612 theoretical framework needed is not yet complete (Cowan et al., 2014; Roth et al., 2014).
 613 In our closed-loop model, P_aO_2 is the natural “control variable”: it carries the signal that
 614 regulates the activity of the CPG (as opposed to P_AO_2 or lung volume being the feedback
 615 signals). Although there is no canonical way to partition fast and slow variables in a high-
 616 dimensional system of ODEs (Clewley et al., 2005), empirical investigation (Fig. 16) suggests
 617 P_aO_2 is also a reasonable candidate for consideration as the slow variable. Identification of
 618 a slow variable suggests analysis *via* averaging. In this case, averaging gives a qualitative
 619 insight into the nature of the bistability between eupnea and tachypnea, interpreted along the
 620 P_aO_2 “phase line” (Fig. 7). However, the resulting behaviors are not fixed points but limit
 621 cycles, and the averaging analysis with a single slow variable does not give full quantitative

622 agreement. An averaging analysis considering multiple slow variables (Wang and Rubin,
623 2016), which lies beyond the scope of the present paper, may be able to more faithfully
624 capture the chain of dependencies present in the closed-loop model.

625 It is both conceptually and mathematically convenient that the slow variables coincide
626 with the control variables for this system, and we suggest that it may be useful to look
627 for this feature in other motor control systems, such as those involved in legged locomotion
628 (Full and Koditschek, 1999).

629 **Closed-loop respiratory control models**

630 Although the literature on computational modeling of the respiratory system is vast
631 (Lindsey et al., 2012), the model analyzed here is, to our knowledge, the first to embed
632 a conductance-based CPG capable of firing action potentials into a closed-loop respiratory
633 control model. Most computational studies have focused on respiratory pattern generation
634 rather than the neural response to changes in blood gases (Ben-Tal and Tawhai, 2013).
635 Furthermore, much of the work that treats the respiratory system from a control-theoretic
636 perspective (Grodins, 1963) predates the identification of the preBötzinger complex as the
637 main location of the rhythmic pattern generation circuitry (Smith et al., 1991). In early
638 dynamical models of the respiratory control loop, neuronal activity was represented by time
639 delays between different compartments (Grodins et al., 1954, 1967), or as a black-box rhythm
640 generator (Khoo, 1990; Cheng et al., 2010). Later models incorporated neuronal dynamics
641 using a generic limit cycle oscillator (Eldridge, 1996) or firing rate models of excitatory and
642 inhibitory neurons (Longobardo et al., 2005) as the respiratory pattern generator. Ben-Tal
643 and Smith (2008) developed the first closed-loop model with a rhythm generator based on
644 the persistent sodium current (I_{NaP}) that plays a major role in bursting of brainstem pBC
645 neurons. The Ben-Tal model used a reduced description of the BRS model that did not
646 include the ionic currents needed to produce action potentials. Instead, the activity level is
647 described by a variable that represents the average spike rate of the pBC population, which
648 can be related to the average voltage by a linear transformation. Two closed-loop models
649 with detailed respiratory neuronal networks are the O’Connor et al. (2012) and Molkov et
650 al. (2014) models. Both include the pBC as well as other brainstem neuronal populations
651 involved in pattern generation, such as the Bötzing complex and the ventral respiratory

652 column. However, neither model simulates action potential-like spikes. The O’Connor model
653 employed interacting populations of integrate-and-fire neurons where spikes are implied by
654 voltage threshold crossings. The Molkov model used an activity-based neuron formalism
655 in which the voltage variable represents an average voltage for the population, and the
656 population firing rate is described by a function of the voltage variable. As discussed in
657 the previous section, in our model we find that replacing the full conductance-based model
658 with a lower-dimensional model obtained by averaging reproduces the qualitative but not
659 quantitative aspects of the full model.

660 It is possible that several of the features of the closed-loop model explored in this paper,
661 such as bistability and spontaneous autoresuscitation, would still be present in a version of
662 the model where the ionic currents responsible for action potential firing of the CPG have
663 been removed. We choose to retain the spikes, as it has been shown that reduced models
664 of bursting cells (the R15 neuron in *Aplysia californica*) that do not consider the effects of
665 action potentials on the underlying slow-wave oscillation in membrane potential may wrongly
666 predict transitions between quiescent, bursting, and beating activity modes compared to the
667 full model (Butera et al., 1996). In the BRS model, creating a “spikeless” reduced model by
668 removing the transient sodium current I_{Na} yields a slow-wave membrane potential oscillation
669 with a period that is approximately twice that of the full model (Ermentrout and Terman,
670 2010). The full model has a shorter period relative to the reduced model because action
671 potentials intensify the inactivation of the pacemaking persistent sodium current I_{NaP} .

672 **Physiology of Autoresuscitation**

673 Autoresuscitation occurs when the confluence of chemosensory drive and centrally gen-
674 erated drive causes a restart of the respiratory network. Typically, this restart occurs after
675 the decreased oxygen tension is sensed via the carotid bodies and low O_2 drives the hypoxic
676 ventilatory response (HVR), consisting of two distinct phases: Phase 1, an acute increase
677 in minute ventilation early after hypoxic exposure, and Phase 2, a later response character-
678 ized by ventilatory depression. In most mammals, the HVR is fully mature by two weeks
679 of postnatal life (Prabhakar et al., 2007). However, in neonatal mammals with immature
680 chemosensory feedback, the reduced drive to the CPG is likely the key failure point that re-
681 duces the probability of restarting the respiratory rhythm in response to severe hypoxia (i.e.,

682 anoxia). Serotonergic and adrenergic neuromodulatory inputs appear to play a key role and
683 are developmentally regulated (Erickson and Sposato, 2009; Givan and Cummings, 2016).
684 Other complications of neonatal life, including infection (Siljehav et al., 2014), confound our
685 understanding of the points of failure in the respiratory control system. As of yet, we do not
686 have a mechanistic understanding of why autoresuscitation sometimes fails and sometimes
687 succeeds. Our model provides greater understanding of the state changes that are required
688 for resuscitation, and an impetus for future experiments dedicated to elucidating the key
689 control points that can force the respiratory network into restart after a hypoxic challenge.

690 Development

691 Developmental changes in the respiratory rhythm-generating and pattern formation net-
692 works have been described, but we do not yet know the impact that these changes have on
693 the core of the rhythm-generating circuit. For example, burst-generating currents, including
694 I_{NaP} and I_{CAN} (Ca^{2+} -activated nonselective cation) currents, are modulated during devel-
695 opment (Del Negro et al., 2005). Furthermore, fetal hemoglobin is known to have a higher
696 binding affinity for oxygen, and the time course by which fetal hemoglobin shifts to pre-
697 dominantly adult hemoglobin would impact autoresuscitation (Rutland et al., 1983; Teitel
698 and Rudolph, 1985). Developmental changes in chemosensation also are key modifiers of
699 autoresuscitation, as mentioned above. Carotid body resetting—after the relatively hypoxic
700 environment *in utero*—occurs over the first weeks of life (Prabhakar et al., 2007), and the
701 chronic intermittent hypoxic events common in neonates can alter the gain of carotid body
702 chemosensors (Pawar et al., 2008). In our closed-loop model, changes in the gain of the hy-
703 poxia sensitive pathway would correspond to changes in the slope of the sigmoid connecting
704 P_{aO_2} to g_{tonic} (the parameter σ_g in (22)). Additionally, hypoxia alters gene transcription
705 and reactive oxygen species (ROS)-mediated signaling. Relatively little is known about how
706 the respiratory control circuit changes, as a whole, over the course of development from the
707 perinatal period to adulthood.

708 In our closed-loop model, the ability of the system to recover from an interruption in
709 chemosensory feedback failure depends on the constant value assumed for g_{tonic} when dis-
710 connected from P_{aO_2} (Fig. 14). If this value is in the range that produces bursting in the
711 isolated CPG (between 0.25 and 0.4 nS), then the closed-loop system always returns to

712 eupnea following chemosensory interruption. Based on this observation, we speculate that
713 there may be at least two distinct components of carotid body input to the brainstem: an
714 excitatory drive that is independent of chemosensory feedback, and a modulatory pathway
715 to confer additional robustness. The former would be an example of open-loop control,
716 and may be dominant during early stages of development; whereas the latter would reflect
717 closed-loop control, and may be more prominent in later stages of development.

718 **Periodic breathing**

719 In the closed-loop model, a stable bursting limit cycle (eupnea) coexists with a sta-
720 ble tonic spiking limit cycle (tachypnea). On the boundary between the basins of attrac-
721 tions of two different stable limit cycles, one may “generically” expect to find an unstable
722 limit cycle solution—just as we have observed (Benes et al., 2011). Indeed, in many neu-
723 ronal models, the transition between bursting and spiking exhibits complicated dynamics
724 (Ermentrout and Terman, 2010). Recently, it has been shown that a common dynamical
725 phenomenon, the *torus canard*, separates bursting and spiking regimes in several neuronal
726 models (Kramer et al., 2008; Burke et al., 2012). Torus canards have been found in classes
727 of neuronal models where the active phase of bursting terminates in a saddle-node bifurca-
728 tion of periodic orbits (a fold-cycle bifurcation) in the fast subsystem, such as subcritical-
729 Hopf/fold-cycle, circle/fold-cycle, and fold/fold-cycle bursters. In contrast, the BRS model
730 is a fold/homoclinic (square wave) burster, i.e. the active phase of bursting terminates at
731 a homoclinic bifurcation. In the BRS model, there is a fold-cycle bifurcation in the fast
732 subsystem, however the active phase of bursting does not terminate there, and it is not clear
733 whether the torus canard phenomenon is possible in the closed-loop model presented here.
734 Although the single-neuron version of the BRS model exhibits fold/homoclinic bursting, two
735 synaptically coupled BRS model neurons exhibit fold/fold-cycle (or top hat) bursting (Best
736 et al., 2005). A recent study (Roberts et al., 2015) has linked the transitions between bursting
737 and spiking in the coupled BRS model to folded singularities and canards. Thus, we expect
738 that torus canards may be present in a version of the closed-loop model where the CPG is a
739 network of BRS neurons, rather than a single representative neuron. In systems with torus
740 canards, trajectories can make extended visits to the neighborhood of an attracting limit
741 cycle and a repelling limit cycle in alternation (Benes et al., 2011). Such dynamics in a res-

742 piratory control loop might provide a model of periodic breathing, a phenomenon commonly
743 observed in premature infants where pauses in breathing of up to 10 seconds are followed
744 by a series of rapid, shallow breaths before breathing returns to normal (Mohr et al., 2015;
745 Patel et al., 2016). The typical phenotype of periodic breathing—apneas interspersed with
746 tachypneic episodes—is also seen in adults as Cheyne-Stokes breathing. Hypoxic episodes
747 have been implicated in the early stages of Cheyne-Stokes breathing, and may be essential
748 to the initiation of these episodes, and the downward spiral into pathophysiological rhythms
749 (Guntheroth, 2011).

750 **Robustness and flexibility**

751 Lyttle et al. (2016) recently introduced a dynamical systems framework for character-
752 izing the robustness and flexibility of motor control systems. They defined *robustness* as
753 the ability of a system to maintain performance despite perturbations (or parameter varia-
754 tion), and *flexibility* as the ability of a system to deploy alternative strategies that improve
755 performance by adjusting behavioral output in response to perturbations. A third concept,
756 *sensitivity*, measures the extent to which the dynamics of system components change in
757 response to perturbations. Using a model of an invertebrate feeding apparatus, Lyttle et al.
758 (2016) demonstrated that motor control systems can achieve robustness and flexibility by
759 dynamically switching between coexisting modes in response to changing demands. One of
760 these modes is characterized by low sensitivity to perturbations and parameter variations,
761 and the other mode by high sensitivity.

762 Interpreting our respiratory control model in this framework raises interesting questions.
763 We have shown that the closed-loop system is more *robust* to changes in metabolic demand
764 (M) than the open-loop system, because it is able to maintain blood oxygen within accept-
765 able limits (80 to 110 mmHg) over a wider range of M values (Fig. 8). However, once M
766 exceeds a certain value ($1.24 \times 10^{-7} \text{ ms}^{-1}$), then $P_a\text{O}_2$ drops precipitously in the closed-loop
767 model, and for M values above this threshold the $P_a\text{O}_2$ levels in the open-loop model are
768 higher than they are in the closed-loop model. This suggests that respiratory system per-
769 formance might improve if the system were to modulate its sensitivity by reducing the gain
770 of chemosensory feedback (σ_g) as metabolic demand increases, paradoxically enabling it to
771 postpone a collapse in $P_a\text{O}_2$ by switching to more of an open-loop control regime. Additional

772 feedback mechanisms on a longer time scale could potentially confer such flexibility.

773 As another point of comparison, Fig. 10 illustrates the mechanism by which sensory
774 feedback allows the closed-loop respiratory system to respond to what Lyttle et al. (2016)
775 calls a “challenge”, that is, a perturbation that tends to decrease the system’s performance
776 (in this case, maintenance of adequate P_aO_2 levels). Imposing a hypoxic challenge leads to
777 the system producing a longer and stronger motor response that effectively counteracts the
778 perturbation, within certain amplitude limits. The role of sensory feedback in (Lyttle et
779 al., 2016) is qualitatively similar. In that system, applying a mechanical load opposing the
780 pulling in of food, during the swallowing phase of an ingestive motor pattern, activates a
781 proprioceptive input to the CPG that selectively extends a portion of the underlying limit
782 cycle trajectory. In response, the central pattern generator produces a longer and stronger
783 activation of the motor units innervating muscles opposed to the mechanical challenge.

784 **Model extensions**

785 There are several aspects of the respiratory control network that could be incorporated in
786 future work extending our closed-loop model. These include modeling the pBC as a multi-
787 unit network with parametric heterogeneity, which has been shown to increase the robustness
788 of inspiratory oscillations in a network of model conditional pacemaker neurons (Rubin and
789 Terman, 2002b); interaction of the pBC with other brainstem nuclei such as the ventral
790 respiratory column and the retrotrapezoid nucleus, which can lead to a variety of multiphasic
791 rhythms (Rubin et al., 2009); changes in cellular properties in response to hypoxia (Mironov
792 et al., 1998; Mironov and Richter, 1998); and additional sensory feedback pathways involving
793 carbon dioxide sensing (Molkov et al., 2014) and lung/chest/abdominal stretch receptors
794 (Paintal, 1973; Widdicombe, 1982; Coleridge and Coleridge, 1994; Schlafke and Koepchen,
795 1996).

796 These extensions would introduce challenges in the mathematical analysis of the result-
797 ing model. For example, inclusion of lung volume feedback modulation of inspiratory drive
798 yields a closed-loop model with a mechanical control problem nested within the blood gas
799 homeostatic control problem. Moreover, additional sensory feedback pathways may not
800 converge on the same input (g_{tonic}) used as the control variable in the present paper. Incorporating
801 multiple control pathways will significantly complicate the averaging analysis, just

802 as systems with multiple slow variables are more challenging to analyze through fast-slow
803 dissection than systems with a single slow variable (Bertram and Rubin, 2016). However
804 what we would expect to carry over to a more elaborate model is that the timing of the
805 sensory feedback, or different components of sensory feedback, would still be expected to
806 play the predominant role in setting the timing of respiration rather than intrinsic properties
807 of the central pattern generator in isolation.

808 APPENDIX

809 To better understand the nature of the bistability between normal and reduced P_aO_2
810 levels, we performed a fast-slow decomposition of the closed-loop system, treating P_aO_2
811 as the slow variable and then approximating its dynamics using the method of averaging
812 (Sanders et al., 2007).

813 Fast-slow decomposition

814 The application of singular perturbation methods developed by Fenichel and others (Ru-
815 bin and Terman, 2002a; Fenichel, 1979; Jones, 1995; Wiggins, 1994) has led to rapid
816 advances in understanding the geometry of bursting dynamics in numerous neural oscilla-
817 tors admitting a time scale separation between “slow” and “fast” variables (Borisjuk and
818 Rinzel, 2005; Coombes and Bressloff, 2005; Izhikevich, 2000; Rinzel and Ermentrout, 1989;
819 Bertram and Rubin, 2016). The global structure of the flows in such systems is determined
820 by the “slow” variables, for instance the persistent sodium gating variable h in the isolated
821 BRS model (Best et al., 2005). In the case of a respiratory control loop, we embed the BRS
822 model into a system including time scales for gas exchange, lung mechanics, and metabolic
823 consumption of O_2 . What is, or what are, the “slow variables” in such a control system?

824 The closed-loop model is a 7-dimensional system of ordinary differential equations (ODEs)
825 that includes time scales for a variety of processes (neuronal dynamics, lung mechanics, gas
826 exchange, and metabolic consumption of oxygen), and several different partitions of the
827 system into fast and slow subsystems are possible. In order to place disparate variables on
828 a common basis, we calculated the *maximum relative speed* of the variable, ν_x , defined as

829 the maximum rate of change divided by the range of the variable. Formally,

$$\nu_x = \frac{\max_{t \in [0, T]} \{|x'(t)|\}}{\max_{t \in [0, T]} \{x(t)\} - \min_{t \in [0, T]} \{x(t)\}}, \quad (24)$$

830 where $x'(t)$ is the time derivative dx/dt . The smaller ν_x is, the “slower” we consider x to be.

831 We find that during eupneic bursting, the intrinsic slowness of the variables span multiple

832 temporal scales, with P_aO_2 , vol_L , and P_AO_2 being an order of magnitude slower than h and

833 α , which in turn are an order of magnitude slower than v and n (Fig. 16 and Table I).

x	$\max_{t \in [0, T]} \{ x'(t) \}$	$\max_{t \in [0, T]} \{x(t)\}$	$\min_{t \in [0, T]} \{x(t)\}$	ν_x
P_aO_2	0.0278	105.7054	93.3442	0.0022
vol_L	0.0022	2.9744	2.0078	0.0023
P_AO_2	0.0349	107.2739	94.5528	0.0027
h	0.0035	0.7551	0.6734	0.0427
α	7.0518×10^{-4}	0.0090	3.5427×10^{-5}	0.0783
v	76.2152	6.3719	-59.7198	1.1532
n	1.7849	0.9386	4.6197×10^{-4}	1.9027

Table I. **Comparing the “relative speed” of the closed-loop model variables.** The dimensionless quantity ν_x of each variable in the model along the eupneic bursting limit cycle of period T is calculated using equation (24).

834 Averaging analysis

835 To set up an averaging calculation to obtain the approximate dynamics of the control

836 variable, $y = P_aO_2$, we write the closed-loop model in the following form:

$$\frac{dx}{dt} = f(x, y) \quad (25)$$

$$\frac{dy}{dt} = g(x, y). \quad (26)$$

837 where $x = (V, h, n, \alpha, \text{vol}_L, P_AO_2)$ play the role of the dependent variables. The control

838 variable, $y = P_aO_2$, is held constant and the dependent variables are allowed to evolve

839 freely. The dependent subsystem $dx/dt = f(x, y)$ will evolve either to a fixed point or to a

840 (beating or bursting) limit cycle. If the dependent subsystem has a fixed point, then

$$\frac{dy}{dt} = \bar{g}(y) = g(O^*(y), y) \quad (27)$$

841 is the reduced system for the evolution of the control variable, where $O^*(y)$ is the (y -
 842 dependent) value of lung oxygen at the fixed point. If the dependent subsystem has a limit
 843 cycle $\gamma_y(t)$ with period $T(y)$, we obtain $\bar{g}(u)$ by numerically integrating $g(\gamma_u(t), u)$ over one
 844 period $T(u)$

$$\bar{g}(u) = \frac{1}{T(u)} \int_{t=0}^{T(u)} g(\gamma_u(t), u) dt, \quad (28)$$

845 and the averaged equation for the dynamics of the control variable is

$$\frac{d\bar{y}}{dt} \approx \bar{g}(\bar{y}). \quad (29)$$

846 Floquet analysis

847 The stability of periodic solutions can be determined using Floquet theory (Perko, 2001).
 848 Suppose we have a period T limit cycle solution $x = \gamma(t)$ of a system $\dot{x} = f(x)$, $x \in \mathbb{R}^n$.
 849 The linearization of the dynamics around the limit cycle are $A(t) = D_x f(\gamma(t))$, giving the
 850 periodically forced linear system

$$\dot{u} = A(t)u, \quad (30)$$

851 with the fundamental matrix $\Phi(t)$ satisfying

$$\dot{\Phi} = A(t)\Phi, \quad \Phi(0) = I. \quad (31)$$

852 Floquet's theorem says we can write Φ as

$$\Phi(t) = Q(t)e^{Bt}, \quad (32)$$

853 where $Q(t)$ is T -periodic and B is a constant matrix. The eigenvalues of e^{Bt} are the Floquet
 854 multipliers μ_1, \dots, μ_n and they describe the cycle-to-cycle growth or decay of perturbations.
 855 One multiplier will be unity, corresponding to perturbations along $\gamma(t)$. If any of the re-
 856 maining multipliers have $|\mu| > 1$ then the periodic solution is unstable.

857 In the closed-loop model, D_x is undefined at the transition from inspiration to expiration
 858 because the right hand side of (14) is nondifferentiable at that point. Thus, instead of solving
 859 the variational equation we compute Floquet multipliers through perturbation and direct
 860 simulation of the system equations alone. We start at a point x_0 on the limit cycle, and solve
 861 the initial value problem from 0 to T with $x_0 + \hat{e}_k \varepsilon$ for $k = 1, \dots, 7$. The \hat{e}_k are unit vectors,
 862 and ε must be small enough that we stay close to the limit cycle for one period, but large

863 enough that we are not overwhelmed by roundoff error. For the limit cycle on the boundary
 864 between eupnea and tachypnea, the period T is 1818.5 ms, and we have found $\varepsilon = 10^{-7}$
 865 to work well. We also simulate the unperturbed system, which after one period returns to
 866 $x_T \approx x_0$. Let x_k be the solution starting from $x_0 + \hat{e}_k \varepsilon$. Then the seven vectors $x_k - x_T$ form
 867 the columns of the (approximate) multiplier matrix, the eigenvalues of which are the Floquet
 868 multipliers. With x_0 located at arrow (b) in Fig. 13A ($v = -50.9617, n = 0.0041, h =$
 869 $0.5126, \alpha = 0.0012, \text{vol}_L = 2.2660, P_A \text{O}_2 = 78.0837, P_a \text{O}_2 = 77.2000$), the following Floquet
 870 multipliers μ_1, \dots, μ_7 were obtained: 1.37, 1.00, 0.49, $-0.01 + 0.01i$, $-0.01 - 0.01i$, 0.00, and
 871 0.00. Since $\mu_1 > 1$, we conclude that the limit cycle on the boundary between eupnea and
 872 tachypnea is unstable. Associated with each multiplier is an eigenvector ξ_i satisfying

$$e^{BT} \xi_i = \mu_i \xi_i. \quad (33)$$

873 The components of ξ_1 contain information about how influential each of the 7 closed-loop
 874 variables is in determining whether trajectories perturbed off of the boundary limit cycle
 875 will head towards eupnea or tachypnea. To ensure a fair comparison of the components,
 876 we rescaled the eigenvectors using scaling factors s_i defined as the magnitude of the change
 877 in each variable during one unperturbed period of the unstable limit cycle. The rescaled
 878 eigenvectors ζ_i are given by:

$$\zeta_i = \frac{S^{-1} \xi_i}{\|S^{-1} \xi_i\|} \quad (34)$$

879 with scaling matrix $S = \text{diag}(s_1, \dots, s_7)$. The components of ζ_1 computed with x_0 located
 880 at 4 different points along the boundary limit cycle (arrows b–e in Fig. 13A) are shown in
 881 Fig. 13B–E.

882 ACKNOWLEDGEMENTS

883 This work originated as an externally mentored postdoctoral project through the Math-
 884 ematical Biosciences Institute (NSF grant DMS-1440386), and was partially supported by
 885 NSF grants DMS-1413770 (PJT), DMS-1412877 (COD), and DMS-155237 (COD). We thank
 886 Catherine A. Mayer and Paulina Getsy for technical assistance with the *in vitro* experiments,
 887 Joseph C. LaManna for helpful technical discussions, and Patricia O’Callaghan for a critical
 888 reading of the manuscript.

889 REFERENCES

- 890 **Bässler U.** On the definition of central pattern generator and its sensory control. *Biol*
891 *Cybern* 54: 65–69, 1986.
- 892 **Ben-Tal A, Smith J.** A model for control of breathing in mammals: coupling neural
893 dynamics to peripheral gas exchange and transport. *J Theor Biol* 251: 480–497, 2008.
- 894 **Ben-Tal A, Tawhai M.** Integrative approaches for modeling regulation and function of
895 the respiratory system. *Wiley Interdiscip Rev Syst Biol Med* 5: 687–699, 2013.
- 896 **Benes G, Barry A, Kaper T, Kramer MA, Burke J.** An elementary model of torus
897 canards. *Chaos* 21: 023131, 2011.
- 898 **Bertram R, Rubin J.** Multi-timescale systems and fast-slow analysis. *Math Biosci* doi:
899 10.1016/j.mbs.2016.07.003, 2016.
- 900 **Bertram R, Butte M, Kiemel T, Sherman A.** Topological and phenomenological
901 classification of bursting oscillations. *Bull Math Biol* 57: 413–439, 1995.
- 902 **Best J, Borisyuk A, Rubin J, Terman D, Wechselberger M.** The dynamic range of
903 bursting in a model respiratory pacemaker network. *SIAM J Appl Dyn Syst* 4: 1107–1139,
904 2005.
- 905 **Borisyuk A, Rinzel J.** Understanding neuronal dynamics by geometrical dissection of
906 minimal models In: *Models and Methods in Neurophysics, Proc Les Houches Summer*
907 *School 2003, (Session LXXX)*, p. 19–72. Elsevier, 2005.
- 908 **Burke J, Desroches M, Barry A, Kaper TJ, Kramer MA.** A showcase of torus
909 canards in neuronal bursters. *J Math Neurosci* 2: 3, 2012.
- 910 **Butera J RJ, Clark J JW, Byrne JH.** Dissection and reduction of a modeled bursting
911 neuron. *J Comput Neurosci* 3: 199–223, 1996.
- 912 **Butera Jr. RJ, Rinzel J, Smith JC.** Models of respiratory rhythm generation in the
913 preBötzinger complex. I. bursting pacemaker neurons. *J Neurophysiol* 82: 382–397, 1999a.
- 914 **Butera Jr. RJ, Rinzel J, Smith JC.** Models of respiratory rhythm generation in the
915 preBötzinger complex. II. populations of coupled pacemaker neurons. *J Neurophysiol* 82:
916 398–415, 1999b.
- 917 **Cheng L, Ivanova O, Fan H, Khoo M.** An integrative model of respiratory and car-
918 diovascular control in sleep-disordered breathing. *Respir Physiol Neurobiol* 174: 4–28,
919 2010.

920 **Clewley R, Rotstein HG, Kopell N.** A computational tool for the reduction of nonlinear
921 ODE systems possessing multiple scales. *Multiscale Model Simul* , 2005.

922 **Coleridge H, Coleridge J.** Pulmonary reflexes: neural mechanisms of pulmonary defense.
923 *Annu Rev Physiol* 56: 69–91, 1994.

924 **Coombes S, Bressloff PC (Eds.).** *Bursting: The Genesis of Rhythm in the Nervous*
925 *System.* World Scientific, 2005.

926 **Cowan NJ, Ankarali MM, Dyhr JP, Madhav MS, Roth E, Sefati S, Sponberg S,**
927 **Stamper SA, Fortune ES, Daniel TL.** Feedback control as a framework for under-
928 standing tradeoffs in biology. *Integr Comp Biol* 54: 223–237, 2014.

929 **D’Agostino D, Mazza E, Neubauer JA.** Heme oxygenase is necessary for the excitatory
930 response of cultured neonatal rat rostral ventrolateral medulla neurons to hypoxia. *Am J*
931 *Physiol Regul Integr Comp Physiol* 296: R102–R118, 2009.

932 **Del Negro CA, Morgado-Valle C, Hayes JA, Mackay DD, Pace RW, Crowder EA,**
933 **Feldman JL.** Sodium and calcium current-mediated pacemaker neurons and respiratory
934 rhythm generation. *J Neurosci* 25: 446–453, 2005.

935 **Diekman CO, Wilson CG, Thomas PJ.** Spontaneous autoresuscitation in a model of
936 respiratory control *Conf Proc IEEE Eng Med Biol Soc* 2012: 6669–6672, 2012.

937 **Dunmyre JR, Del Negro CA, Rubin JE.** Interactions of persistent sodium and calcium-
938 activated nonspecific cationic currents yield dynamically distinct bursting regimes in a
939 model of respiratory neurons. *J Comput Neurosci* 31: 305–328, 2011.

940 **Eldridge F.** The North Carolina respiratory model. a multipurpose model for studying
941 the control of breathing. In: *Bioengineering Approaches to Pulmonary Physiology and*
942 *Medicine*, edited by Khoo M. Plenum Press, 1996 p. 25–49.

943 **Erickson JT, Sposato BC.** Autoresuscitation responses to hypoxia-induced apnea are
944 delayed in newborn 5-ht-deficient pet-1 homozygous mice. *J Appl Physiol* 106: 1785–1792,
945 2009.

946 **Ermentrout B.** *Simulating, Analyzing, and Animating Dynamical Systems: A Guide to*
947 *XPPAUT for Researchers and Students.* SIAM, 2002.

948 **Ermentrout GB, Terman DH.** *Mathematical Foundations Neuroscience.* Springer, 2010.

949 **Feldman JL, Del Negro CA, Gray PA.** Understanding the rhythm of breathing: so
950 near, yet so far. *Annu Rev Physiol* 75: 423–452, 2013.

951 **Fenichel N.** Geometric singular perturbation theory for ordinary differential equations. *J*

952 *Diff Eq* 31: 53–98, 1979.

953 **Full RJ, Koditschek DE.** Templates and anchors: neuromechanical hypotheses of legged
954 locomotion on land. *J Exp Biol* 202: 3325–3332, 1999.

955 **Gaspard P.** Measurement of the instability rate of a far-from-equilibrium steady state at
956 an infinite period bifurcation. *J Phys Chem* 94: 1–3, 1990.

957 **Givan SA, Cummings KJ.** Intermittent severe hypoxia induces plasticity within sero-
958 tonergic and catecholaminergic neurons in the neonatal rat ventrolateral medulla. *J Appl*
959 *Physiol* 120: 1277–1287, 2016.

960 **Grodins F.** *Control Theory and Biological Systems*. Columbia University Press, 1963.

961 **Grodins F, Buell J, Bart A.** Mathematical analysis and digital simulation of the respi-
962 ratory control system. *J Appl Physiol* 22: 260–276, 1967.

963 **Grodins F, Gray J, Schroeder K, Norins A, Jones R.** Respiratory responses to
964 CO₂ inhalation: a theoretical study of a nonlinear biological regulator. *J Appl Physiol* 7:
965 283–308, 1954.

966 **Guntheroth WG.** Cheyne–Stokes respiration: hypoxia plus a deep breath that interrupts
967 hypoxic drive, initiating cyclic breathing. *Med Hypotheses* 77: 714–716, 2011.

968 **Hlastala MP, Berger AJ.** *Physiology of Respiration*. Oxford University Press, 2001.

969 **Izhikevich EM.** Neural excitability, spiking, and bursting. *Int J Bif Chaos* 10: 1171–1266,
970 2000.

971 **Izhikevich EM.** *Dynamical Systems in Neuroscience: The Geometry of Excitability and*
972 *Bursting*. Cambridge: MIT Press, 2007.

973 **Jones C.** Geometric singular perturbation theory. In: *Dynamical Systems*, No. 1609 of
974 *Lecture Notes in Mathematics*, edited by Johnson R. Berlin: Springer, 1995, p. 44–118.

975 **Kandel ER, Schwartz JH, Jessell TM.** *Principles of Neural Science*. New York: Else-
976 vier, 1991.

977 **Keener J, Sneyd J** *Mathematical Physiology, Vol. II. Systems Physiology*. New York:
978 Springer, 2009.

979 **Khoo M.** A model-based evaluation of the single-breath CO₂ ventilatory response test. *J*
980 *Appl Physiol* 68: 393–399, 1990.

981 **Koizumi H, Wilson CG, Wong S, Yamanishi T, Koshiya N, Smith JC.** Functional
982 imaging, spatial reconstruction, and biophysical analysis of a respiratory motor circuit
983 isolated in vitro. *J Neurosci* 28: 2353–2365, 2008.

984 **Koshiya N, Smith JC.** Neuronal pacemaker for breathing visualized in vitro. *Nature* 400:
985 360–363, 1999.

986 **Kramer MA, Traub RD, Kopell N.** New dynamics in cerebellar purkinje cells: Torus
987 canards. *Phys Rev Lett* 101: 068103, 2008.

988 **Lindsey B, Rybak I, Smith J.** Computational models and emergent properties of respi-
989 ratory neural networks. *Compr Physiol* 2: 1619–1670, 2012.

990 **Longobardo G, Evangelisti C, Cherniack N.** Introduction of respiratory pattern gen-
991 erators into models of respiratory control. *Respir Physiol Neurobiol* 148: 285–301, 2005.

992 **Lyttle DN, Gill JP, Shaw KM, Thomas PJ, Chiel HJ.** Robustness, flexibility, and
993 sensitivity in a multifunctional motor control model. *Biol Cybern* p. 1–23, 2016.

994 **Martin RJ, Di Fiore J, MacFarlane PM, Wilson C.** Physiologic basis for intermittent
995 hypoxic episodes in preterm infants. *Adv Exp Med Biol* 758: 351–358, 2012.

996 **Mironov S, Langohr K, Haller M, Richter D.** Hypoxia activates ATP-dependent
997 potassium channels in inspiratory neurones of neonatal mice. *J Physiol* 509: 755–766,
998 1998.

999 **Mironov S, Richter D.** L-type Ca²⁺ channels in inspiratory neurones of mice and their
1000 modulation by hypoxia. *J Physiol* 512: 75–87, 1998.

1001 **Mironov S, Richter D.** Intracellular signalling pathways modulate K(ATP) channels in
1002 inspiratory brainstem neurones and their hypoxic activation: involvement of metabotropic
1003 receptors, G-proteins and cytoskeleton. *Brain research* 853: 60–67, 2000.

1004 **Mironov S, Richter D.** Oscillations and hypoxic changes of mitochondrial variables in
1005 neurons of the brainstem respiratory centre of mice. *J Physiol* 533: 227–236, 2001.

1006 **Mohr MA, Fairchild KD, Patel M, Sinkin RA, Clark MT, Moorman JR, Lake
1007 DE, Kattwinkel J, Delos JB.** Quantification of periodic breathing in premature infants.
1008 *Physiol Meas* 36: 1415, 2015.

1009 **Molkov Y, Shevtsova N, Park C, Ben-Tal A, Smith J, Rubin J, Rybak I.** A
1010 closed-loop model of the respiratory system: focus on hypercapnia and active expiration.
1011 *PLOS One* 9: e109894, 2014.

1012 **O’Connor R, Segers L, Morris K, Nuding S, Pitts T, Bolser D, Davenport P,
1013 Lindsey B.** A joint computational respiratory neural network-biomechanical model for
1014 breathing and airway defensive behaviors. *Front Physiol* 3: 264, 2012.

1015 **Paintal A.** Vagal sensory receptors and their reflex effects. *Physiol Rev* 53: 159–227, 1973.

1016 **Patel M, Mohr M, Lake D, Delos J, Moorman JR, Sinkin RA, Kattwinkel J,**
1017 **Fairchild K.** Clinical associations with immature breathing in preterm infants: part
1018 2-periodic breathing. *Pediatr Res* , 2016.

1019 **Pawar A, Peng YJ, Jacono FJ, Prabhakar NR.** Comparative analysis of neonatal
1020 and adult rat carotid body responses to chronic intermittent hypoxia. *J Appl Physiol* 104:
1021 1287–1294, 2008.

1022 **Perko LJ.** *Differential Equations and Dynamical Systems*. New York: Springer-Verlag,
1023 2001.

1024 **Prabhakar NR, Peng YJ, Kumar GK, Pawar A.** Altered carotid body function by
1025 intermittent hypoxia in neonates and adults: relevance to recurrent apneas. *Respir Physiol*
1026 *Neurobiol* 157: 148–153, 2007.

1027 **Ramirez JM, Telgkamp P, Elsen FP, Quellmalz UJ, Richter DW.** Respiratory
1028 rhythm generation in mammals: synaptic and membrane properties. *Respir Physiol* 110:
1029 71–85, 1997.

1030 **Rinzel J.** A formal classification of bursting mechanisms in excitable systems In: *Mathemat-*
1031 *ical Topics in Population Biology, Morphogenesis, and Neurosciences*, Vol. 71 of *Lecture*
1032 *Notes in Biomathematics*, edited by Teramoto E, Yamaguti M. Berlin: Springer-Verlag,
1033 1987.

1034 **Rinzel J, Ermentrout G.** Analysis of neural excitability and oscillations In: *Methods in*
1035 *Neuronal Modeling*, edited by Koch C, Segev I. MIT Press, 1989.

1036 **Roberts KL, Rubin JE, Wechselberger M.** Averaging, folded singularities, and torus
1037 canards: explaining transitions between bursting and spiking in a coupled neuron model.
1038 *SIAM J Appl Dyn Syst* 14: 1808–1844, 2015.

1039 **Roth E, Sponberg S, Cowan N.** A comparative approach to closed-loop computation.
1040 *Curr Opin Neurobiol* 25: 54–62, 2014.

1041 **Rubin J, Terman D.** Geometric singular perturbation analysis of neuronal dynamics In:
1042 *Handbook of Dynamical Systems, Vol. 2: Towards Applications*, edited by Fiedler B. El-
1043 sevier, 2002a, p. 93–146.

1044 **Rubin J, Terman D.** Synchronized activity and loss of synchrony among heterogeneous
1045 conditional oscillators. *SIAM J Appl Dyn Syst* 1: 146–174, 2002b.

1046 **Rubin JE, Shevtsova NA, Ermentrout GB, Smith JC, Rybak IA.** Multiple rhythmic
1047 states in a model of the respiratory central pattern generator. *J Neurophysiol* 101: 2146–65,

1048 2009.

1049 **Rutland P, Pembrey M, Davies T.** The estimation of fetal haemoglobin in healthy
1050 adults by radioimmunoassay. *Br J Haematol* 53: 673–682, 1983.

1051 **Rybak IA, Abdala APL, Markin SN, Paton JFR, Smith JC.** Spatial organization
1052 and state-dependent mechanisms for respiratory rhythm and pattern generation. *Prog*
1053 *Brain Res* 165: 201–220, 2007.

1054 **Sanders J, Verhulst F, Murdock J.** *Averaging Methods in Nonlinear Dynamical Systems.*
1055 New York: Springer, 2007.

1056 **Schläfke M, Koepchen H.** A systems view of respiratory regulation. In: *Comprehensive*
1057 *Human Physiology*, edited by Greger R, Windhorst U, 1996, p. 2097–2127.

1058 **Shimkin N,** Nonlinear control systems In: *Encyclopedia of Neuroscience*, edited by Binder
1059 M, Hirokawa N, Windhorst U. Springer, 2009, p. 2886–2889.

1060 **Siljehav V, Shvarev Y, Herlenius E.** Il-1 β and prostaglandin E2 attenuate the hyper-
1061 capnic as well as the hypoxic respiratory response via prostaglandin E receptor type 3 in
1062 neonatal mice. *J Appl Physiol* 117: 1027–1036, 2014.

1063 **Smith JC, Abdala APL, Koizumi H, Rybak IA, Paton JFR.** Spatial and func-
1064 tional architecture of the mammalian brain stem respiratory network: a hierarchy of three
1065 oscillatory mechanisms. *J Neurophysiol* 98: 3370–3387, 2007.

1066 **Smith JC, Butera RJ, Koshiya N, Del Negro C, Wilson CG, Johnson SM.** Respi-
1067 ratory rhythm generation in neonatal and adult mammals: the hybrid pacemaker-network
1068 model. *Respir Physiol* 122: 131–47, 2000.

1069 **Smith J, Ellenberger H, Ballanyi K, Richter D, Feldman J.** Pre-Bötzing complex:
1070 a brainstem region that may generate respiratory rhythm in mammals. *Science* 254:
1071 726–729, 1991.

1072 **Takakura AC, Moreira TS, West GH, Gwilt JM, Colombari E, Stornetta RL,**
1073 **Guyenet PG.** Gabaergic pump cells of solitary tract nucleus innervate retrotrapezoid
1074 nucleus chemoreceptors. *J Neurophysiol* 98: 374–381, 2007.

1075 **Teitel D, Rudolph A.** Perinatal oxygen delivery and cardiac function. *Adv Pediatr* 32:
1076 321–347, 1985.

1077 **Wang Y, Rubin J.** Multiple timescale mixed bursting dynamics in a respiratory neuron
1078 model. *J Comput Neurosci* 41: 245–268, 2016.

1079 **West JB.** *Respiratory Physiology: The Essentials* Lippincot Williams & Wilkins, 2008.

- 1080 **Widdicombe J.** Pulmonary and respiratory tract receptors. *J Exp Biol* 100: 41–57, 1982.
- 1081 **Wiggins S.** *Normally Hyperbolic Invariant Manifolds in Dynamical Systems*, No. 105 in
- 1082 *Applied Mathematical Sciences*. New York: Springer-Verlag, 1994.

Figure 1. **Schematic of closed-loop respiratory control model including neural, mechanical, and chemosensory components.** Bursting oscillations of the brainstem CPG membrane potential (V) activate motor neurons (α) to cause increases in lung volume (vol_L) and inspiration. Inhaled air increases alveolar oxygen partial pressure ($P_A\text{O}_2$). Oxygen enters the bloodstream through gas exchange. Arterial oxygen partial pressure ($P_a\text{O}_2$) is monitored by chemoreceptors that regulate input drive current (I_{tonic}) to the CPG by modulating excitatory synaptic conductances (g_{tonic}). This respiratory control circuit can maintain $P_A\text{O}_2$ levels in the desired range around 100 mmHg.

Figure 2. **Closed-loop bursting persists in the absence of the isolated CPG bursting mechanism.** **A:** Black traces show bursts of action potentials (V , top panel) in the closed-loop model with persistent sodium channel inactivation (h , middle panel) as a dynamic variable and a dynamic g_{tonic} (bottom panel) in response to changes in $P_a\text{O}_2$. **B:** Blue traces show bursting in the open-loop model with h as a dynamic variable and g_{tonic} set as a static parameter. **C:** Red traces show bursting in a version of the closed-loop model where h is set as a static parameter. This illustrates that the dynamical mechanism responsible for bursting in the open-loop model (slow h dynamics) is not required for bursting in the closed-loop model.

Figure 3. **Closed-loop bursting exists in the quiescent regime of the isolated CPG system.** Blue contour and vertical hatching indicate the range of values the dynamic variable h (abscissa) traverses as the static parameter g_{tonic} (ordinate) is varied in the open-loop model. For example, with g_{tonic} fixed at 0.3 nS, the CPG is bursting and h oscillates between 0.57 and 0.61. The blue dashed vertical lines demarcate regions of quiescence (Q), bursting (Bu), and beating (Be) in the open-loop model. The red contour and horizontal hatching indicate the range of values the variable g_{tonic} traverses as the parameter h is varied in the version of the closed-loop model with dynamic g_{tonic} and static h . For example, with h fixed at 0.6, the CPG is bursting and g_{tonic} oscillates between 0.21 and 0.32 nS. The red dashed horizontal lines demarcate regions of quiescence, slow beating, bursting, and fast beating in this model. The black curve is the bursting trajectory of the full closed-loop model (with dynamic g_{tonic} and dynamic h) projected onto the $g_{\text{tonic}} - h$ plane. Note that this limit cycle exists in the Q/Bu region indicating that the g_{tonic} values traversed during closed-loop bursting lie entirely within the range of g_{tonic} values that produce quiescence in the open-loop model. The black arrow indicates the direction of flow on the closed-loop limit cycle. The cyan, green, and magenta dots (along with the cyan, green, and magenta arrows labeled B, C, and D on the g_{tonic} axis) denote three locations on the closed-loop limit cycle that are further illustrated in Figs. 4B, C, and D (where the same color scheme is used). The blue arrow labeled A corresponds to $g_{\text{tonic}} = 0.3$ nS, which is the value used to further illustrate the open-loop limit cycle in Fig. 4A.

Figure 4. **Closed-loop fast subsystem undergoes bifurcations differently than the open-loop fast subsystem.** **A.** Bifurcation diagram of open-loop fast subsystem (\dot{V}, \dot{n}) with bifurcation parameter h , and $g_{\text{tonic}} = 0.3$ nS. Black curve \mathcal{S} shows stable (thick lines) and unstable (thin lines) fixed points of the fast subsystem. Solid black dots indicate saddle-node (SN), Hopf (HB), and homoclinic (HC) bifurcations of the fast subsystem. The blue trace is the bursting trajectory from the open-loop system projected onto the $h - V$ plane. Bottom panel is a zoomed-in view of the top panel, also showing the h -nullcline (dashed gray line). Open gray dot is an unstable fixed point of the full CPG subsystem $(\dot{V}, \dot{n}, \dot{h})$; the bursting trajectory circumnavigates this unstable fixed point. Additional unstable fixed points located at $(h = 0.20, V = -39)$ and $(h = 0.02, V = -24)$ are not shown. **B–D.** Bifurcation diagrams of closed-loop fast subsystem during silent phase (**B**), at the onset of spiking (**C**), and at the termination of spiking (**D**). Black trace is the closed-loop bursting trajectory, and gray curves show how \mathcal{S} shifts as g_{tonic} varies during closed-loop bursting (the locations shown correspond to the points labeled B, C, and D in Fig. 3). **B.** Cyan dot shows the location of the trajectory at the minimum g_{tonic} value (0.12 nS) observed during closed-loop bursting. Lower portion of \mathcal{S} , and corresponding SN point, are shifted to the right relative to the open-loop system and the CPG is not spiking. Cyan arrow indicates that \mathcal{S} will move to the left as the trajectory evolves and g_{tonic} increases through the remainder of the silent phase of the burst. **C.** Green dot shows the location of trajectory at the maximum g_{tonic} value (0.22 nS) observed during closed-loop bursting. Lower portion of \mathcal{S} , and SN point, are shifted to the left relative to panel (**B**) and the CPG is about to start spiking. Green arrow indicates that \mathcal{S} will move to the right as the trajectory evolves and g_{tonic} decreases, during the spiking phase of the burst. **D.** Magenta dot shows the location of the trajectory at $g_{\text{tonic}} = 0.22$, which is near the HC bifurcation that terminates spiking. Lower portion of \mathcal{S} is shifted to the left relative to (**B**) and to the right relative to (**C**). Magenta arrow indicates that \mathcal{S} will continue to move to the right until reaching the minimum g_{tonic} configuration shown in (**B**). **B–D bottom panels.** Solid gray dots are stable fixed points of the full CPG subsystem $(\dot{V}, \dot{n}, \dot{h})$. The trajectory does not circumnavigate these fixed points, but exhibits bursting due to the movement of \mathcal{S} , the fast subsystem’s steady-state curve.

Figure 5. **Chemosensory feedback (not the isolated CPG bursting mechanism) governs burst timing in the closed-loop system.** **A–C:** Effect of persistent sodium channel inactivation time constant ($\bar{\tau}_h$) and timescale of chemosensory feedback ($\tau_{P_aO_2}$) on burst properties. Blue lines (open-loop) and black lines (closed-loop): $\bar{\tau}_h$ is increased from 8 to 45 s, where $\gamma = 1$ corresponds to the default BRS model setting of $\bar{\tau}_h = 10,000$ ms. Green line: $\tau_{P_aO_2}$ is modulated by forcing the BRS model with compressed ($\gamma < 1$) and elongated ($\gamma > 1$) versions of the g_{tonic} waveform observed during closed-loop bursting ($\gamma = 1$). **A:** Interburst interval (IBI) increases linearly in the open-loop system as $\bar{\tau}_h$ is increased (blue) and in the forced system as $\tau_{P_aO_2}$ is increased (green). IBI is much less sensitive to $\bar{\tau}_h$ in the closed-loop system (black). **B–C:** Burst duration (**B**) and the number of spikes per burst (**C**) are more sensitive to increases in $\bar{\tau}_h$ in the open-loop system (blue) than in the closed-loop system (black). In the forced system, burst duration and the number of spikes per burst increase sharply, then level off, and eventually decrease slightly as $\tau_{P_aO_2}$ is increased (green).

Figure 6. **Coexistence of two stable periodic orbits (bistability) in the closed-loop respiratory control model.** **(A)** and **(B)** show simulations with identical parameter values but different initial conditions. Top panel is CPG voltage (mV), second panel is lung volume (liters), third panel is arterial oxygen (mmHg), bottom panel is chemosensory-dependent input to CPG (nS), and horizontal axis is time (seconds). **A:** “Eupneic” bursting. The central BRS circuit responds to time varying chemosensory input by producing a regular breathing rhythm at approximately 10 breaths per minute. Lung volume varies between 2-3 liters. Blood oxygen (P_aO_2) varies between 90 and 110 mmHg. **B:** Different initial conditions lead to pathological “tachypneic” spiking. The CPG receives elevated tonic input causing sustained spiking at several Hz, leading to ineffective motor output. Lung volume fluctuates by less than 0.1 liters and blood oxygen is approximately constant at a pathologically reduced level (25 mmHg).

Figure 7. **Reduced slow subsystem predicts that eupnea is lost at high metabolic demand through saddle-node bifurcation.** **A:** Phase line of averaged slow subsystem (23) showing the approximate rate of change of P_aO_2 (\bar{g}) as a function of P_aO_2 . The curves show when P_aO_2 will increase ($\bar{g} > 0$) and decrease ($\bar{g} < 0$) for three different values of the metabolic demand M . Colored dots are fixed points of the averaged slow subsystem ($\bar{g} = 0$). Zero crossings with positive and negative slopes are unstable and stable fixed points, respectively. When $M = 0.4 \times 10^{-5} \text{ ms}^{-1}$ (green curve), the system has a stable fixed point corresponding to eupneic bursting ($P_aO_2 = 89 \text{ mmHg}$), a stable fixed point corresponding to tachypneic spiking ($P_aO_2 = 41 \text{ mmHg}$), and an unstable fixed point ($P_aO_2 = 74 \text{ mmHg}$). When $M = 0.8 \times 10^{-5} \text{ ms}^{-1}$ (cyan curve), the system still has two stable fixed points, but the stable eupneic fixed point ($P_aO_2 = 87 \text{ mmHg}$) and the unstable fixed point ($P_aO_2 = 80 \text{ mmHg}$) have moved closer together. When $M = 1.6 \times 10^{-5} \text{ ms}^{-1}$ (magenta curve), the system has only one fixed point, which corresponds to stable tachypneic spiking ($P_aO_2 = 17 \text{ mmHg}$). **B:** Location of fixed points in averaged slow subsystem. The curve shows the P_aO_2 value of fixed points ($\bar{g} = 0$) as a function of metabolic demand M . For intermediate M values, the system has three branches of fixed points. The upper branch is stable and corresponds to eupnea, the middle branch is unstable, and the lower branch is stable and corresponds to tachypnea. At $M = 0.25 \times 10^{-5} \text{ ms}^{-1}$, the lower stable branch and unstable middle branch collide and these fixed points are destroyed in a saddle-node bifurcation (SN_1) leaving only the stable upper branch (eupnea) for $M < SN_1$. Similarly, at $M = 0.88 \times 10^{-5} \text{ ms}^{-1}$, the upper stable branch and unstable middle branch collide in another saddle-node bifurcation (SN_2) leaving only the stable lower branch (tachypnea) for $M > SN_2$.

Figure 8. **Sensory feedback increases the robustness of eupnea with respect to metabolic demand.** Mean P_aO_2 levels in systems with (closed-loop, black curve) and without (open-loop, blue curve) chemosensory feedback as a function of M . Green band indicates a nominal range of normoxia from 80-110 mmHg. The enhanced robustness of the closed-loop system is evident in the shallower slope of the black curve relative to the blue curve at the operating point of $P_aO_2 = 100 \text{ mmHg}$, and in the wider range of M values for which the black curve stays within the normoxic limits.

Figure 9. **Transient response of CPG in closed-loop system can lead to “autoresuscitation” after hypoxic perturbations.** The open-loop system was simulated with $g_{\text{tonic}} = 0.3800$ nS (red curve) and $g_{\text{tonic}} = 0.3791$ nS (blue curve) until it reached steady state. At $t = 0$, we “closed the loop” and allowed g_{tonic} to vary as a function of $P_{\text{a}}\text{O}_2$ throughout the remainder of the simulation. From these initial conditions, the blue trajectory approaches eupnea, whereas the red trajectory approaches tachypnea. The dashed line indicates that initial conditions determined from steady states of open-loop simulations with g_{tonic} values corresponding to $P_{\text{a}}\text{O}_2$ levels above (below) this line will approach eupnea (tachypnea). At $t = 180$ s, $P_{\text{a}}\text{O}_2$ was set to 40 mmHg momentarily and then immediately went back to being determined by the system dynamics. This hypoxic perturbation takes the trajectory to $P_{\text{a}}\text{O}_2$ levels below the steady-state dividing line, but the transient response allows the system to recover to eupnea. At $t = 360$ s, $P_{\text{a}}\text{O}_2$ was set to 30 mmHg momentarily, and then immediately went back to being determined by the system dynamics. The transient response again leads to an abrupt initial increase in $P_{\text{a}}\text{O}_2$ following the perturbation, but it is not enough to get over the dividing line and the trajectory ultimately approaches tachypnea.

Figure 10. **Hypoxia-induced barrage of spiking leads to an autoresuscitative lung expansion and is explained by the effect of hypoxia on the location of the homoclinic bifurcation that terminates spiking.** **A:** Traces from the closed-loop model during eupneic bursting ($t < 180$ s) and after a hypoxic perturbation ($t > 180$ s). At $t = 180$ s, P_aO_2 (top) was set to 40 mmHg, which causes a large and immediate increase in g_{tonic} (second from top). The increase in g_{tonic} elicits a barrage of spiking (V , second from bottom) that drives a much bigger increase in lung volume (vol_L , bottom) than occurs during a typical breath. This large breath causes a substantial increase in P_aO_2 , which reduces g_{tonic} sufficiently for the system to recover from the perturbation and return to eupneic bursting. The green and magenta dots indicate the values of system variables at, respectively, initiation and termination of spiking during the last burst before the perturbation and the first burst after the perturbation. The cyan dot indicates the minimum g_{tonic} point during eupneic closed-loop bursting. **B:** Expanded view of voltage trace from (A) during the last burst before the hypoxic perturbation (top) and during the barrage of spiking induced by the perturbation (bottom). The burst induced by the perturbation is longer and consists of higher frequency spiking than the burst before the perturbation. **C:** Bifurcation diagram of BRS model fast subsystem during the last burst before the hypoxic perturbation (top) and during the barrage of spiking induced by the perturbation (bottom). Top: Black trace is the trajectory during closed-loop bursting, projected onto the $V - h$ plane. The green, magenta, and cyan curves show the location of the fast subsystem steady states in its leftmost position which occurs at the initiation of spiking (green, $g_{\text{tonic}} = 0.22$ nS), at the homoclinic bifurcation that terminates spiking (magenta, $g_{\text{tonic}} = 0.18$ nS), and at its rightmost position which occurs at the g_{tonic} minimum point (cyan, $g_{\text{tonic}} = 0.12$ nS). Note that these three curves are the same as those shown in Fig. 4B, C, and D. Bottom: Black trace is the trajectory during the barrage of spiking induced by the perturbation, projected onto the $V - h$ plane. The green and magenta curves show the location of the fast subsystem steady states in its leftmost position which occurs at the initiation of spiking (green, $g_{\text{tonic}} = 0.57$ nS), and at the homoclinic bifurcation that terminates spiking (magenta, $g_{\text{tonic}} = 0.35$ nS). The cyan curve is the same as in the top panel. The drastic reduction in P_aO_2 due to the hypoxic perturbation has shifted the green curve much further to the left (cf. top and bottom panels), enabling the CPG to fire more spikes (and at a higher frequency) before reaching the homoclinic bifurcation.

Figure 11. **Hypoxia induces a barrage of spiking *in vitro*.** **A:** Application of 300 μM sodium cyanide (NaCN), a pharmacological analog of hypoxia, led to increased spiking in an individual pBC inspiratory cell recorded in current-clamp (top) and increased network activity measured as hypoglossal nerve (XII) rootlet discharge (bottom) in a brainstem slice preparation. At the peak of the stimulation, phasic, coordinated drive is abolished. Insets show the firing pattern of pBC cell before (left) and after (right) the NaCN challenge. The depolarization and increased spiking that occurs in response to the hypoxic perturbation *in vitro* is qualitatively similar to the responses observed in our closed-loop model. **B:** Summary data from nine experiments showing burst duration and frequency changes for baseline, NaCN treatment, hypoxia treatment, and recovery ($N = 9$, $p < 0.05$ ANOVA, Tukey's LSD as *post-hoc* test, baseline vs. hypoxia or NaCN, error bars are SEM). NaCN and hypoxia challenges do not result in statistically significantly different responses and produce an equivalent perturbation of the breathing rhythm in our *in vitro* slice preparations.

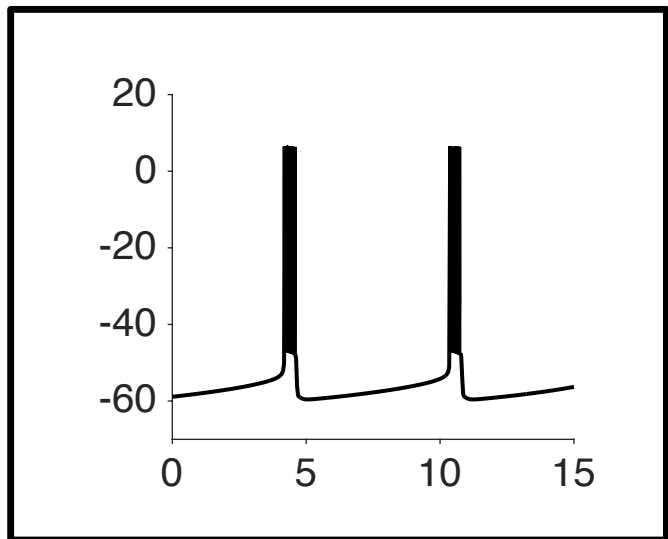
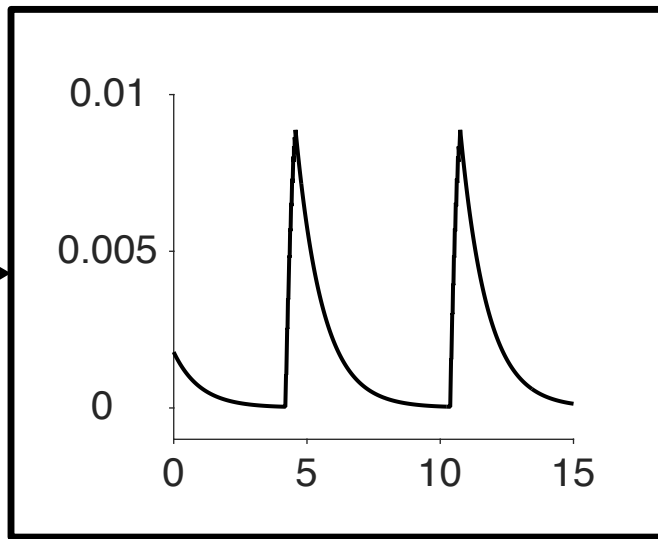
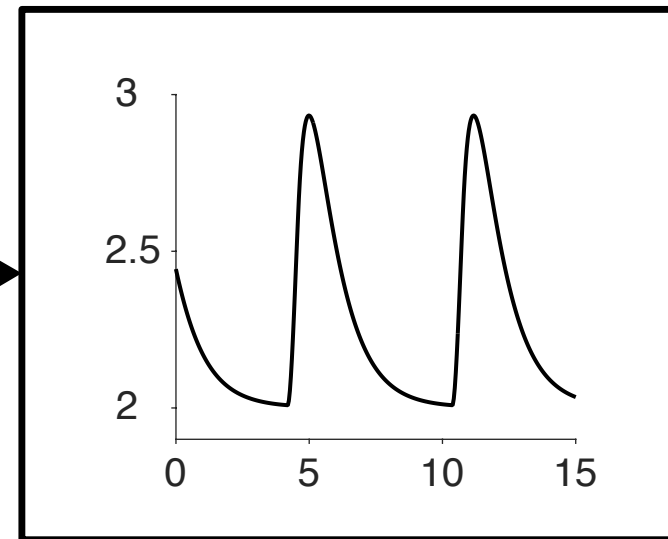
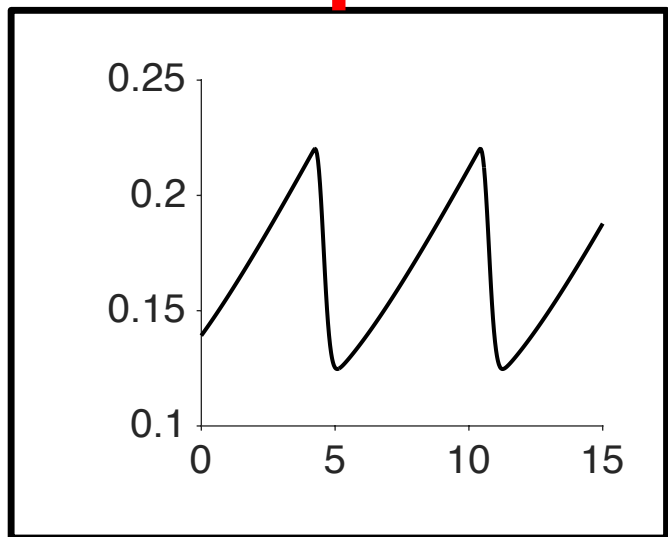
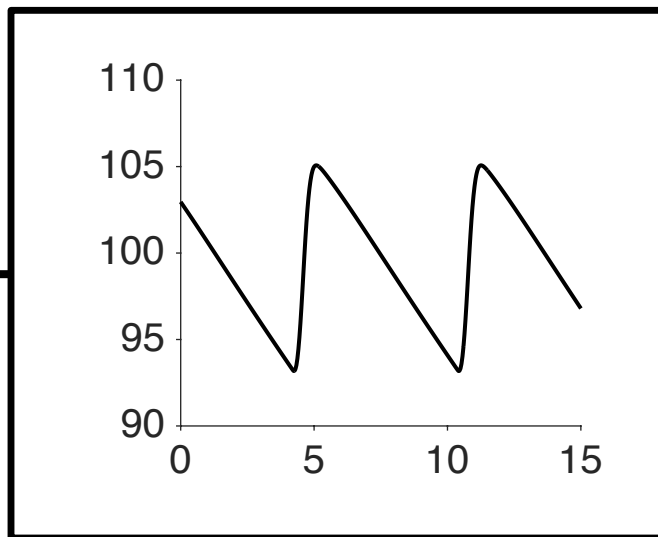
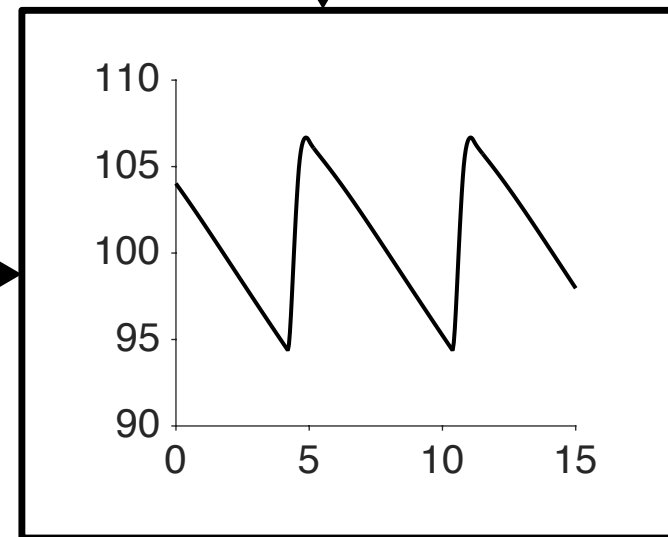
Figure 12. **Recovery to eupnea versus tachypneic failure following transient interruption of chemosensory feedback.** **A:** Time course of P_aO_2 before (black), during (blue), and after (green) interruption of chemosensory feedback. Black: Eupneic breathing in closed-loop model. Blue: Chemosensory feedback is interrupted by holding g_{tonic} fixed at 0.1 nS for 49.2466 s. Green: Chemosensory feedback is reestablished by again making g_{tonic} a function of P_aO_2 . System recovers to eupnea. **B:** Same as (A), except the $g_{\text{tonic}} = 0.1$ nS clamp (blue) is held for 0.1 ms longer. After reestablishing chemosensory feedback the system ultimately descends into tachypnea (red) rather than recovering to eupnea. **C.** Eupneic recovery from (A) projected onto $(h, \text{vol}_L, P_aO_2)$ coordinates. During the g_{tonic} clamp (blue curve), the CPG is quiescent and P_aO_2 decreases to 42 mmHg. Following release of the clamp (green curve), g_{tonic} increases rapidly, causing a barrage of spiking and a large expansion of lung volume that rapidly increases P_aO_2 to 82 mmHg. From $t = 120$ to 180 seconds the system exhibits bursts of spiking with shorter interburst intervals and shorter burst durations than eupneic breathing. This leads to intermediate P_aO_2 values (76 to 80 mmHg) as the interburst intervals and burst durations gradually lengthen and the system returns to eupneic breathing. **D:** Tachypneic failure from (B) projected onto $(h, \text{vol}_L, P_aO_2)$ coordinates. Same as (C), except that during the intermediate P_aO_2 oscillations from $t = 120$ to 180 seconds the interburst intervals and burst durations gradually shorten and the system descends into tachypnea (red curve).

Figure 13. **Floquet eigenvectors at the eupnea-tachypnea boundary limit cycle.** **A:** Trajectories from the closed-loop model that either recover to eupnea (green) or descend to tachypnea (red) following chemosensory interruption, projected onto $(h, \text{vol}_L, P_aO_2)$ coordinates. These are the same trajectories as shown in Fig. 12C and D, replotted here for the time window between $t = 130$ and 155 seconds, when they are near an unstable limit cycle on the boundary between eupnea and tachypnea. The black arrows illustrate the eigenvectors associated with the unstable Floquet multiplier at four locations along the boundary limit cycle. To aid the clarity of the illustration, the eigenvectors were multiplied by -1 so that the arrows point towards tachypnea rather than eupnea. **B–E:** Eigenvector components at the locations labeled (b)–(e) in panel (A). The signs of the components were chosen such that positive values are consistently “pro-eupneic” and negative values are consistently “pro-tachypneic” (see text for details).

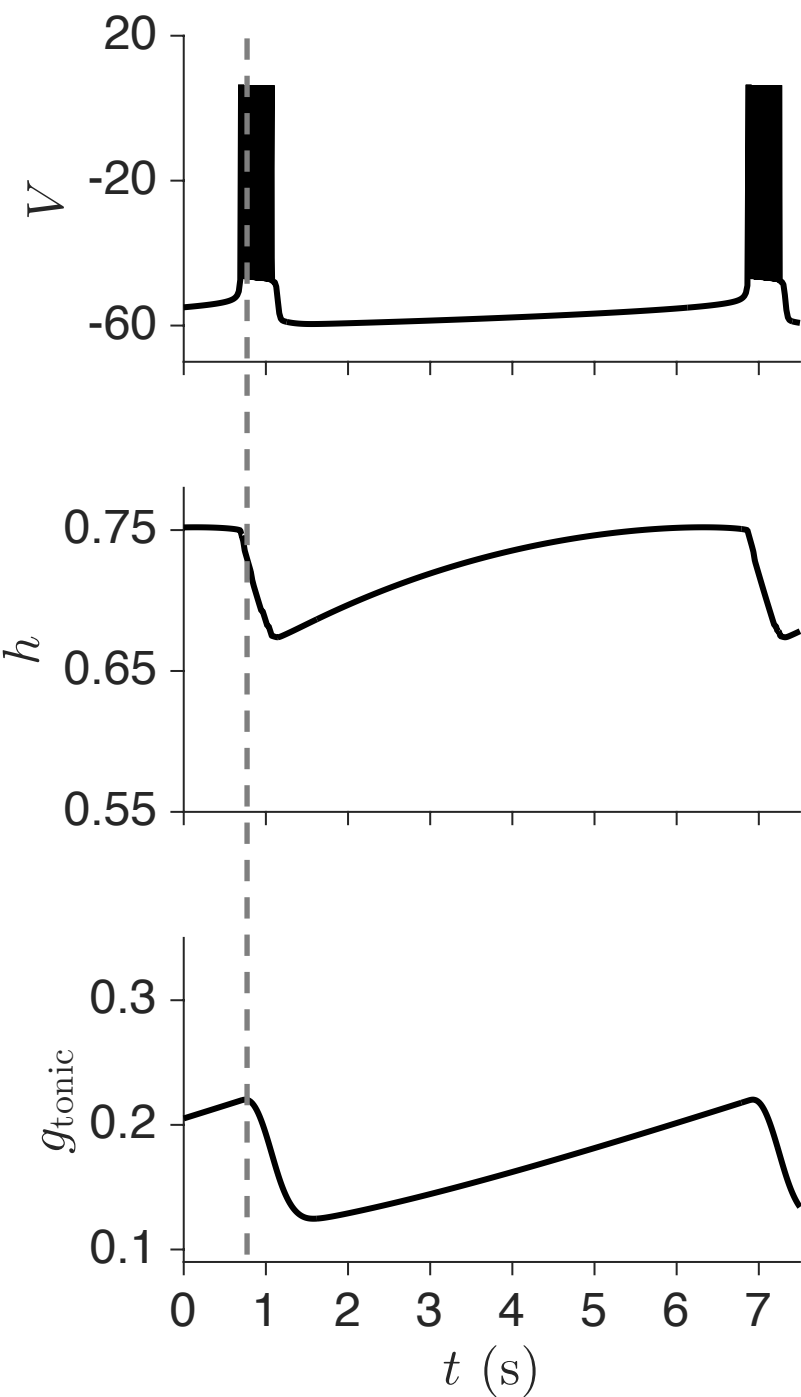
Figure 14. **Autoresuscitation occurs for both high and low default g_{tonic} levels.** Pseudocolors indicate $P_{\text{a}}\text{O}_2$ levels in the restored closed-loop system after transient interruption of chemosensory feedback for a range of durations (horizontal axis, seconds) and severities (vertical axis, nS). The severity of the failure corresponds to the value at which g_{tonic} was held constant during the chemosensory interruption. The $P_{\text{a}}\text{O}_2$ levels shown were measured 3 minutes after chemosensory feedback was reestablished and were calculated as the mid-range of $P_{\text{a}}\text{O}_2$ over a 10 second window. The capability of the system to autoresuscitate is observed whether the CPG is quiescent due to low input drive (low g_{tonic} values) or hyperexcited due to high input drive (high g_{tonic} values) during the absence of chemosensory feedback. For default g_{tonic} values in an intermediate range, the system recovers to eupnea despite arbitrarily long interruptions of feedback.

Figure 15. **Recovery to eupnea versus tachypneic failure following transient interruptions of chemosensory feedback assuming high input drive to the CPG during the interruptions.** These simulations are analogous to those shown in Fig. 12, except here g_{tonic} is set to 0.5 nS (high drive to CPG) rather than 0.1 nS (low drive to CPG) in the absence of chemosensory feedback. **A:** Time course of $P_a\text{O}_2$ before (black), during (blue), and after (green) interruption of chemosensory feedback. Black: Eupneic breathing in closed-loop model. Blue: Chemosensory feedback is interrupted by holding g_{tonic} fixed at 0.5 nS for 24.5 s. Green: Chemosensory feedback is reestablished by again making g_{tonic} a function of $P_a\text{O}_2$. System recovers to eupnea. **B:** Same as in (A), except the $g_{\text{tonic}} = 0.5$ nS clamp (blue) is held for 0.1 s longer. After reestablishing chemosensory feedback the system ultimately descends into tachypnea (red) rather than recovering to eupnea. **C.** Eupneic recovery from (A) projected onto $(h, \text{vol}_L, P_a\text{O}_2)$ coordinates. The interruption of chemosensory feedback causes a sudden increase in g_{tonic} , since the constant value it is set to during the interruption (0.5 nS) is higher than the values traversed by g_{tonic} during eupneic bursting (0.12-0.22 nS). This change triggers a barrage of spiking and a large expansion of lung volume that rapidly increases $P_a\text{O}_2$ to 124 mmHg. During the remainder of the g_{tonic} clamp, the CPG exhibits tonic spiking that does not drive effective lung expansions and $P_a\text{O}_2$ decreases to 83 mmHg. Following release of the clamp, the system exhibits bursts of spiking with shorter interburst intervals and shorter burst durations than eupneic breathing. This leads to intermediate $P_a\text{O}_2$ values (76 to 80 mmHg) as the interburst intervals and burst durations gradually lengthen and the system returns to eupneic breathing (green trace). **D:** Tachypneic failure from (B) projected onto $(h, \text{vol}_L, P_a\text{O}_2)$ coordinates. Same as in (C), except that during the intermediate $P_a\text{O}_2$ oscillations from $t = 90$ to 120 seconds the interburst intervals and burst durations gradually shorten and the system descends into tachypnea (red trace).

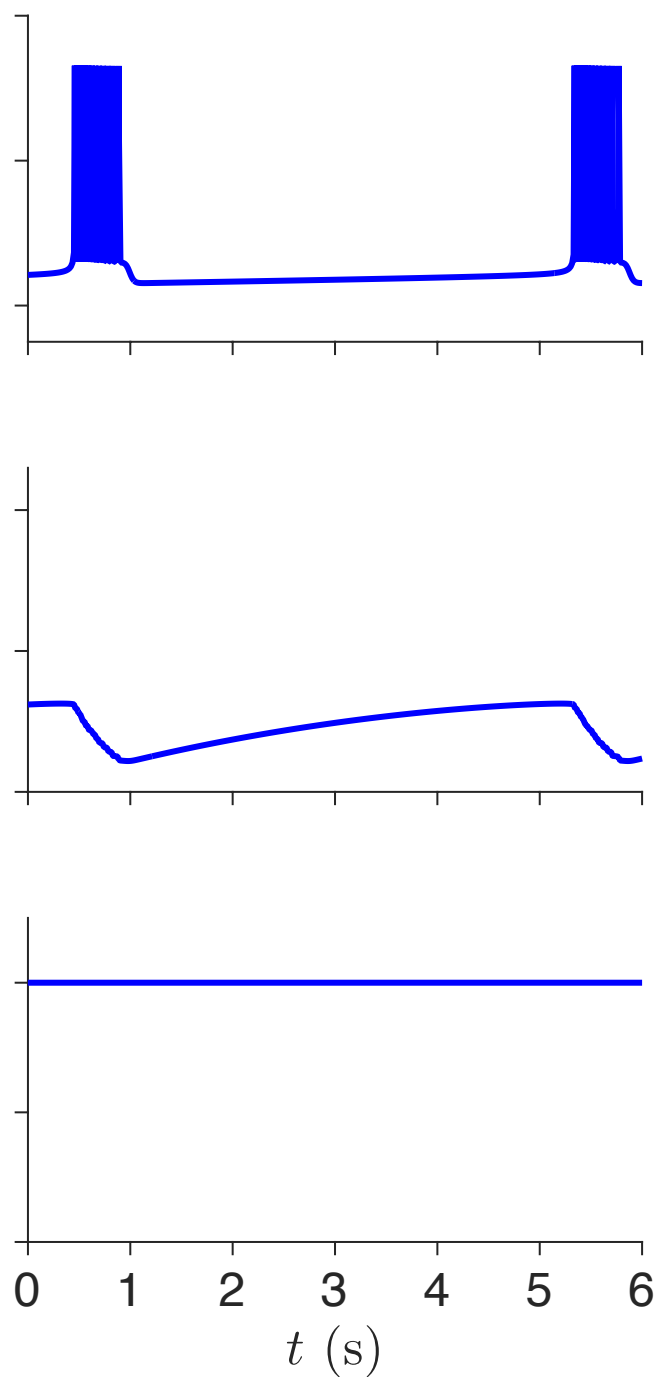
Figure 16. (Appendix Figure 1) **Phase plots showing the relative speed of each variable during closed-loop bursting identify $P_a\text{O}_2$ as a slow variable.** Horizontal axis is x and vertical axis is the rate of change $x'(t)$ normalized by the range of x , where $x = n, V, \alpha, h, \text{vol}_L, P_A\text{O}_2, P_a\text{O}_2$. Green dots indicate the maximal speed ν_x of each variable ($-\nu_x$ is shown for $x = h$). Note the significantly different time scales involved: $P_a\text{O}_2, P_A\text{O}_2,$ and vol_L are slower than h and α , which themselves are slower than V and n .

CPG (V, h, n)**Motor pool (α)****Lung Volume (vol_L)** I_{tonic} **Chemosenstion (g_{tonic})****Blood Oxygen (P_aO_2)****Lung Oxygen (P_AO_2)** V 

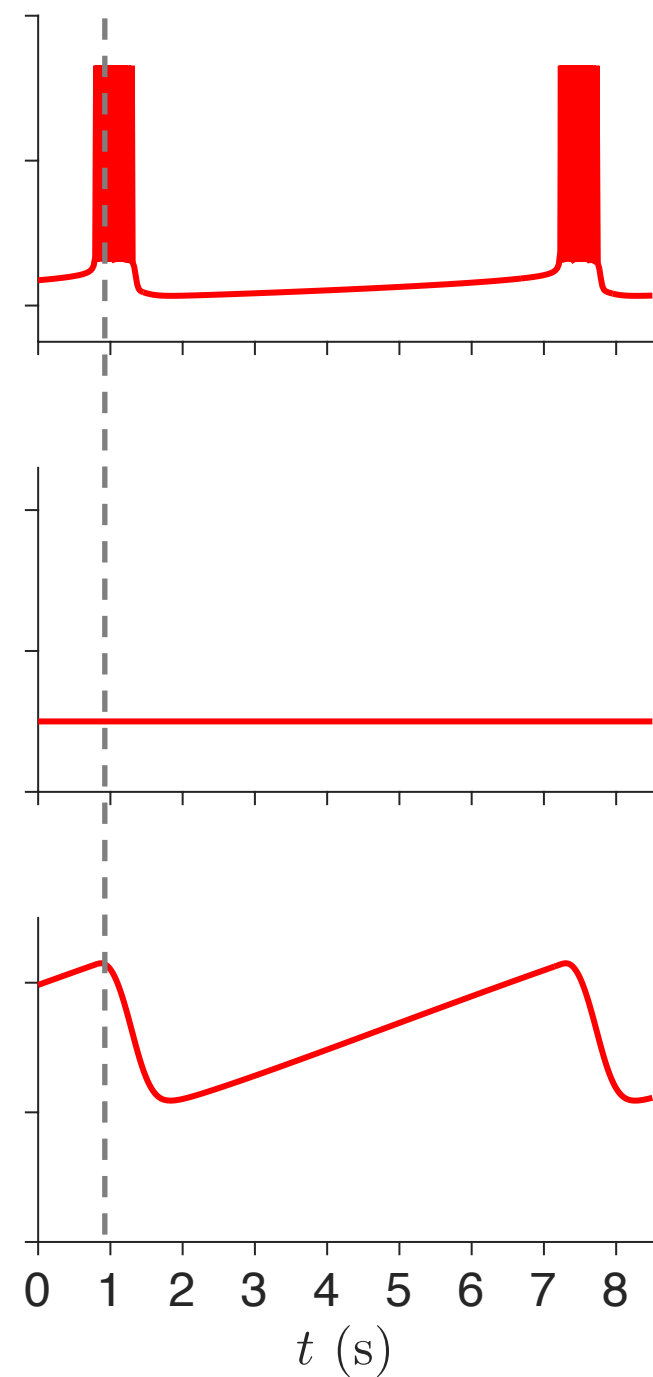
A Closed loop
(dynamic g_{tonic} + dynamic h)



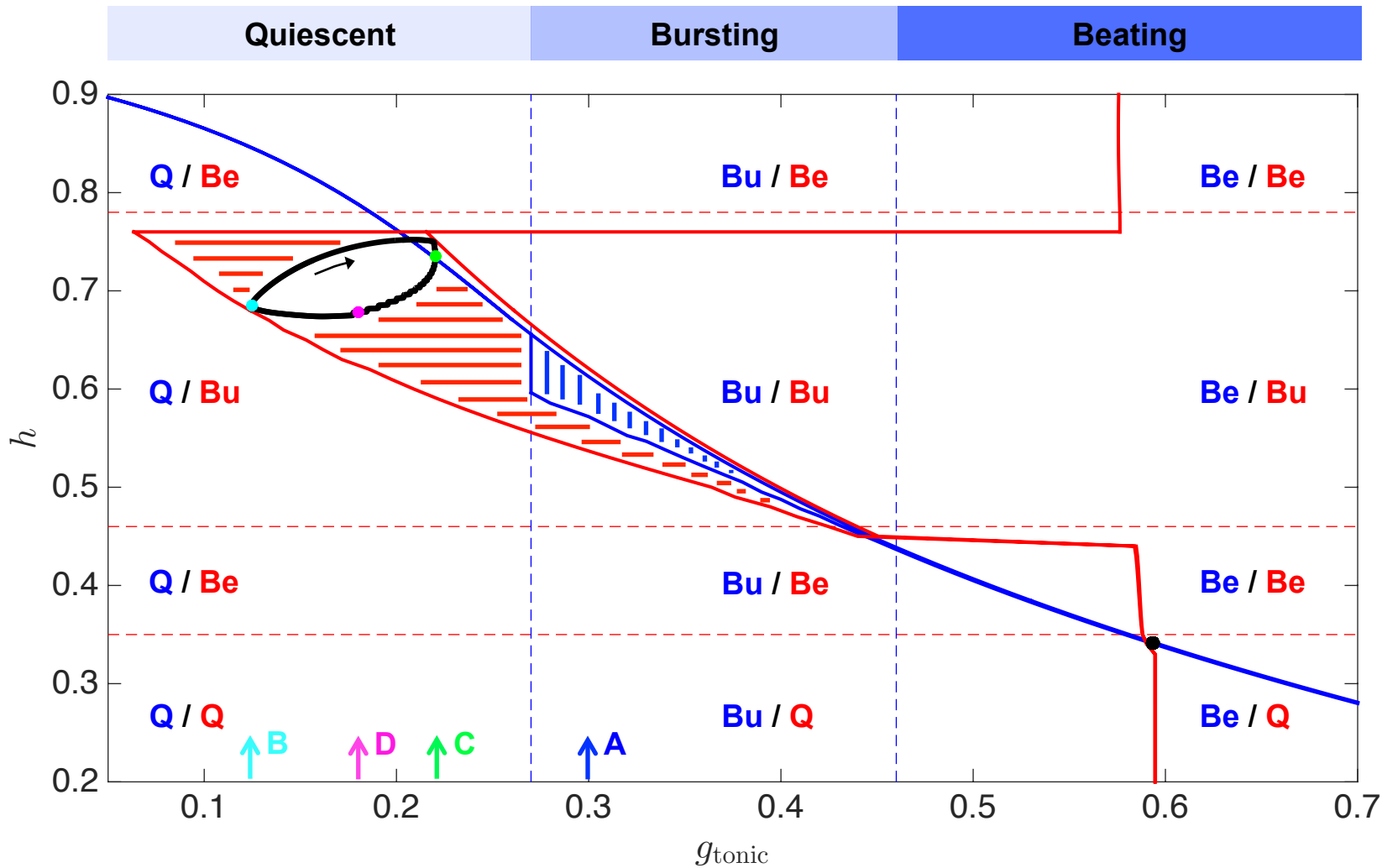
B Open loop
(static g_{tonic} + dynamic h)



C Closed loop
(dynamic g_{tonic} + static h)



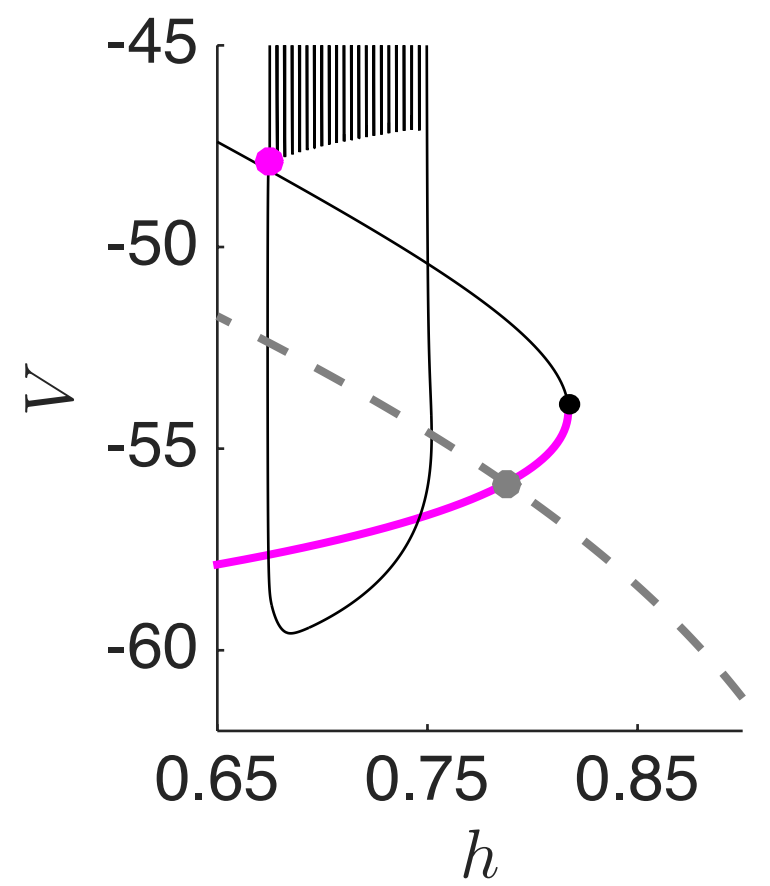
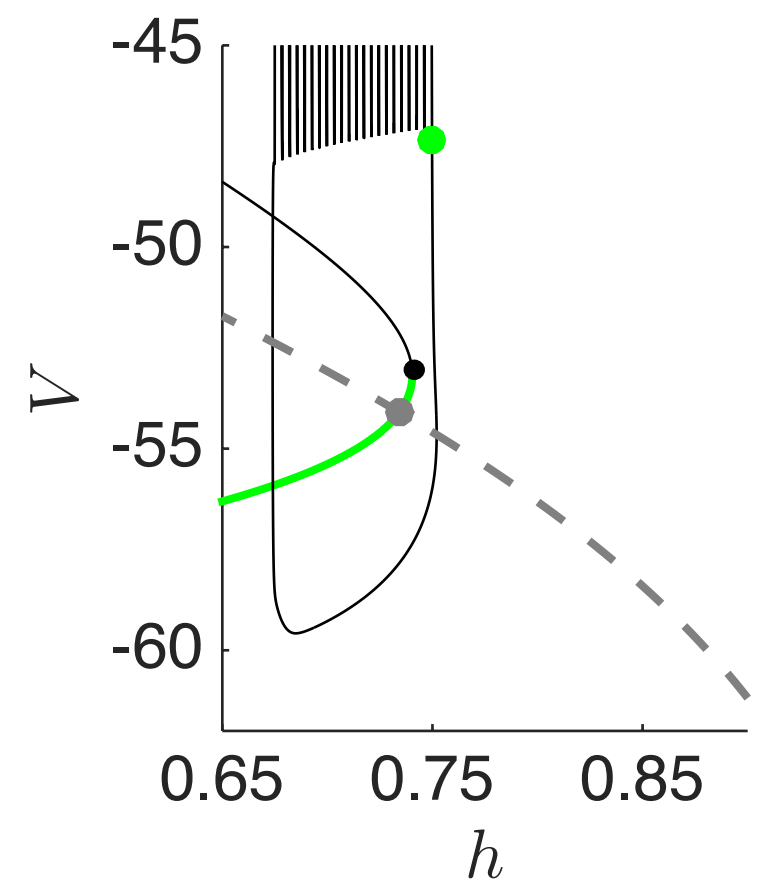
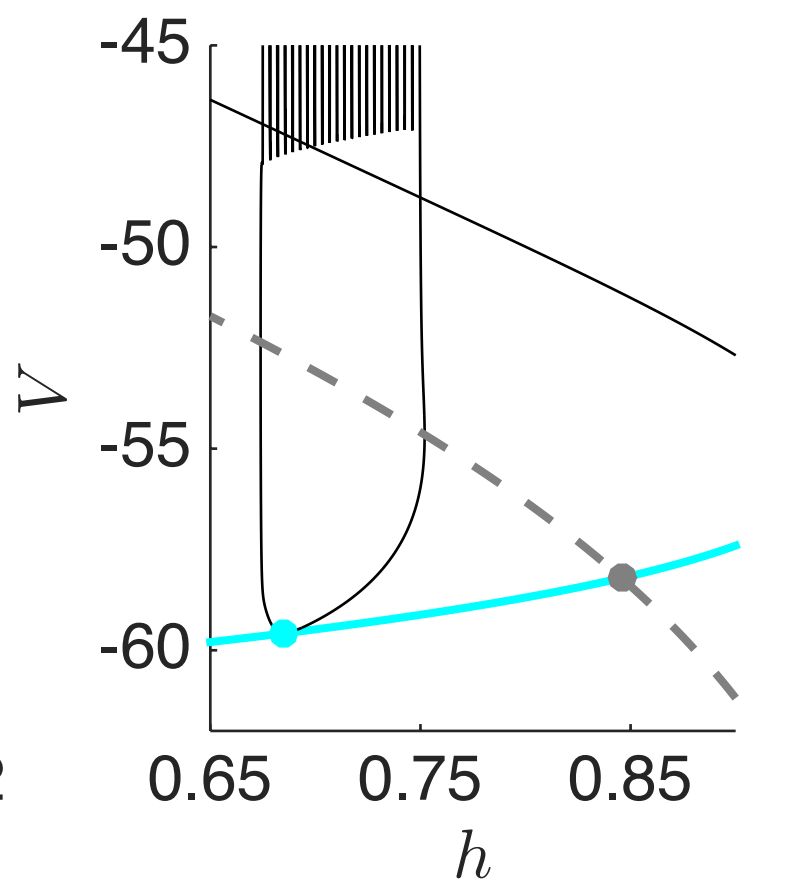
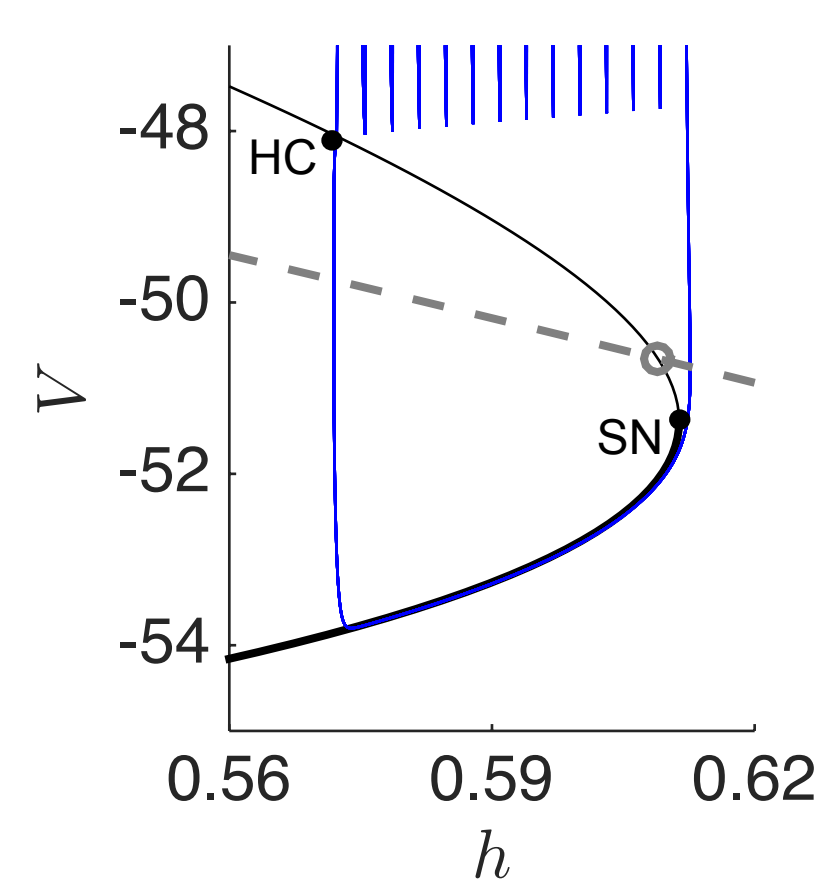
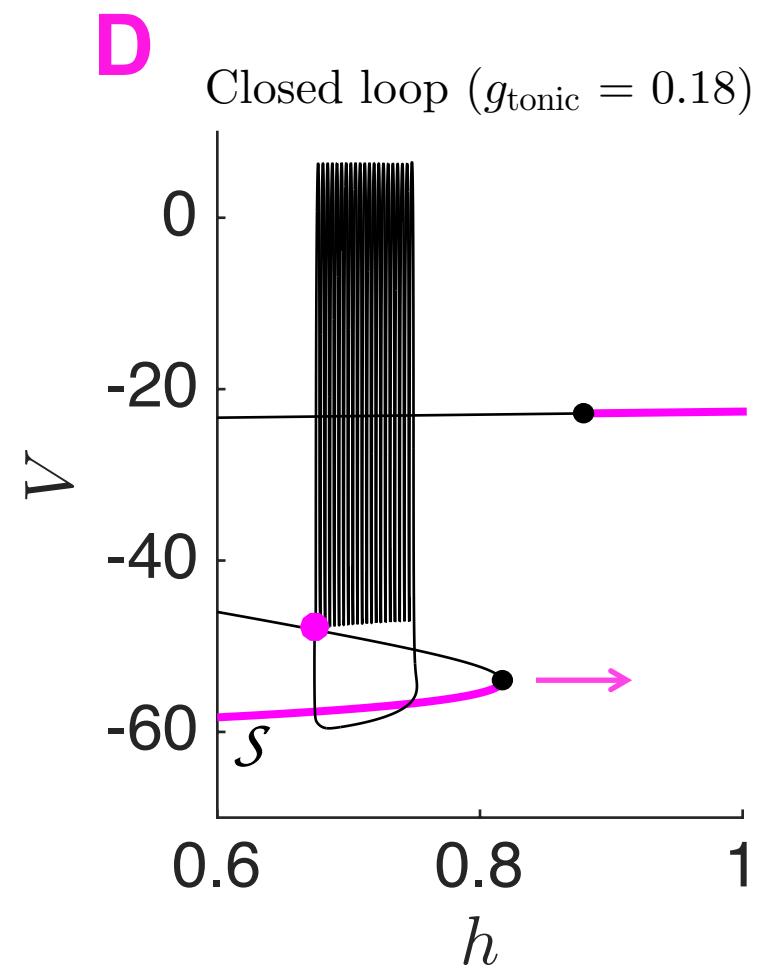
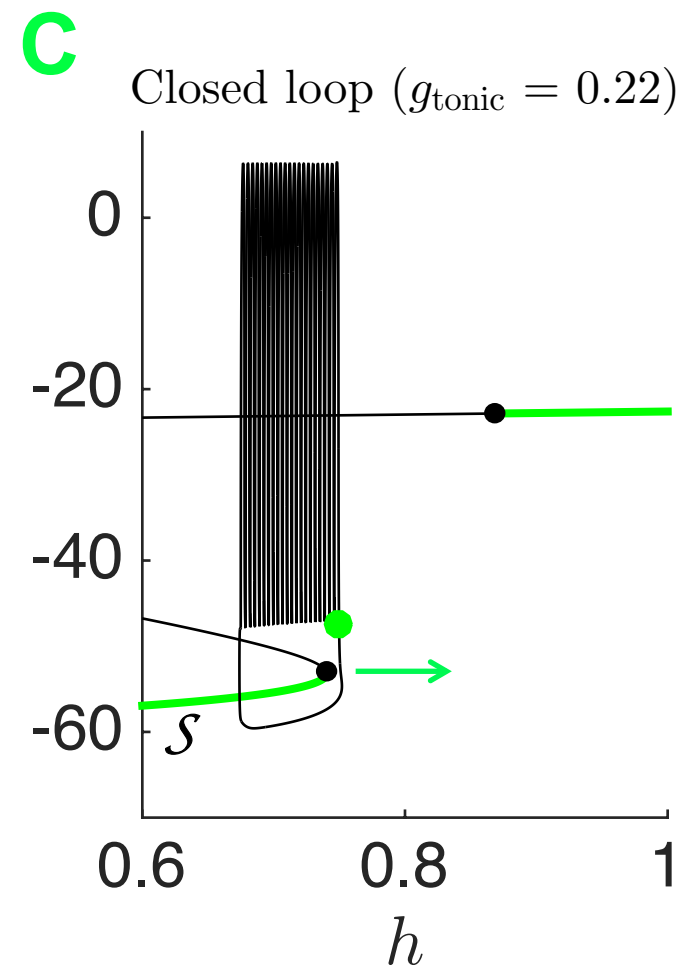
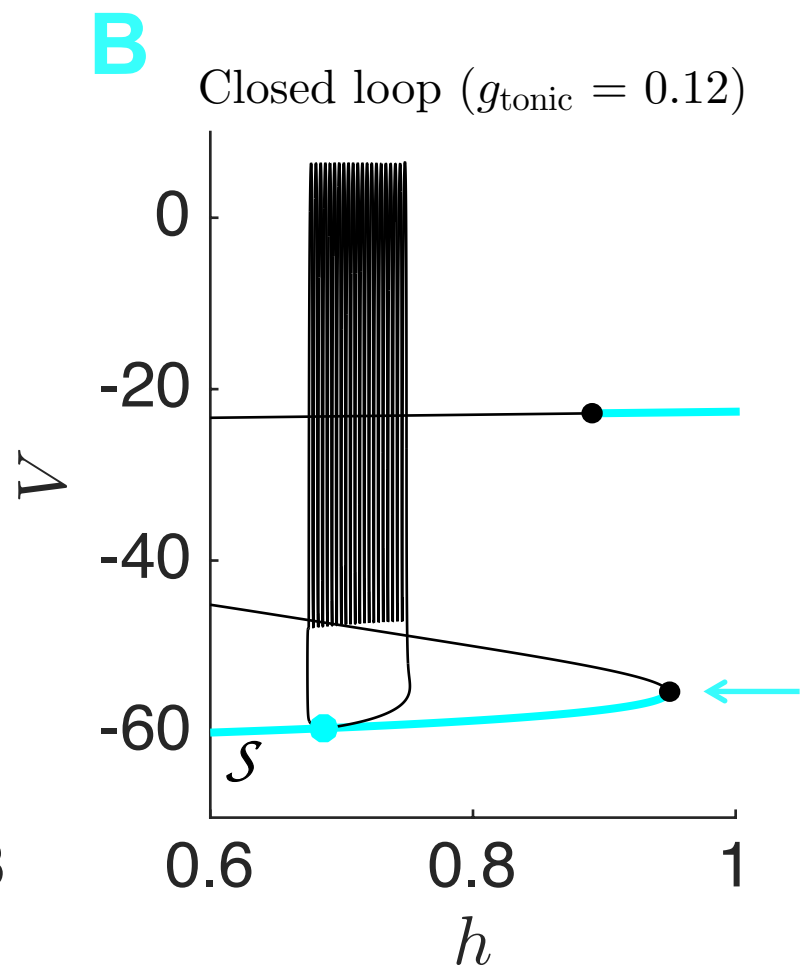
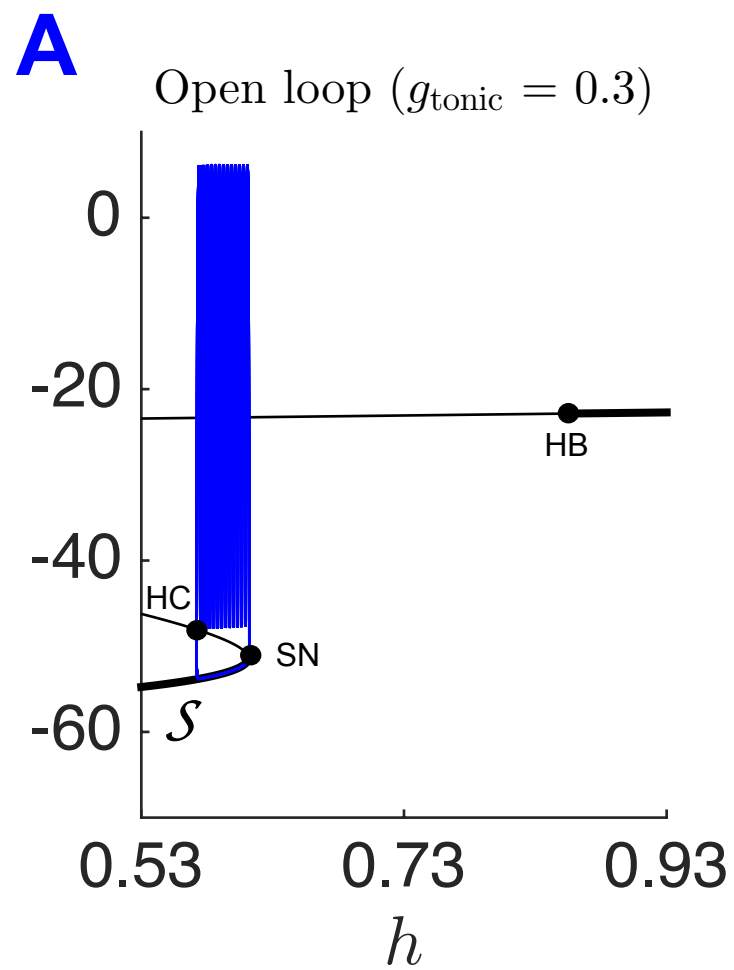
Open loop (static g_{tonic} + dynamic h)

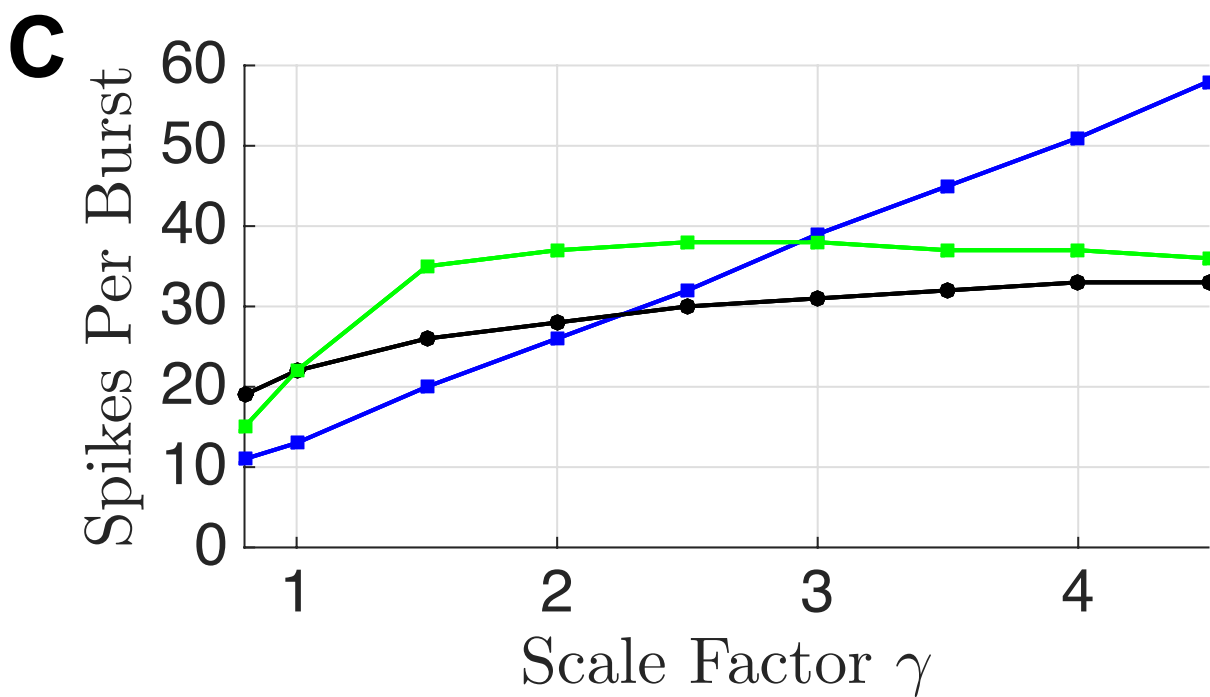
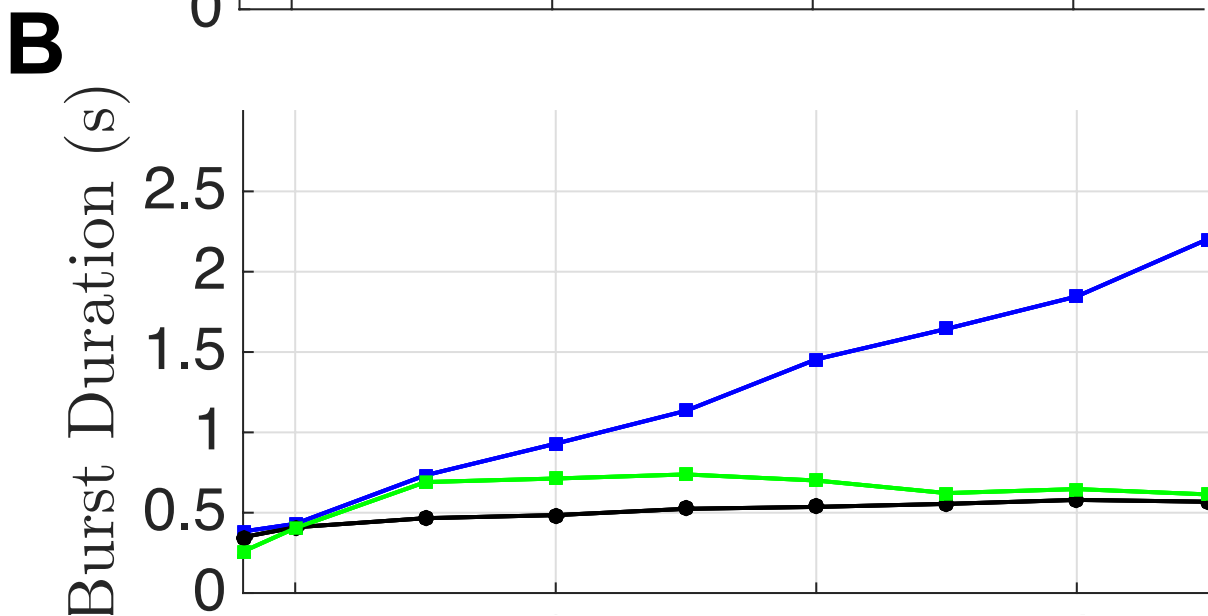
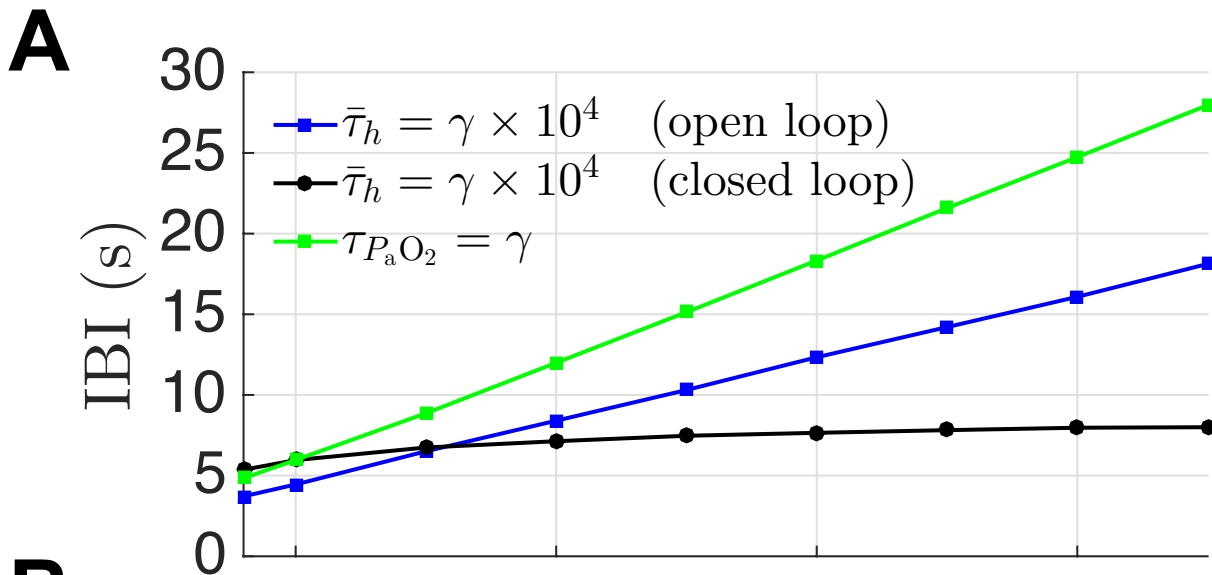


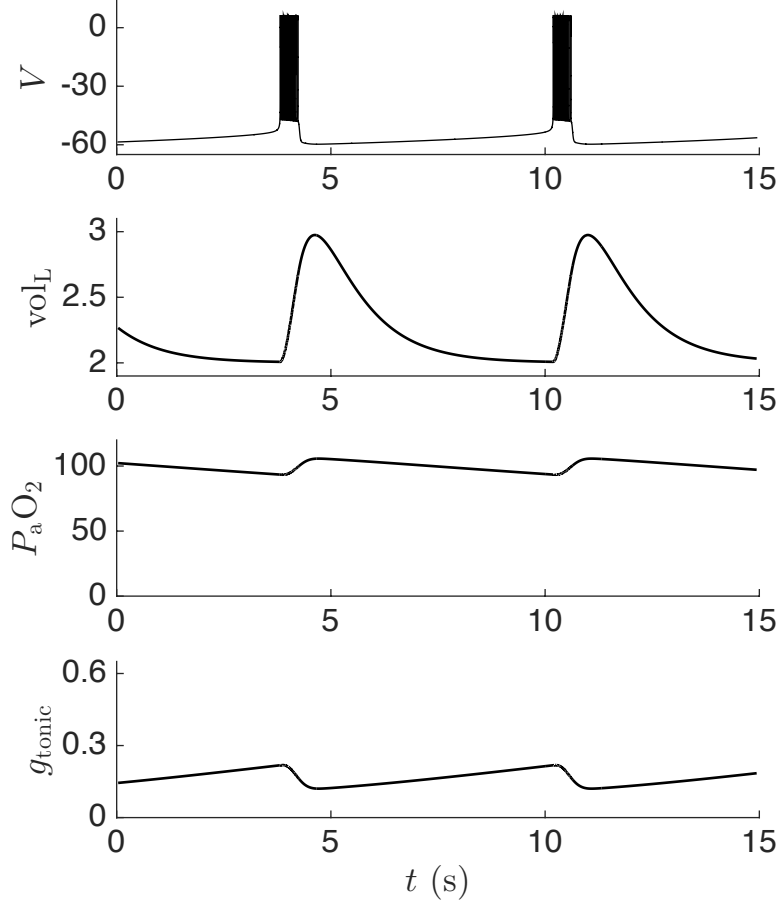
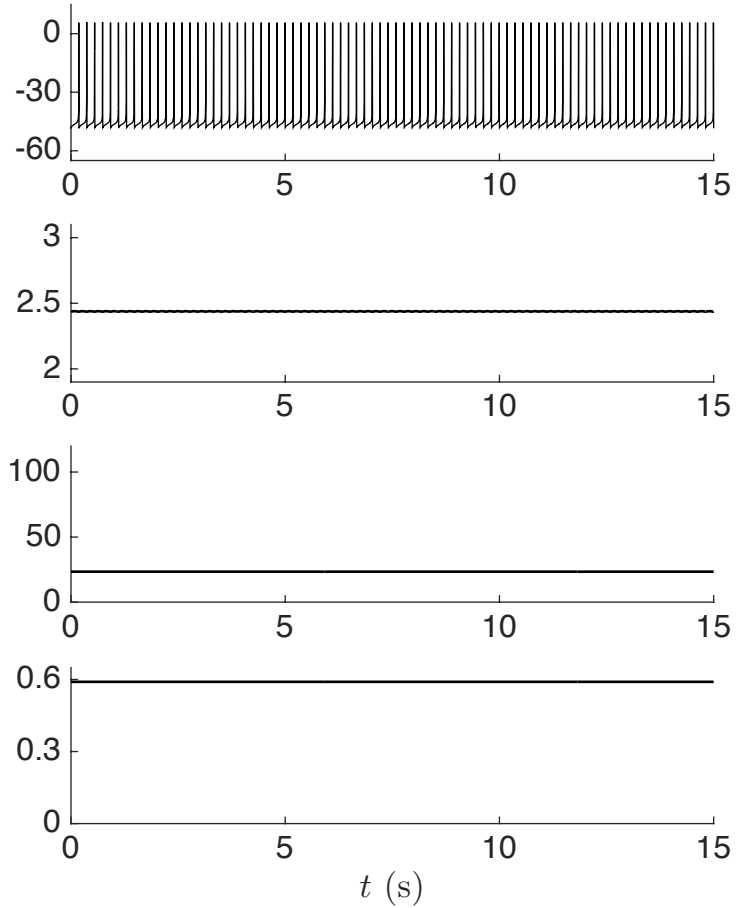
Fast Beat.
Bursting
Slow Beat.
Quiesc.

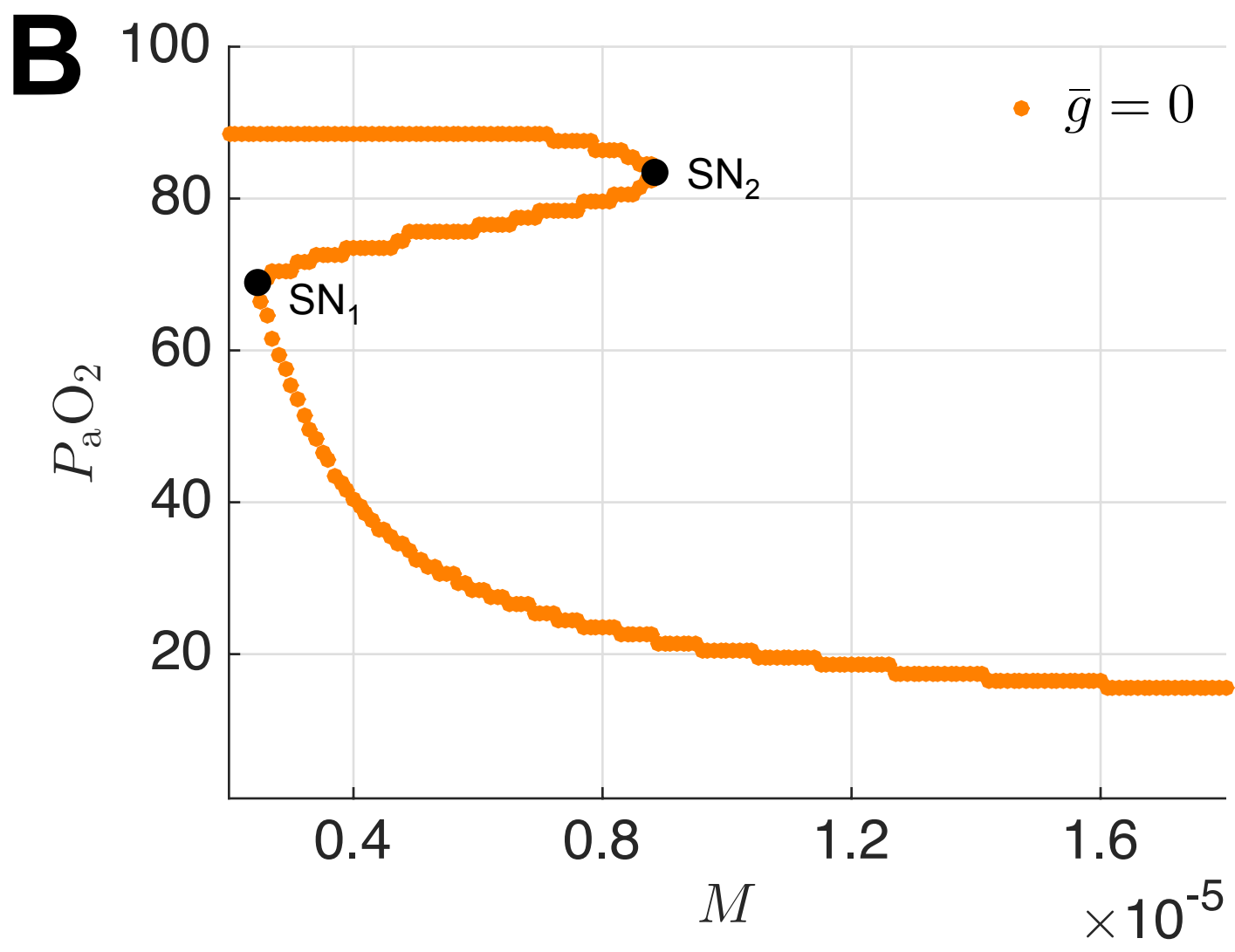
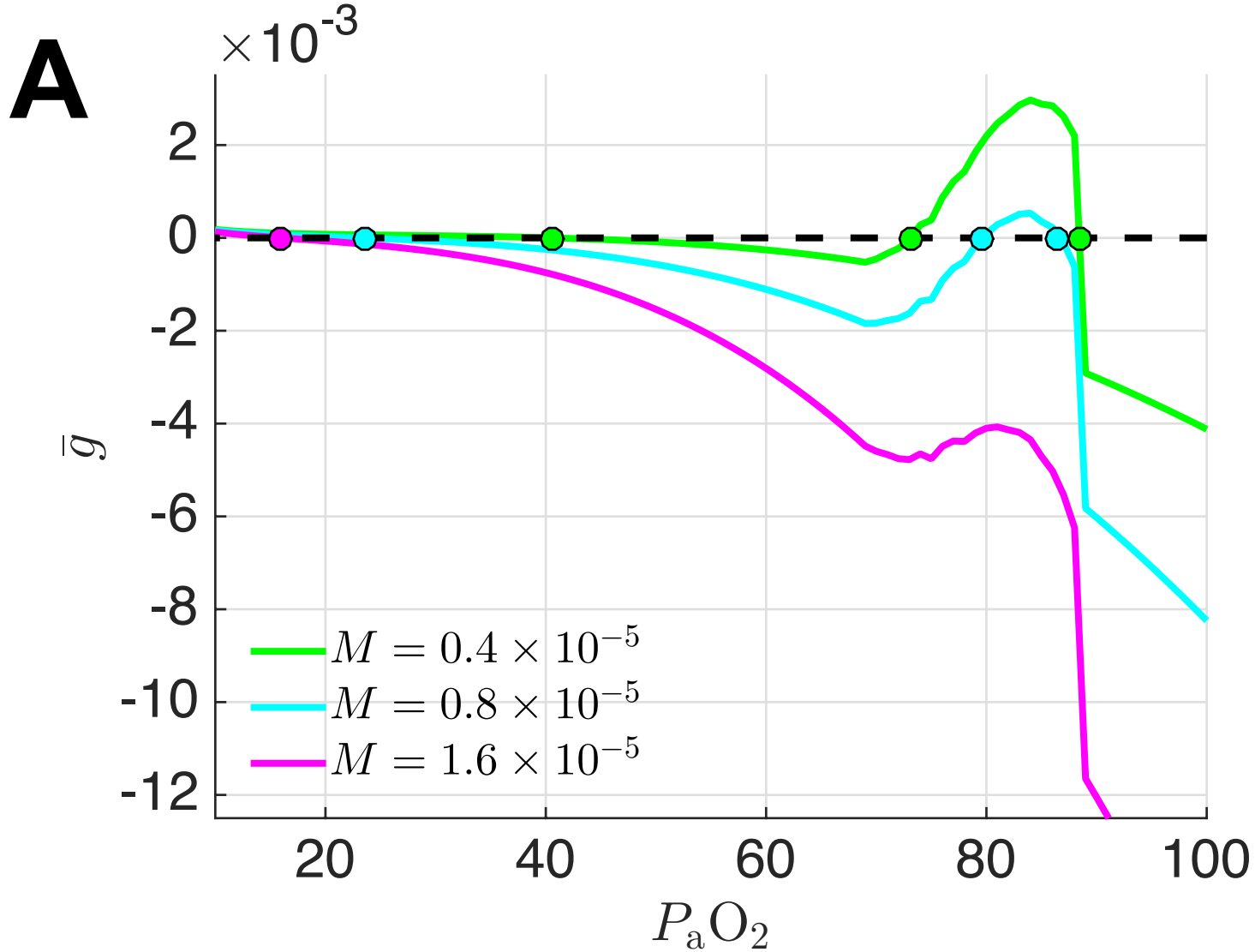
(dynamic g_{tonic} + static h)

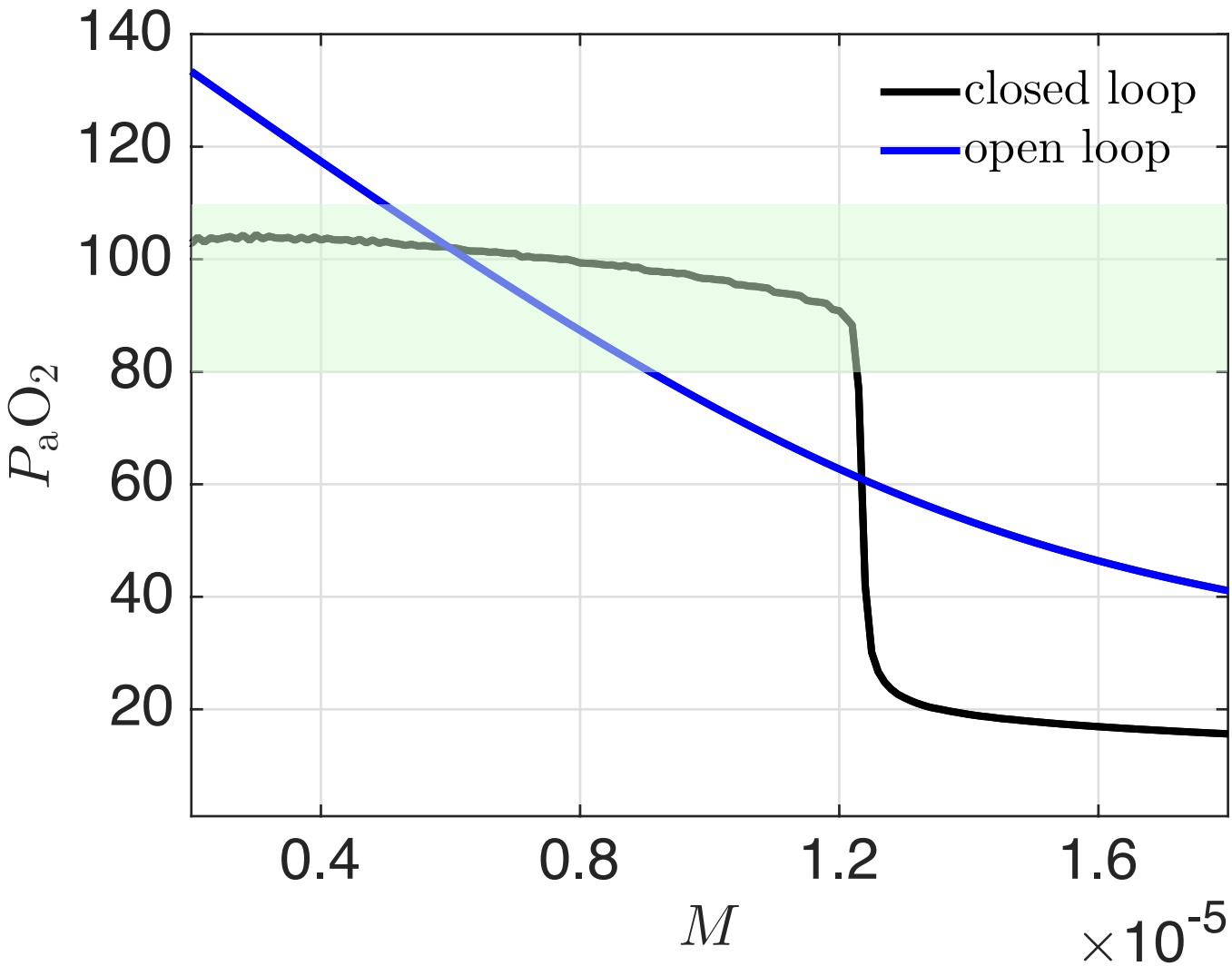
Closed loop

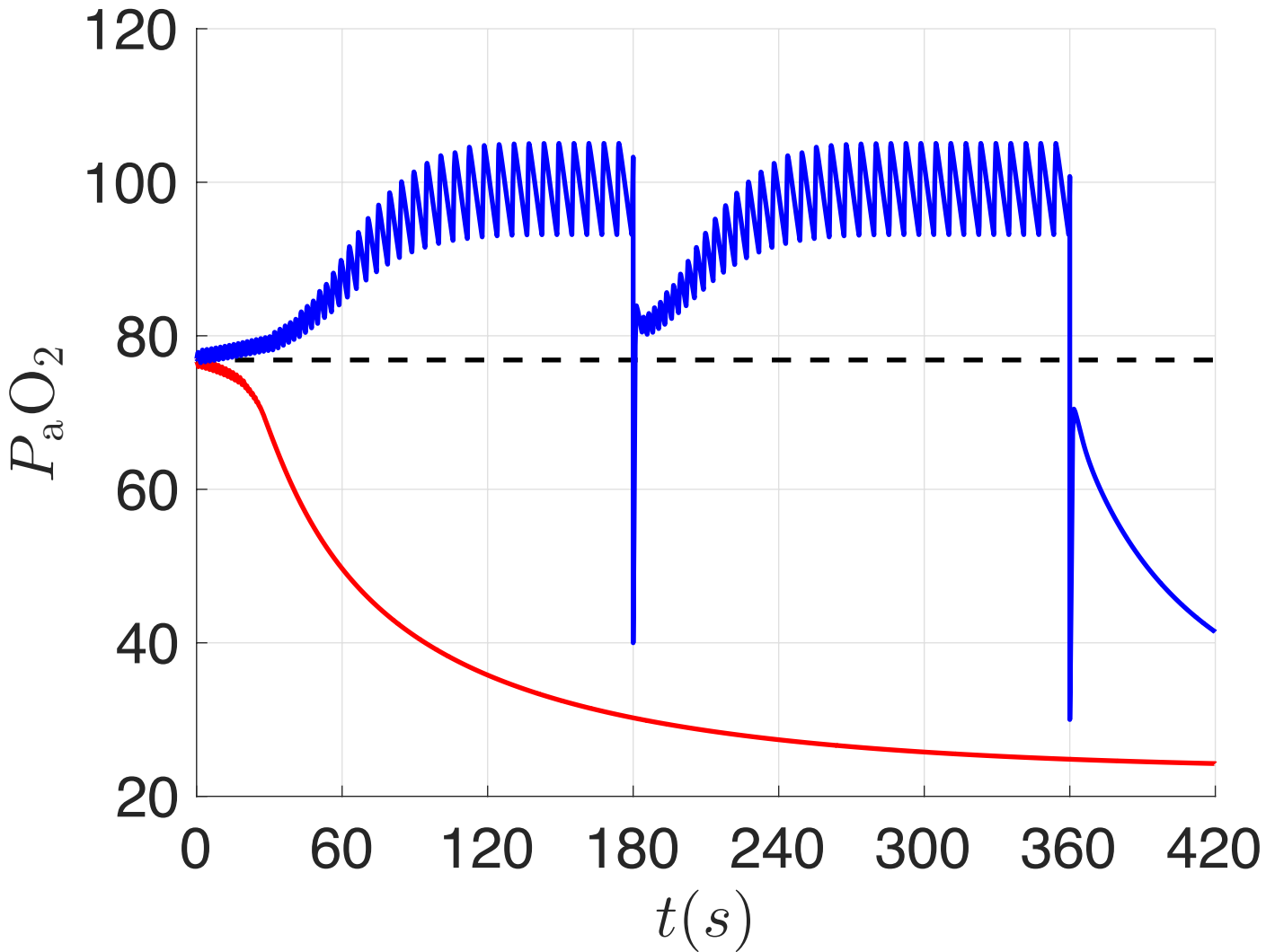


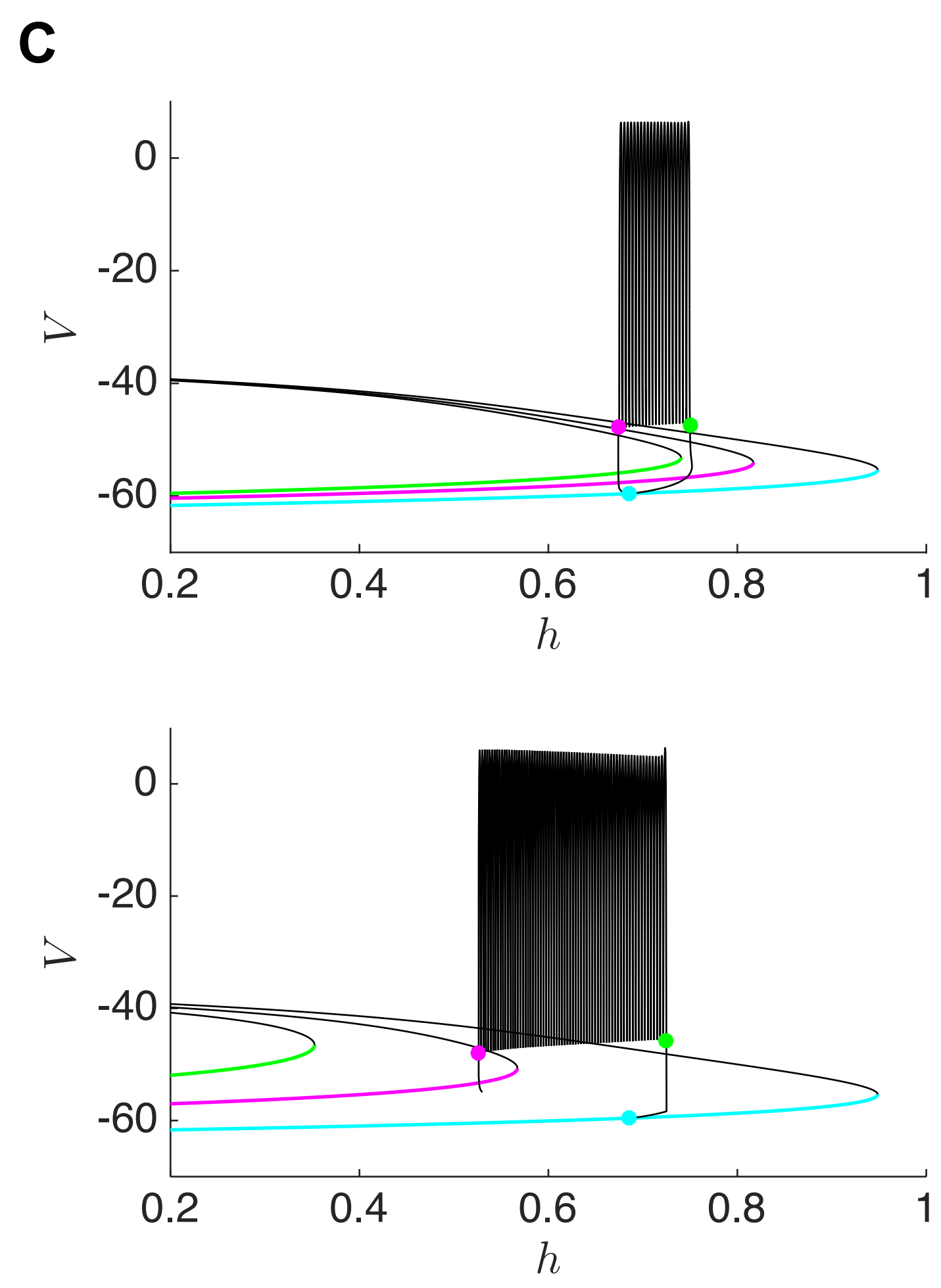
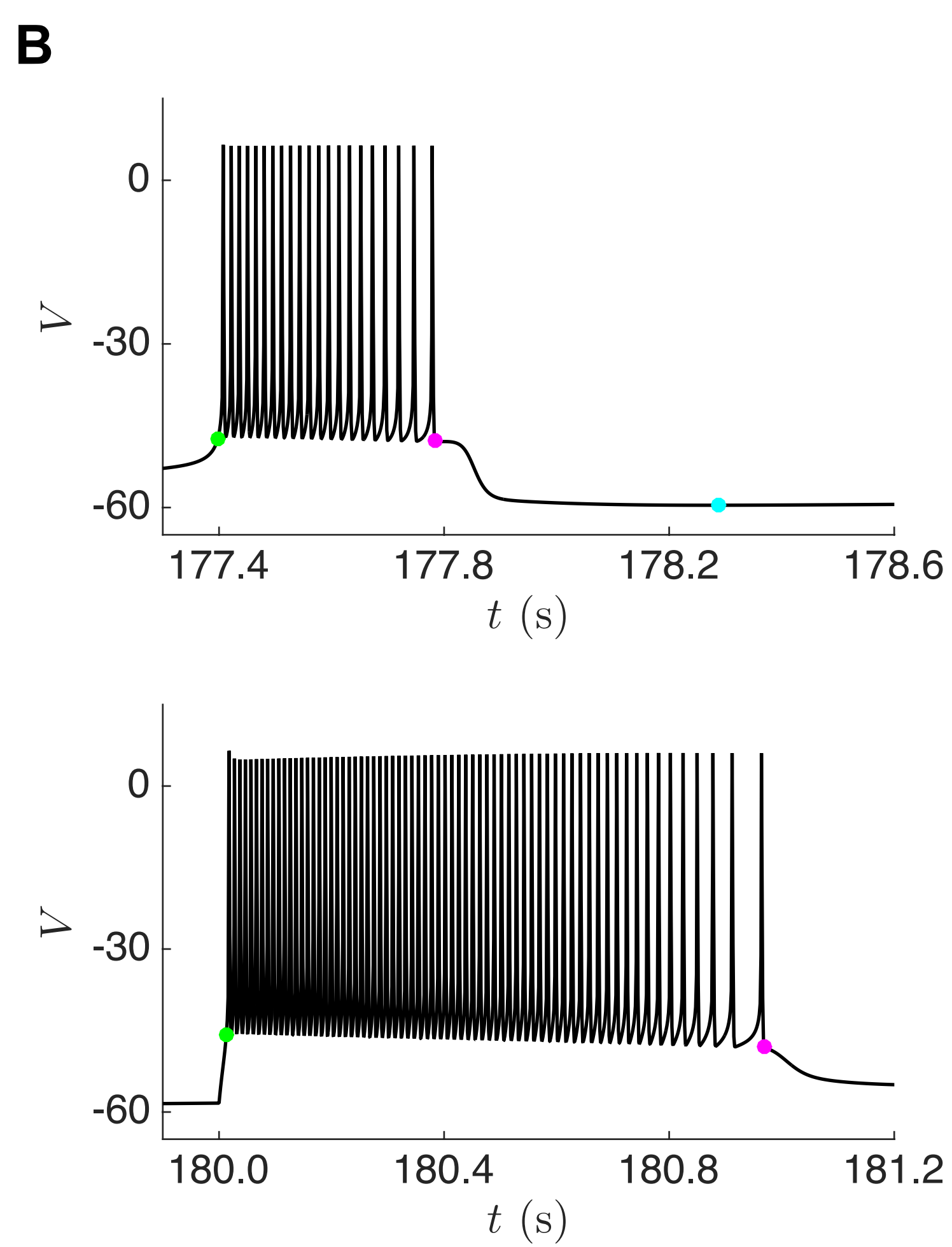
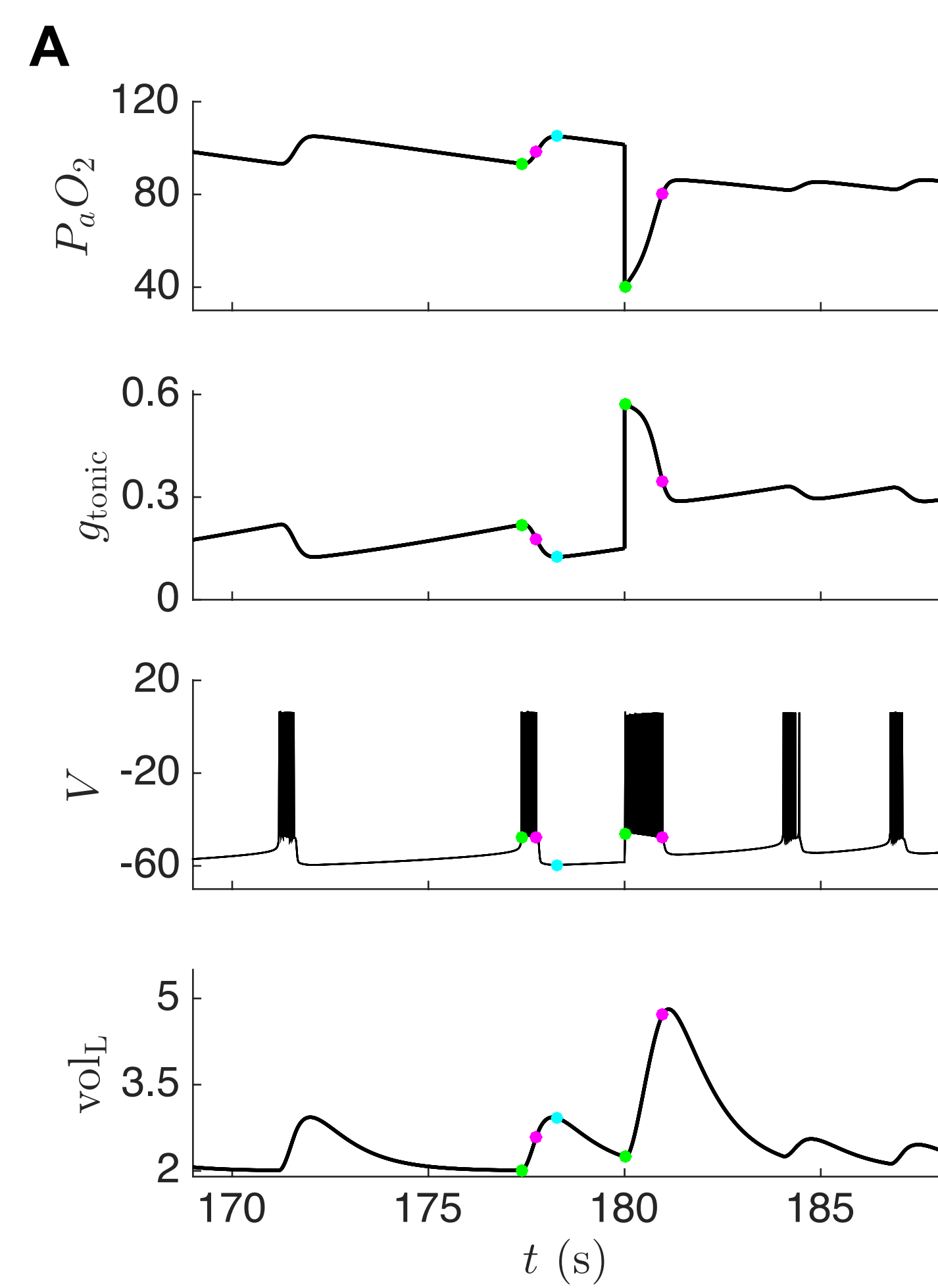


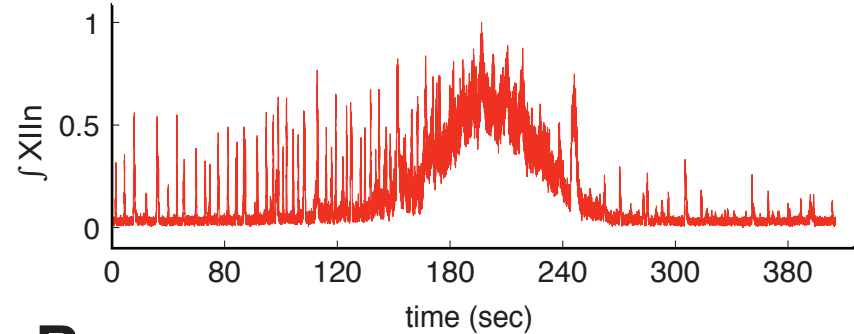
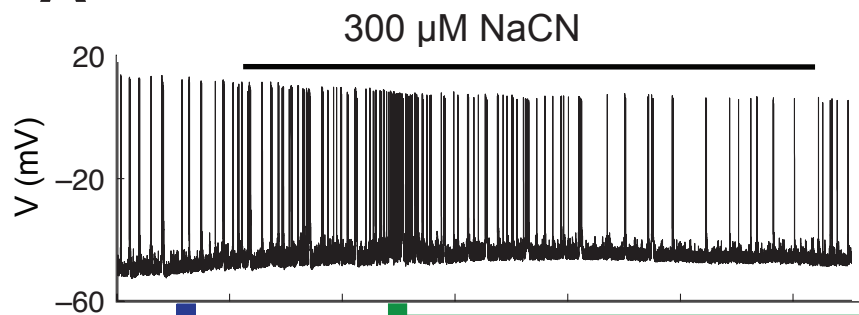
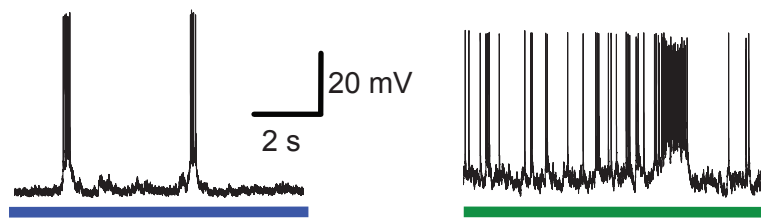
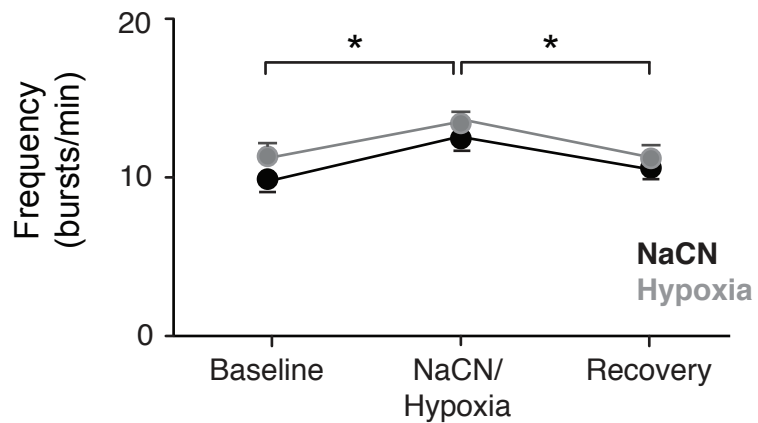
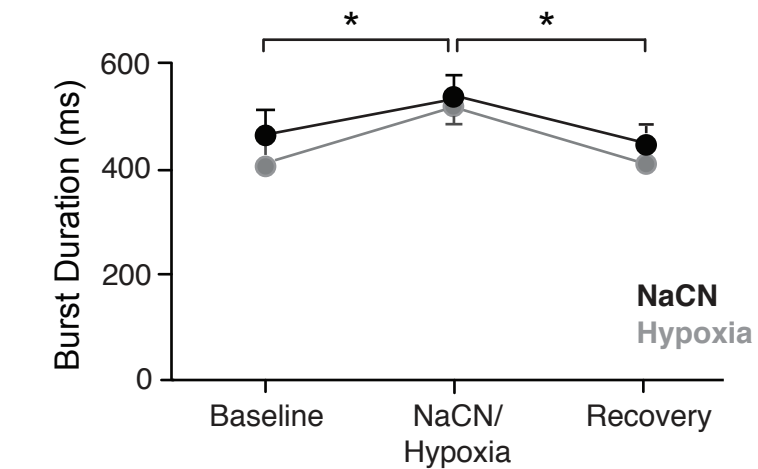
A**B**

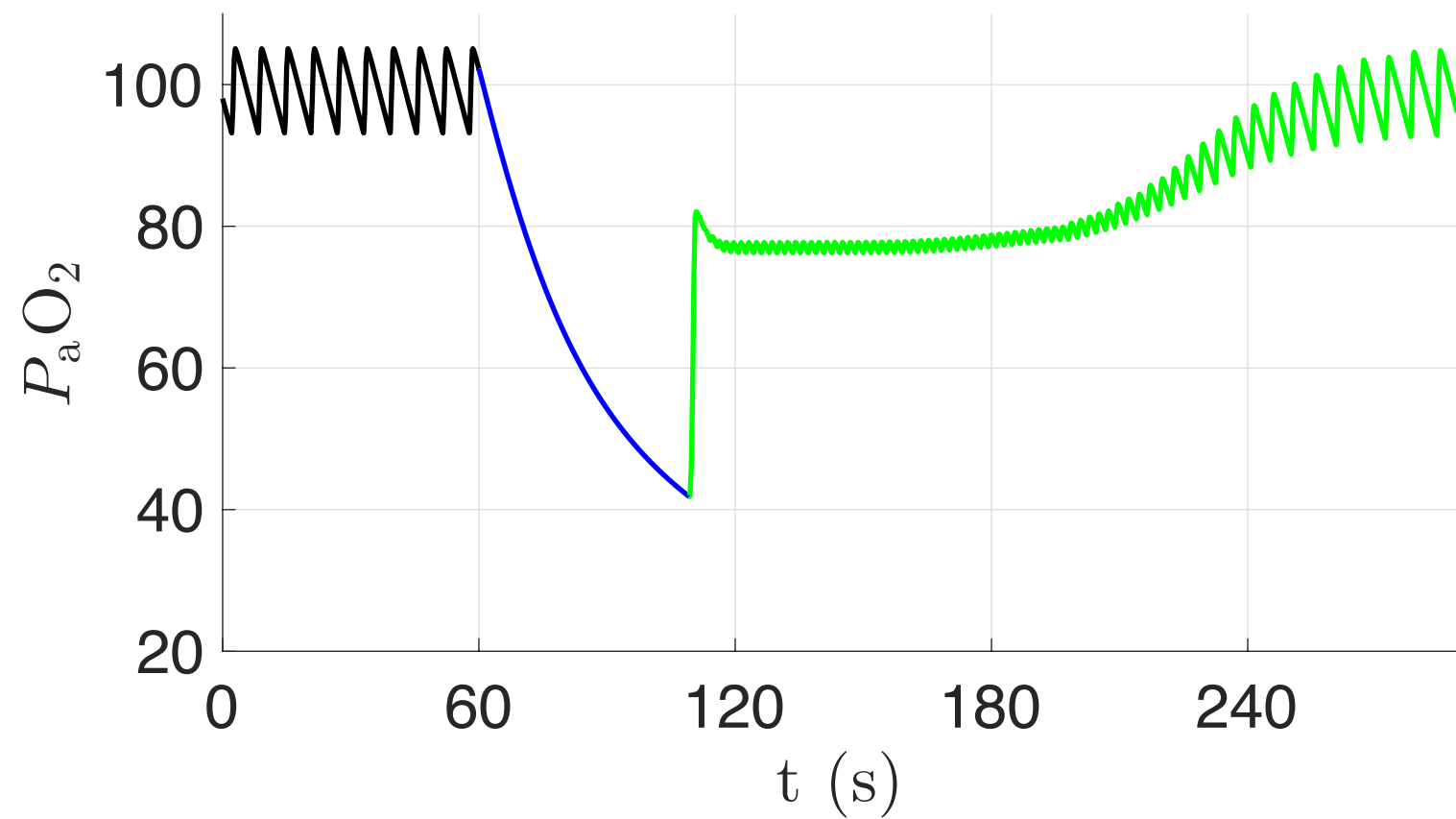
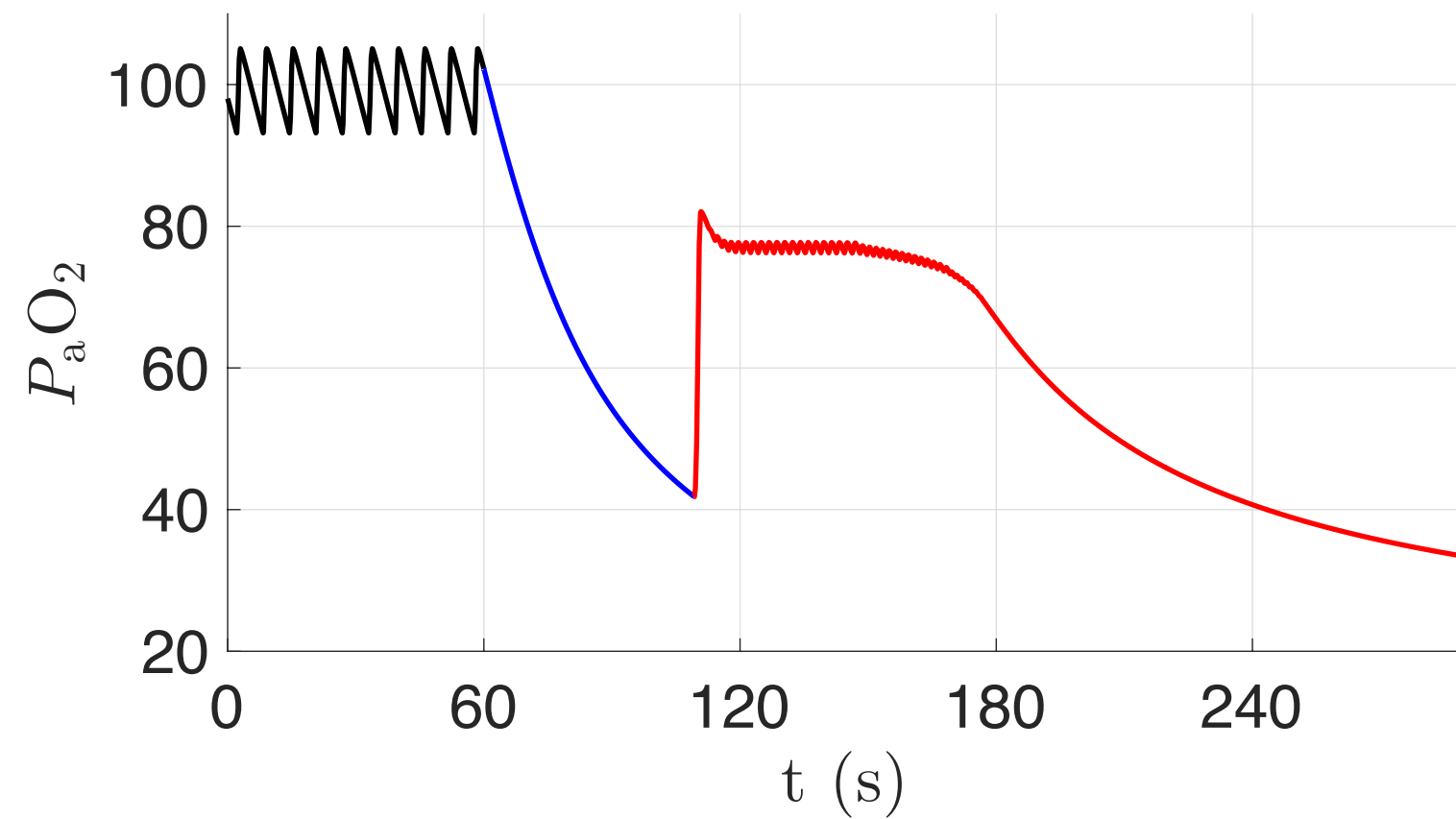
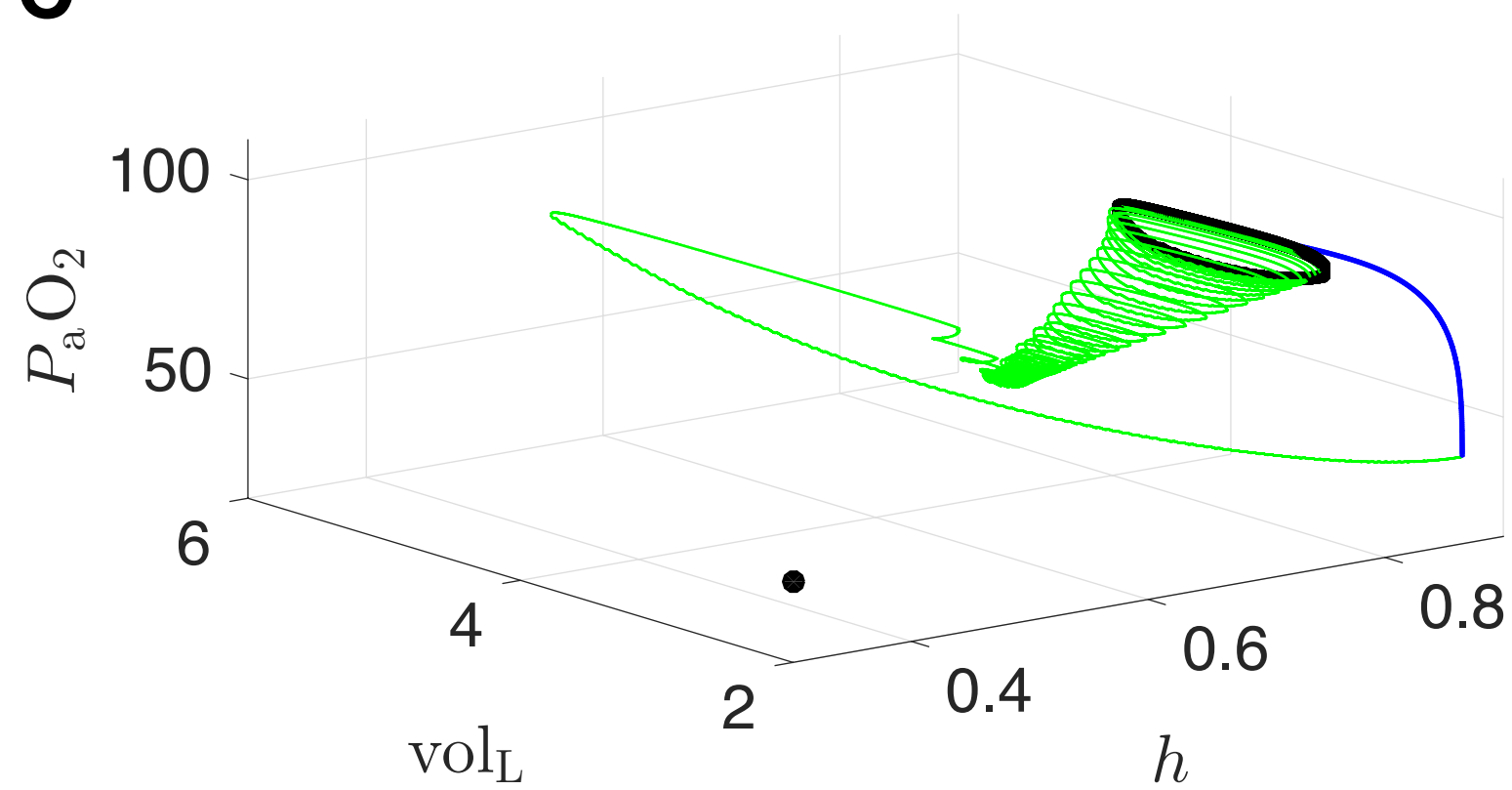








A**B****C**

A**B****C****D**